SANDIA REPORT

SAND2007-3442
Unlimited Release
Printed June 2007

Suppression of Pool Fires with HFC-125 in a Simulated Engine Nacelle

John C. Hewson and David R. Keyser

Sandia National Laboratories

Suppression of pool fires with HFC-125 in a simulated engine nacelle

J. C. Hewson[*]

Fire Science and Technology

Sandia National Laboratories

Albuquerque, NM 87185-1135, USA

D. R. Keyser

INS, Inc.

48015-A Pine Hill Run Rd., Bldg. 1

Lexington Park, MD 20653, USA

Abstract

CFD simulations are conducted to predict the distribution of fire suppressant in an engine nacelle and to predict the suppression of pool fires by the application of this suppressant. In the baseline configuration, which is based on an installed system, suppressant is injected through four nozzles at a rate fast enough to suppress all simulated pool fires. Variations that reduce the mass of the suppression system (reducing the impact of the suppression system on meeting mission needs) are considered, including a reduction in the rate of suppressant injection, a reduction in the mass of suppressant and a reduction in the number of nozzles. In general, these variations should work to reduce the effectiveness of the suppression system, but the CFD results point out certain changes that have negligible impact, at least for the range of phenomena considered here. The results are compared with measurements where available. Comparisons with suppressant measurements are reasonable. A series of twenty-three fire suppression tests were conducted to check the predictions. The pre-test predictions were generally successful in identifying the range of successful suppression tests. In two separate cases, each where one nozzle of the suppression system was capped, the simulation results did indicate a failure to suppress for a condition where the tests indicated successful suppression. When the test-suppressant discharge rate was reduced by roughly 25%, the tests were in agreement with the predictions. That is, the simulations predict a failure to suppress slightly before observed in these cases.

---

[*]E-mail address: jchewso@sandia.gov

Executive summary

This report describes simulations of pool-fire suppression and fire suppressant concentrations in a prototype engine nacelle ground simulator used for testing purposes. These simulations were conducted using the Vulcan fire-physics simulator. Computational predictions have been compared with available measurements of suppressant distribution and with actual fire-suppression tests in the engine nacelle simulator. The pretest predictions were in agreement with the test results in the vast majority of cases. In some pretest simulations and tests, specific nozzles were removed from the suppressant distribution system. In two unique cases, the pretest predictions indicated a failure to suppress one step (25% change in suppressant injection rate) before the actual test did, a conservative result for the predictions.

In general, two criteria need to be met to insure successful suppression. First, the rate of suppressant injection must be high enough that the average concentration in the nacelle exceeds the concentration required to suppress fires. Second, the suppressant must be distributed with sufficient uniformity that the criteria for suppression is met in all regions of the nacelle. The rate of injection required to meet the first criteria can be identified, to a first approximation, with simple zonal models. However, the results presented in the present study indicate that the first criteria is insufficient to guarantee suppression. The manner in which the suppressant is injected and distributed throughout the nacelle also matters. Poor distribution leads to substantial inhomogeneities in the suppressant distribution that allow local burning leading to a reemergence of the fire as the suppressant is dissipated. For the particular nacelle employed here, it is predicted (and the test results agree) that the average mass fraction in the nacelle should exceed the cup burner value by 30-40% to account for inhomogeneities. (This number varies according to details of the suppressant injection process.)

Evaluation of the simulation results suggests several general guidelines for fire suppressant distribution. One of the most significant of these is that suppressant should be injected into or across the primary air inflow when this inflow is substantial. A failure to inject suppressant into the primary air inflow is associated with a substantial region with insufficient suppressant to extinguish a flame. This region is also associated with rapid turbulent mixing that tends to enhance the burning rate if clutter is available to stabilize the flame.

Contents

List of Tables

List of Figures

1 Introduction

Suppression of fires in aircraft engine nacelles and other similar environments is challenging for a number of reasons. To begin with, these environments are highly cluttered. The clutter both acts as a flame stabilizer and impedes the transport of suppressant to this flame-stabilization region. High air-flow rates designed to remove combustible gases from the nacelle also act to rapidly remove suppressant from the nacelle, limiting the potential mixing time. Limits on the mass of suppression systems that can be carried while still allowing aircraft mission success are a further constraint. All of these physical realities contribute to a relatively tight set of requirements for successful fire suppression.

In the past, successful fire suppression systems have been developed through a combination of an understanding of these various issues and extensive testing. Detailed computational models, at the level of computational fluid dynamics (CFD), have had limited success prior to this because of the complexity of the nacelle environment and the relatively high degree of accuracy required. However, new model developments and increased computational capabilities have moved CFD to a point where some level of prediction is now possible.

Further, until their recent phase-out, chemicals like Halon 1301 (CF_3Br) and 1202 (CF_2Br_2) were widely employed to protect vehicles, structures and equipment from fire damage. Because of their high ozone-depleting potential, production of these fire-fighting agents has largely ceased, and research programs have identified a number of other promising agents [10]. Takahashi et al. [28] and Hamins et al. [10] have compiled data on the critical suppressant mole fraction required to suppress fires in various configurations for Halon 1301 and other potential fire suppressants. It is reported that non-ozone depleting agents identified with the most desirable toxicity, corrosion, stability, etc., characteristics generally require a greater agent mass and/or volume, relative to Halon 1301, to suppress a fire. For example, typical mole fractions of Halon 1301 required to suppress fires are between 3 and 4% while HFC-125 (C_2HF_5) requires between 8 and 9%. The mass of agent required is similarly greater, with roughly double the mass of HFC-125 required relative to that for Halon 1301. For applications where the fire suppression-system mass is a key design criterion, as it is in aircraft, a need to optimize the agent delivery system has been identified to minimize the additional suppression-system mass. In this work, the use of HFC-125 as a fire suppressant in a simulated aircraft engine nacelle will be studied. The ability of a CFD model to predict the distribution of suppressants will be assessed (Part 1) along with its ability to predict the suppression of pool fires (Part 2). The results discussed herein are focused on suppressants with boiling temperatures well below operating temperatures, such as HFC-125 (C_2HF_5). The focus here is on pool fires [14, 15]. Spray fires are another significant concern, and recent reviews can be consulted for these scenarios [9, 11]. In addition to engine nacelles, it is vital to also suppress fires in aircraft dry bays [2]. Other work has addressed issues related to higher-boiling point agents [5, 31, 32].

In fire-suppression applications, the ability to predict inhomogeneities in the suppressant concentration is a key requirement for optimizing fire-suppression systems. If regions of the flow field exist where the suppressant concentration is locally below the value that leads to suppression (the cup-burner value or the strained flame-extinction value), then combustion can continue in those regions. In certain applications where the objective is to reduce the fire until fire-fighting crews can attack it, such behavior is acceptable. However, this is not acceptable for fires in aircraft nacelles and other inaccessible areas. Three factors come into play in aircraft nacelles and similar spaces: First, the quantity of fire suppressant that can be carried is severely limited in weight and space in order to satisfy the mission requirements. Second, the need to eliminate trace combustible vapors requires ventilation that also quickly sweeps suppressant out of the nacelle as it sweeps out combustibles. Third, a failure to completely suppress a fire can be catastrophic, since small pockets of fire can quickly propagate through the remaining premixed gases in the nacelle leading to accelerated burning under certain conditions. The present work under the Next Generation Program has focused on developing a set of models and tools to predict suppressant distributions in order to meet these challenges [8].

It is important to point out the relationship of the present work to other levels of modeling. In the fire area, so-called zonal models are frequently employed. While zonal models, treating the volume as a homogeneous mixture, can predict average suppressant concentrations, the suppressant inhomogeneities are important because the local areas that are deficient in suppressant can stabilize a fire until the suppressant has been depleted. The present CFD models are fully capable of describing the variations of the local suppressant concentrations throughout the nacelle. In Sec. 3 a simple zonal model relevant to the present aircraft nacelle application is presented. This is provided to help identify the parameter space in which the nacelle is operating and also to help estimate the nacelle-averaged characteristic conditions. In Sec. 6 the detailed CFD results are presented showing the local flow field. Then in Sec. 8 more global measures of the CFD results are presented to compare with the zonal models and indicate the level of inhomogeneity present.

In Part 2 of the report, simulations of pool fires and the attempted suppression of those fires are presented. These are presented along with the results of a test program that was conducted at the end of this part of the NGP program. All of the simulations presented in this report were pre-test simulations. While there was remarkable agreement between the pre-test simulations and the test results, the careful analysis of the results does indicate some challenges that are faced. Notable among these was the challenge in correctly predicting the pool evaporation rate. At the same time, certain experimental configurations that were suggested as challenging by the simulations could not be realized in the tests due to physical limitations of the nacelle simulator hardware.

Because of the complex, cluttered nature of the aircraft nacelle environment, it is not expected that CFD models will provide truly predictive simulations like those possible in relatively clean environment with

high-end computational submodels. This indicates that a significant experimental test program will be a core part of the suppression system design and qualification process for the foreseeable future. However, the level of success described here indicates that CFD-based methods are coming into a period when they can be successfully used in conjunction with tests. Of particular interest in the design of optimized fire-suppression systems is the use of simulations to explore the parameter space of both system design and system test. The CFD model can be used to iterate over the potential design space to identify designs that provide uniform protection against fires, and yet reduce the system mass or improve upon some other metric. In the present report, the CFD model was used to suggest what nozzles might be removed with little detrimental effect, potentially reducing the mass of piping required. The CFD model is also used to identify the insensitivity of the suppression results to a somewhat reduced total mass of suppressant carried (although the ability to protect against the relight of fires is a concern that is not addressed here). The CFD model is also used to identify regions where relatively robust pool fires can be stabilized, and in this manner could identify the most challenging tests for a particular fire suppression system. Such tests would provide a good measure of the success of the fire suppression system.

The cost of setting up a modeling and simulation capability versus the cost of setting up an extensive test program are both nontrivial, and must be taken into account when considering the approach to be taken. Despite this, there is the potential for improved designs providing better performance (aircraft lifetime cost savings), significant cost savings in the design process, or potentially both. The cost of setting up a test-bed, such as the nacelle simulator described in this report is significant. The cost of running a single experiment is small relative to the cost of the original facility, yet still substantial. Similarly the cost of setting up an initial simulation is significant, involving detailed geometry specifications and grid-refinement analyses. The cost of an additional simulation with slightly differing parameters is small with commodity processors available. As a guide to costs, the initial simulation may require on the order of hundreds of hours to set up while additional simulation costs are roughly two orders of magnitude less in terms of man-hours. Computational requirements are also greater for the initial set up because a large number of test-simulations are involved in checking the appropriateness of the simulation grid, input parameters, etc. Furthermore, the linking of CFD methods with optimization-based search methods [7] provides a nearly automated manner of searching for best possible designs. The result of such a search may point the direction toward the best designs to meet a certain objective.

2   Terminology

The physical device that is being computationally simulated is generally referred to as the "ground-based simulator," and this is to be differentiated from computational simulations. Therefore, here we specify that further references to the "simulator" indicate the physical device located in the laboratory while the "simulation" indicates the computational representation of the simulator.

Part I

Suppressant distribution predictions

The following sections address predictions of the distribution of fire suppressant in the nacelle simulator. The limited available data for suppressant distribution is compared with predictions where possible.

3   Key physics parameters in predicting suppression

Successful total-flooding-based suppression relies on providing a sufficient mass fraction of suppressant to all possible fire locations. There are thus two key issues: First, supply a sufficient overall quantity of suppressant. Second, ensure that the suppressant is sufficiently distributed throughout the nacelle. While the present paper focuses on nacelles, the results in the present section are for relevant to ventilated compartments in general.

In a ventilated compartment, the provision of sufficient suppressant is hampered by the loss of suppressant through whatever ventilation means are available. This section presents a highly simplified model to describe the mean mass fraction of agent in a ventilated nacelle where the composition of gases in the nacelle is assumed to be homogeneous. This analysis identifies two key parameters that affect the overall suppressant mass fraction. These parameters are the ratio of the suppressant injection rate to the total injection rate and the rate of volume displacement by injected fluids per unit nacelle volume.

This simplified inflow-outflow model considers a chamber into which mass fluxes of air and suppressant, denoted $\dot{m}_a$ and $\dot{m}_s$, respectively, are possible. Other fluid sources, like fuel or combustion products, can be added to the air mass source as required. In the simulations conducted here, the additional source attributed to the fuel is at least an order of magnitude smaller than the air. For the purpose of the analysis, the mass fluxes represent known values. We assume that the compartment is sufficiently vented that the pressure will remain constant despite the mass influx. This implies that as mass is added to the system, mass must also leave the system. Because the density may vary with time, the mass that leaves the system will be determined by the volume displaced by the inflowing mass.

To make the analysis tractable, we assume the system to be completely homogeneous so that the density and mass fractions throughout are uniform. Given the pressure, temperature and mean molecular weight, this mean density is $\overline{\rho} = P\overline{W}/RT$. The mean molecular weight is expressible in terms of the mass fractions of the two components, Y_i, as $\overline{W} = 1/(\sum Y_j/W_j)$.

The rate at which gases leave the system is determined by the volume displaced by the inflowing air and suppressant. Multiplying the volume displaced by the mean density gives the mass flow rate of the mixture leaving the chamber

$$\dot{m}_{out} = \bar{\rho} \left(\frac{\dot{m}_a}{\rho_a} + \frac{\dot{m}_s}{\rho_s} \right) \tag{1}$$

where ρ_a and ρ_s are the air and suppressant densities.

Given the above assumptions, conservation equations for the mean suppressant mass fraction in the chamber is

$$\frac{dY_s}{dt} = \frac{\dot{m}_s}{\bar{\rho}V_T} - \left(\frac{\dot{m}_a}{\rho_a} + \frac{\dot{m}_s}{\rho_s} \right) \frac{Y_s}{V_T}. \tag{2}$$

where V_T is the chamber volume. A differential equation for the air (and all other gases, which are lumped with air) is not required since it can be found through overall mass conservation, $\sum Y_i = 1$.

It is convenient to normalize the mass flux for each component with the mass if the chamber were filled with that single component

$$\mu_s = \frac{\dot{m}_s}{\rho_s V_T} \qquad \mu_a = \frac{\dot{m}_a}{\rho_a V_T}. \tag{3}$$

These have dimensions of rate (one over time) and indicate how fast the air or suppressant would displace a volume of fluid V_T. Using these with

$$\frac{\rho_i}{\bar{\rho}} = \sum_j \frac{W_i Y_j}{W_j} = \sum_j Y_j r_{ij} \tag{4}$$

where r_{ij} is the ratio of the molecular weights of component i to component j, Eq. 2 is written

$$\frac{dY_s}{dt} = \mu_s r_{sa} - (\mu_s r_{sa} + \mu_a) Y_s. \tag{5}$$

This first-order ordinary differential equation can be solved for the relevant scenario where $\mu_a = \mu_a^0$, and μ_s is zero except for the time interval $0 < t < t_e$ during which $\mu_s = \mu_s^0$. Because of the step-function nature of μ_s the solution differs for $t < t_e$ and $t > t_e$. For $0 < t < t_e$ the suppressant mass fraction starts at zero and exponentially approaches a steady state value of $\mu_s^0 r_{sa}/(\mu_s^0 r_{sa} + \mu_a^0)$ as described by

$$Y_s = \frac{\mu_s^0 r_{sa}}{\mu_s^0 r_{sa} + \mu_a^0} \left[1 - e^{-(\mu_s^0 r_{sa} + \mu_a^0)t} \right]. \tag{6}$$

The time constant for the approach to the steady-state value is $1/(\mu_s^0 r_{sa} + \mu_a^0)$. Note that this shows that the steady-state value is reached more rapidly for higher air mass flow rates but the steady-state value is correspondingly lower. The rate of change (time-derivative) of Y_s is, however, directly proportional to the suppressant mass flow rate and not the air flow rate.

For $t > te$ the suppressant mass fraction decays exponentially from whatever value it attained at $t = te$ in Eq. 6 according to

$$Y_s = \frac{\mu_s^0 r_{sa}}{\mu_s^0 r_{sa} + \mu_a^0} \left[1 - e^{-(\mu_s^0 r_{sa} + \mu_a^0)t_e} \right] e^{-\mu_a^0(t - t_e)}. \tag{7}$$

With the suppressant inflow turned off, the time constant for the decay of the suppressant mass fraction is $1/\mu_a^0$ and the rate of decay is proportional to μ_a^0 and the value of Eq. 6 evaluated at $t = t_e$, which is represented by the terms on the right-hand side of Eq. 7 prior to the last exponential.

This indicates two key parameters to be considered when designing a suppression system. The ratio of suppressant mass inflow to the total mass inflow gives the steady-state suppressant mass fraction

$$Y_{s,st} = \frac{\mu_s^0 r_{sa}}{\mu_s^0 r_{sa} + \mu_a^0}, \tag{8}$$

corresponding to continuous suppressant injection. The product of the time constant appearing in the exponential Eq. 6 and the duration of the injection, $\tau = (\mu_s^0 r_{sa} + \mu_a^0)t_e$ indicates how close one comes to this steady state mass fraction. After an injection period of roughly $1/(\mu_s^0 r_{sa} + \mu_a^0)$, $(1 - 1/e)$ (roughly two-thirds) of the steady-state value is reached, and roughly eighty-five percent of the steady-state value is reached after twice that period. Injection for longer periods serves primarily to increase the residence time for the highest suppressant concentrations. The maximum averaged suppressant mass fraction is thus estimated to be

$$Y_{s,max} = \frac{\mu_s^0 r_{sa}}{\mu_s^0 r_{sa} + \mu_a^0} \left[1 - e^{-(\mu_s^0 r_{sa} + \mu_a^0)t_e} \right]. \tag{9}$$

This is presented graphically in Fig. 1 for the dimensionless variables $\mu_s t_e$, which represents the mass of suppressant injected over a time period t_e normalized by the total mass that would be required to fill the nacelle, and $\mu_a t_e$, which represents the air inflow during the period of injection normalized by the mass of air that fills the nacelle. For the 3.2 kg of HFC-125 in the current nacelle at ambient temperatures, $\mu_s t_e \approx 0.5$ and is represented by the center curve in Fig. 1. The upper and lower curves indicate a 50% increase or decrease in the suppressant mass. For the conditions considered here, the typical values for $\mu_a t_e$ are 1 to 2. The range of values on the abscissa show the consequences of changing the duration of the injection. Note that average temperatures above ambient will increase μ_i proportionally because μ_i is normalized by the average density. This will reduce the time constant for filling and flushing the nacelle, tending to cause $Y_{s,max}$ to more closely approach $Y_{s,st}$.

This simple model does not account for any spatial fluctuations that may lead to local conditions where the fire can be sustained. Prediction of spatial fluctuations is only possible at the CFD level, accounting for the details of the geometry and boundary conditions. The most that can be said is that higher fluid mixing rates will generally lead to more uniform suppressant distribution. As will be seen in later sections, though, the collocation of high mixing rates with the suppressant mixing process is not guaranteed.
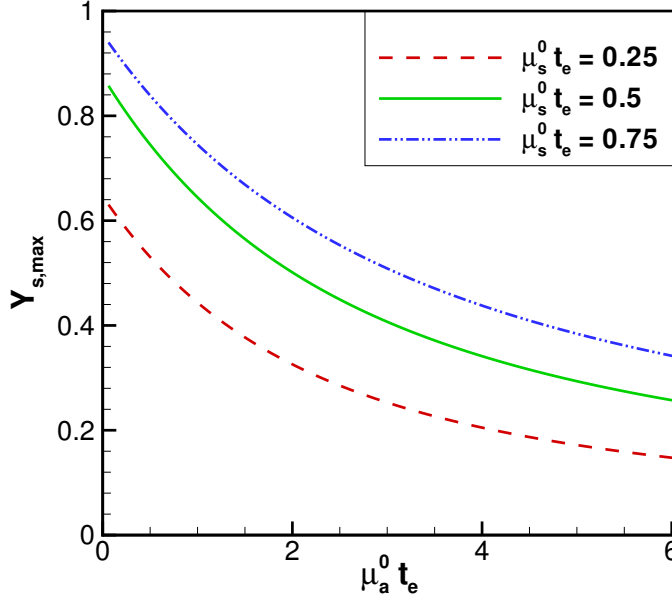
Figure 1: The maximum suppressant mass fraction, averaged over the nacelle, attained for the indicated dimensionless suppressant and air mass flux.

4 An Overview of the Vulcan fire-physics code

Vulcan has been developed over the past eight years at Sandia National Laboratories (SNL) in collaboration with the SINTEF Foundation and the Norwegian University of Science and Technology. Vulcan is derived from the Kameleon Fire model [17] and uses an extension of the SIMPLEC method [27] to solve the conservation equations on a structured, staggered, three-dimensional Cartesian, finite-volume grid. The ability to resolve the geometry of the system is only limited by the ability to construct the appropriate grid with the Cartesian grid generator available in Vulcan. First- and second-order upwind schemes can be used for the convective terms. Turbulence is modeled using a standard two equation k-ϵ model [18]. The Vulcan code has the capability of performing fire simulations, and the combustion simulation is based on Magnussen's Eddy Dissipation Concept (EDC) assuming mixing-limited combustion [17, 24]. Models of soot generation and oxidation are also included. Radiation transport is conducted using the discrete-transfer model of Shah [22]. The suppression model employed in Vulcan is discussed in Sec. 11

5 Overall geometry

The engine-nacelle simulations have been designed in accordance with test fixture drawings of the nacelle simulator [19] and in accordance with visual inspections of the simulator, located at Patuxent River Naval Air Station. The nacelle simulator is based roughly on the United States Navy's F-18, which has two engines located side by side in the fuselage. The ground simulator used in the fire tests simulated here is a mock up of the port engine nacelle. Therefore, the port side corresponds to the outboard side of the engine and the starboard side corresponds to the inboard side of the engine. The nacelle is roughly 3.18 m (125 in.) long. All distances in the text of the present report refer to distances from the front of the nacelle, which is approximately 15 m behind the nose of the aircraft. In the figures, however, the y-axis is measured from the reference point at the nose of the aircraft in concurrence with the drawing specifications.

The width and height vary significantly along the length, but are contained within a region 1.45 m high and 1.15 m wide. Coordinates are measured from a reference point on the top starboard side of the simulator test fixture so that all vertical coordinates are negative while other coordinates are positive. In conjunction with the rearward taper of the airframe, the nacelle is generally tallest and widest near the forward end. At various sections, this narrowing is countered by an abrupt increase in distance of the outer nacelle skin from the engine on the sides and top. The lower nacelle surface slopes smoothly up from the forward to the aft, crossed by five ribs of varying heights. There are roughly four longerons running along the lower nacelle surface. The two central longerons end about 0.6 m before the aft end to provide space for the lower diamond vent.

The engine, a hollow cylinder in the ground simulator, extends from the forward to the aft of the nacelle. The engine diameter is nominally 0.77 m with a slight narrowing over the front 0.61 m to a minimum diameter of 0.62 m. From 0.81 m aft to the aft end of the nacelle, the engine is uniformly 0.77 m in diameter. The outer surface of the engine is generally smooth, although various later-described clutter items are attached to it.

In addition to the ribs and longerons, the most significant clutter is located near the forward end of the nacelle. It is dominated by a "gear-box" assembly located from 0.1 m to 0.75 m behind the forward end and mostly below the engine. The gear-box assembly is a collection of several generally parallelepiped and cylindrical objects of varying sizes that obstruct the flow in the large space between the engine and the lower nacelle in the vicinity of the air inlet scoop. Additional large parallelepiped clutter objects are located along the engine, particularly on the port side as far back as 1.5 m behind the forward end. Smaller clutter, primarily tubing and wire bundles, exists along the lower half of the engine across the length of the nacelle. Some of this smaller clutter has been identified as a potential relight surface because of the relatively low thermal capacity and rapid heating to very high temperatures of smaller clutter [25]. The afterburner control vanes at the aft end of the nacelle have not been included in the computational model because the setup (initially) focused on fire scenarios near the forward end of the nacelle.

The grid employed in the simulations is coarse, with a resolution of one inch (2.54 cm control volume edges). The total grid size is then roughly 320,000 control volumes, but the majority of these are not in relevant regions (outside the nacelle or inside the engine core); a more efficient grid can be obtained using an unstructured grid as with Sandia's Fuego code. The coarse grid used here is selected specifically because the clutter in the nacelle is not to be resolved, but is to be treated with a clutter model [4]. Unfortunately, at the time the simulations were initiated, the clutter model treatment of near wall clutter (the most significant clutter in this nacelle simulator) was not correctly implemented and thus the clutter model was turned off. The clutter model has since been correctly implemented in Vulcan [23]. No rigorous grid resolution studies were conducted during the course of this study for the nacelle simulator geometry, but it is expected that finer grid resolution will change at least the details of the results. Because the coarseness of the resolution is relatively uniform with respect to the flow dynamics, it is expected that the general flow characteristics will not change dramatically.

6 Flow field

In the absence of fires and suppressant flow, the flow field in the nacelle is dominated by flow through an inlet air scoop located near the front of the nacelle coming up through the nacelle bottom. The inlet air flows from the inlet across the engine toward the upper aft of the nacelle. For the purposes of the simulations, air mass flow rates of 0.33, 0.5, 0.66 and 1.0 kg/s have been considered. These air flow rates cover the range (0.57, 0.68 and 0.95 kg/s) described in Ref. [6] that were obtained from F-18 C/D flight test data and scaled up for the E/F aircraft [6]. It is noted that these flow rates can occur over varying altitudes and external air temperatures so that the corresponding air densities may differ somewhat. For the present simulations, only expected ambient conditions at the Patuxent River NAS test facility are considered; these are assumed to be 101000 Pa pressure and 293 K temperature. A sensitivity analysis with respect to air density would be straightforward with the Vulcan CFD code, but is not performed here.

The inlet air mass flow rates determine the air-exchange times. The air-exchange time is the time over which the mass of air entering and leaving the nacelle equals the mass of air in the nacelle. For the simulation, the internal volume of the nacelle, neglecting clutter objects, is just over 1.4 m^3. For the range of air-flow rates (0.33 to 1.0 kg/s) at ambient densities, this gives an air-exchange time of 5.4 to 1.6 s. The air exchange time is equivalent to $1/\mu_a^0$ in the nomenclature of Sec. 3. Shorter air-exchange times correspond to higher mass flow rates. Similarly, for a fixed mass flow rate and a lower density, the air exchange time would be proportionately lower. This provides an indication of the effects of operation at different altitudes where the ambient density differs. Thus, the change in air-exchange time associated with lower ambient densities can be simulated on the ground with higher inlet mass flow rates.

The inlet cross section is approximately 0.008 m^2 and air-flow velocities considered range from 50 to 150 m/s. This results in an inlet Reynolds number, with the length scale defined as the square root of the inlet cross section area, ranging from 3×10^5 to 9×10^5. The inlet air flow is thus strongly turbulent even without the clutter-enhanced mixing.

6.1 Flow field without fire or suppressant injection

In the absence of suppressant injection, the flow field is dominated by the inlet air scoop located on the nacelle bottom near the forward end of the nacelle and directed toward the nacelle aft, but also slightly upward and toward the starboard side, the latter being the centerline of the aircraft. The inlet air flows upward onto the engine and up around the starboard side of the engine. This creates a large circulating flow on the starboard side of the engine. The flow above the engine in the nacelle is primarily in the forward direction, and much of this flow moves down around the engine toward the forward end of the nacelle and is entrained by the inlet air flow. On the port side of the engine, the flow is observed to be primarily in the forward direction, similar to the flow along the top of the nacelle. Figure 2 demonstrates some of these flow patters with velocity vector plots.

Air leaves the nacelle to balance inflow through several vents and openings. The relative flow through the various paths was measured and found to be independent of air-flow rate [6, 20] and the relative flow rates measured there have been reproduced in the present simulations to within a few percent. The majority of the air (65%) leaves the nacelle through the upper diamond vent located in the top of the nacelle 2.85 m behind the nacelle front. Another 10% of the air leaves through the balance piston, centered on the nacelle top 0.75 m from the nacelle front. The remaining 25% of the air leaves through four openings in the nacelle front simulating connections to the AMAD bay and other parts of the aircraft. In the ground simulator, the flow out the lower diamond vent, located directly below the upper diamond vent, is effectively zero; this may be because the fine mesh screen covering the vent was clogged with soot, rust and other particulate [6, 20]. The flow rate out of the various openings was matched to the measured flow rates [6, 20] by varying the porosity of the opening, given the known area of the opening. It would be possible to equate the lower diamond vent porosity to that of the upper diamond vent to ascertain any changes in the flow patterns that might occur in fleet aircraft (not subject to the repeated fires in the ground test simulator) with clean diamond vents, but this has not been done.

6.2 Flow field with suppressant injection

The nacelle simulator was outfitted with a set of four suppressant nozzles that were found to be sufficient to suppress a fire when 3.2 kg (7 lbs.) of suppressant were discharged [25]. These are denoted by the numbers 1 through 4 with larger numbers corresponding to nozzles that are further toward the rear of the nacelle.
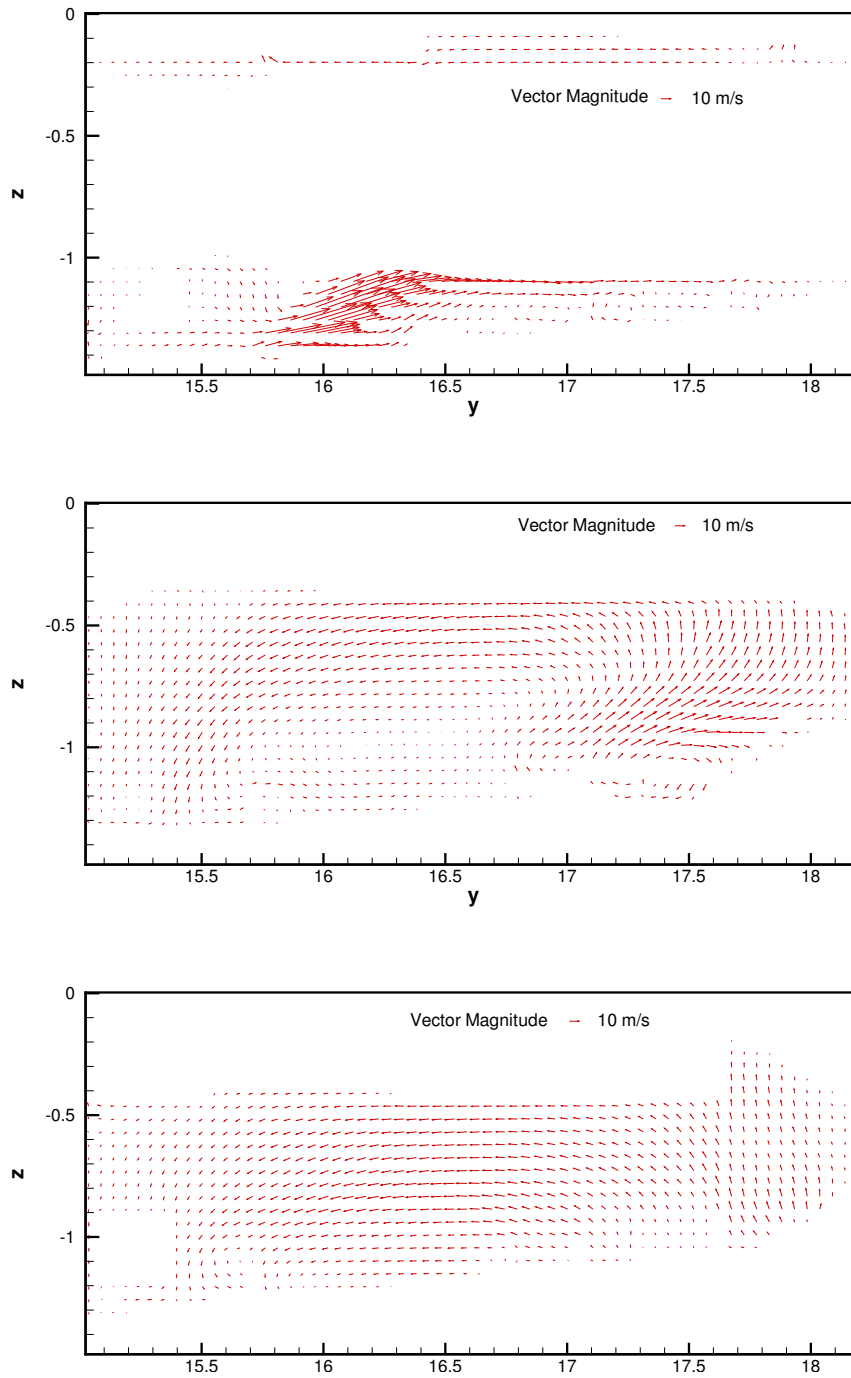
Figure 2: Velocity vectors (top) near the nacelle center, 0.63 m from the starboard reference point, (middle) on the starboard side of the engine, 0.20 m from the starboard reference point and (bottom) on the port side of the engine, 1.06 m from the starboard reference point. Air flow into the nacelle is 0.66 kg/s.

27

Table I: Nozzle characteristics.

Nozzle	Orifice diameter [cm] [25]	Nozzle location x [m]	y [m]	z [m]
1	.396	.09	15.78	-1.02
2	.475	.09	15.84	-1.15
3	.475	.19	16.82	-.41
4	.330	1.03	17.70	-.46

Simulations have been conducted for suppressant injection through these nozzles into the nacelle in the absence of a fire to obtain information on the suppressant distribution through the nacelle. The suppressant was assumed to enter the nacelle in the vapor phase or to vaporize fast relative to other time scales. Except where noted the net suppressant mass flux into the nacelle is 1.06 kg/s so that the injection duration for the standard 3.2 kg of HFC-125 was 3 s. This fixed mass of suppressant injected corresponds to $\mu_s^0 t_e \approx 0.5$ in the nomenclature of Sec. 3. This 3 s duration for the injection was chosen because the available HFC-125 concentration measurements showed an approximately 3 s rise time (see Figs. 30 and 31). The injection rate was taken to be constant during the duration of the injection; this is known to be a gross simplification, but better information was not available at the time of the simulations. The suppressant mass flux for each nozzle was assumed to be proportional to the nozzle orifice area.

The mass fraction of HFC-125 in vertical planes near the nacelle center and near the starboard and port sides are shown in Figs. 3 through 29 at half-second intervals. The mass fractions are colored in such a manner that cool colors indicate likely suppression and hot colors indicate that suppression is unlikely. The critical mass fraction for suppression in the absence of intense mixing is somewhat less than 0.3 (the cup-burner suppressant mass fraction is 0.28 and strained counterflow flames extinguished with a mass fraction of 0.16 [9], so that this is a conservative estimate), and so the dividing line for likely suppression can be taken to be the dividing line between yellow-green and green. Depending on various conditions, suppression may occur for lower mass fractions of HFC-125. Velocity vectors are also provided in Figs. 3 through 29 to indicate the general flow direction.

Nozzle 1 is located on the starboard side of the nacelle in the forward section and is directed upward. The suppressant from nozzle 1 is observed to initially fill the upper forward nacelle and is advected forward and into the lower forward nacelle. The high suppressant mass fractions in the upper forward sections of the nacelle visible in Figs. 14, 16, 23 and 25 arise primarily from nozzle 1. Note that some suppressant from nozzle 1 appears to leave the nacelle soon after injection from the upper balance piston vent in Figs. 3 through 7

Nozzle 2 is located near nozzle 1 on the starboard side of the nacelle and directed to the port side

across the top of the inlet air flow. Suppressant from nozzle 2 is spread rearward by the inlet air along the engine. There is some uncertainty in the momentum of the suppressant flow, but with the current uniform 3 s discharge the momentum is sufficient that more suppressant flows along the port side of the inlet jet and along the lower port side of the engine. The high suppressant mass fraction along the lower port side forward of the 16 m point in Figs. 5 and 7 comes from nozzle 2. If the suppressant jet momentum has been grossly overestimated, the suppressant may not cross the jet and would flow along the lower starboard side of the engine. There is reason to believe that late in the suppressant injection period as the bottle pressure drops that the suppressant momentum is less than currently described.

Nozzle 3 is located just past the mid-point of the nacelle, in between the second and third ribs, on the upper starboard side of the engine. Suppressant flow is directed at roughly a 45 degree angle upward across the engine and into the recessed area at the top of the nacelle. The majority of the suppressant mixes in this recessed area with flow moving forward and is transported gradually along the upper nacelle in the forward direction as evidenced by the high suppressant mass fractions along the forward half of the upper nacelle in Figs. 3 through 7. A significant minority of the suppressant from nozzle 3 leaves the upper recessed region on the port side of the engine. In this region the flow coming from the inlet air is rearward and this advects the suppressant into the regions on the port side near the fourth rib. However, the suppressant transported in this direction is sufficiently diluted that it does not show up on the contour plots.

Nozzle 4 is located on the port side of the engine near the aft of the nacelle just behind the fifth rib. The suppressant is directed downward along the side of the engine as shown in Figs. 21 through 25. This flow is counter to the general upward flow toward the upper diamond vent and so the suppressant is split between suppressant that goes down and around the engine in the lower nacelle area (Figs. 3 through 7) and suppressant that flows rearward and upward to fill the area near the afterburner control actuators. Forward transport of suppressant is inhibited by the overall aft-ward flow from the inlet to the upper diamond vent. The large sixth rib in the lower nacelle just forward of nozzle 4 and also the large fifth rib significantly restrict forward transport of agent past these planes because they constrict the flow leading to relatively high aft-ward velocities.
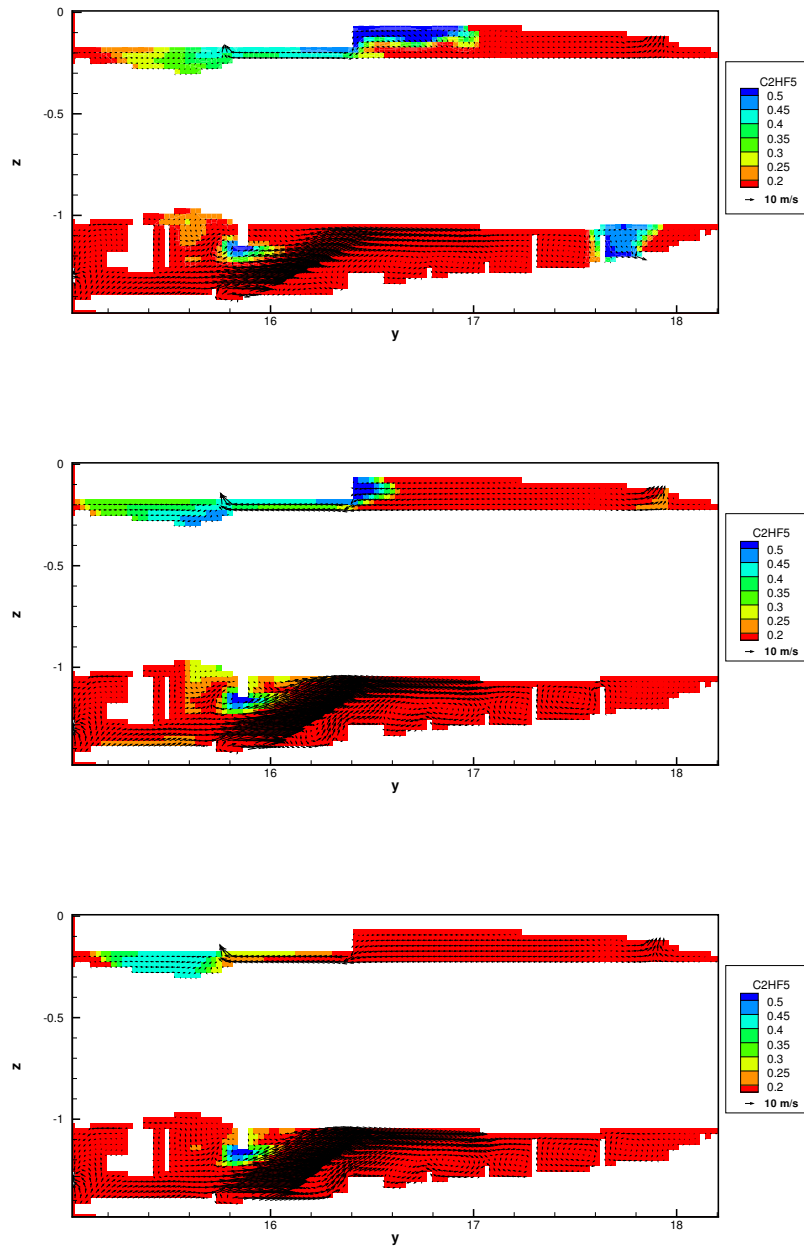
Figure 3: Contour plots of C_2HF_5 at 0.5 s after start of suppressant injection near the nacelle centerline, 0.63 m from the starboard reference point. Air flow into the nacelle is 0.66 kg/s (top) or 1.0 kg/s (center, bottom). Suppressant flow is 3.2 kg over 3 s (top, center) or over 4 s (bottom).
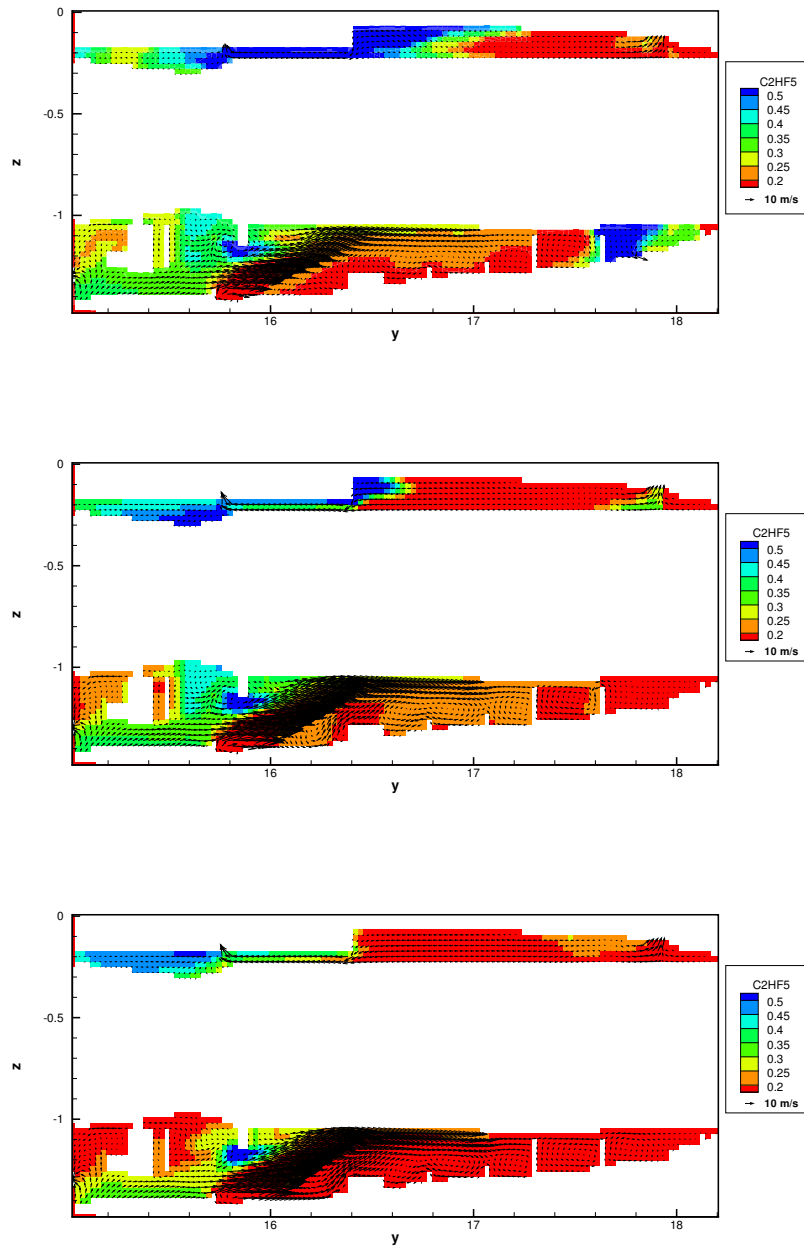
Figure 4: Contour plots of C_2HF_5 at 1.0 s after start of suppressant injection near the nacelle centerline, 0.63 m from the starboard reference point. Air flow into the nacelle is 0.66 kg/s (top) or 1.0 kg/s (center, bottom). Suppressant flow is 3.2 kg over 3 s (top, center) or over 4 s (bottom).
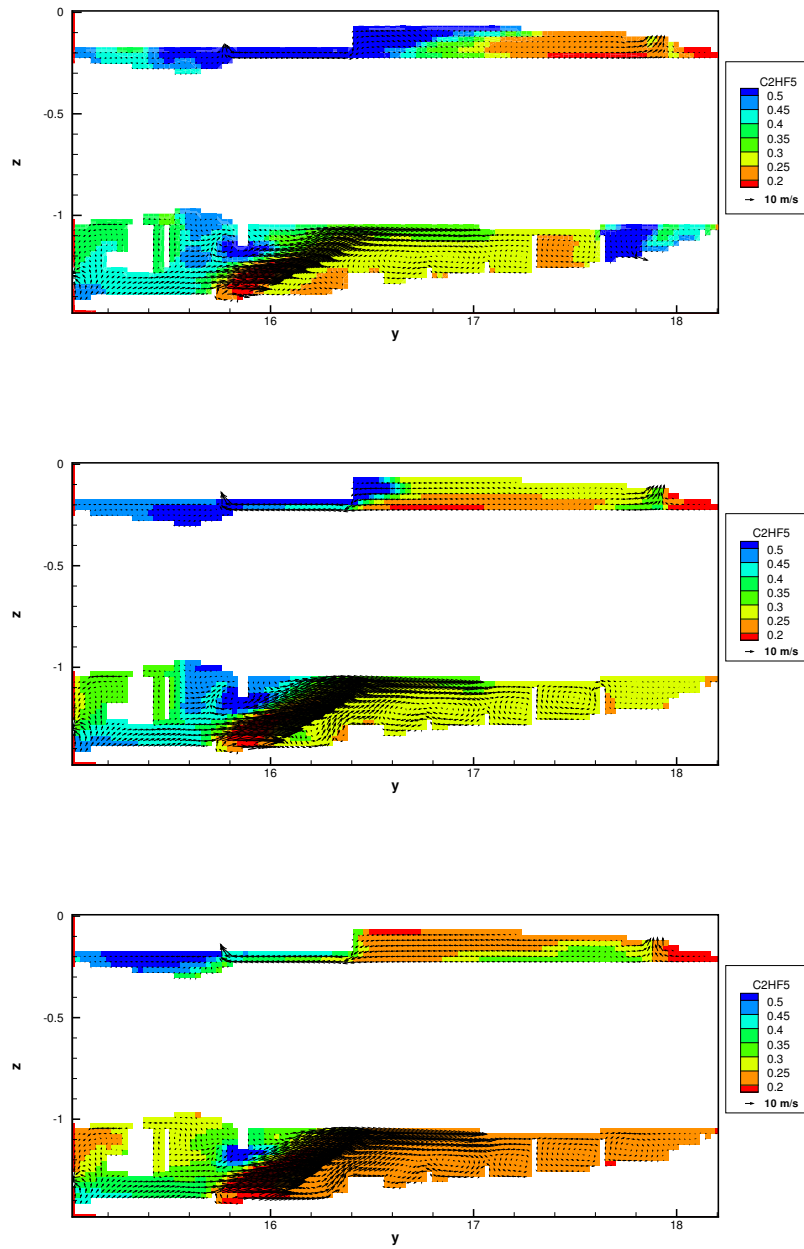
Figure 5: Contour plots of C_2HF_5 at 1.5 s after start of suppressant injection near the nacelle centerline, 0.63 m from the starboard reference point. Air flow into the nacelle is 0.66 kg/s (top) or 1.0 kg/s (center, bottom). Suppressant flow is 3.2 kg over 3 s (top, center) or over 4 s (bottom).
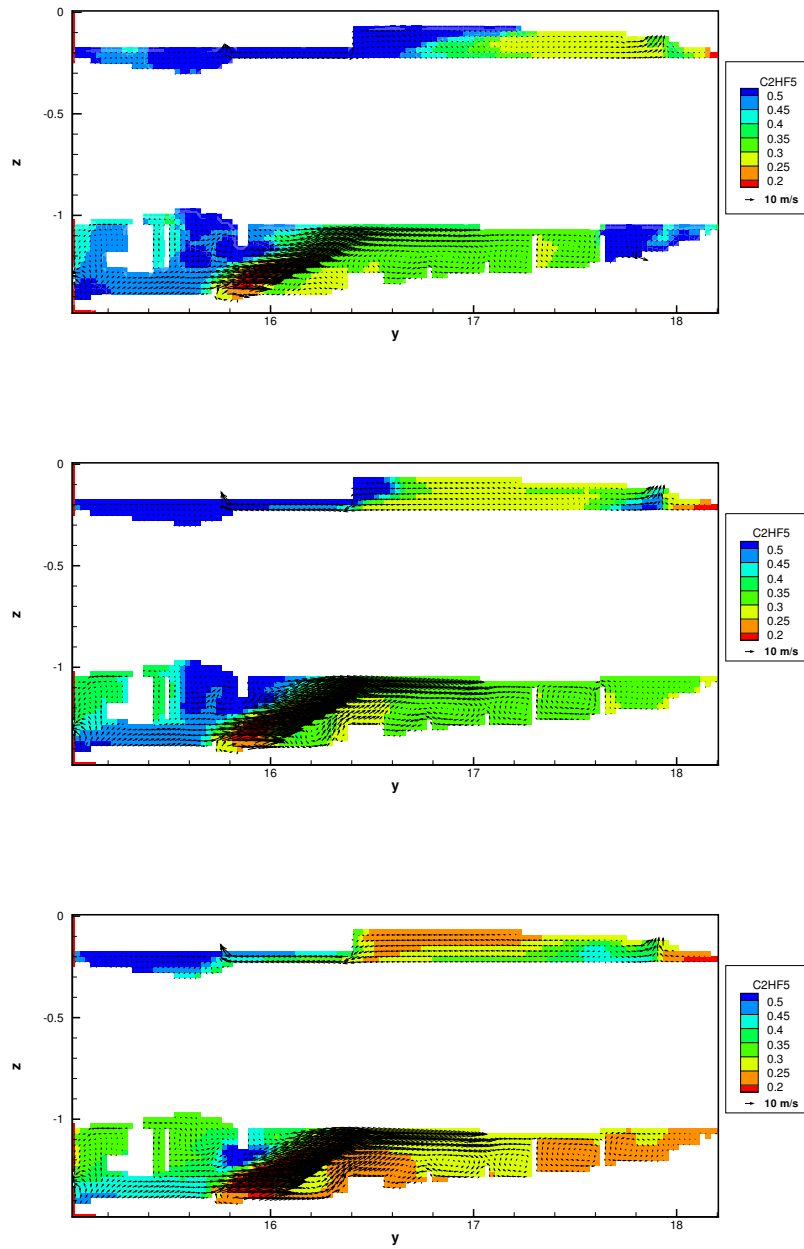
Figure 6: Contour plots of C_2HF_5 at 2.0 s after start of suppressant injection near the nacelle centerline, 0.63 m from the starboard reference point. Air flow into the nacelle is 0.66 kg/s (top) or 1.0 kg/s (center, bottom). Suppressant flow is 3.2 kg over 3 s (top, center) or over 4 s (bottom).
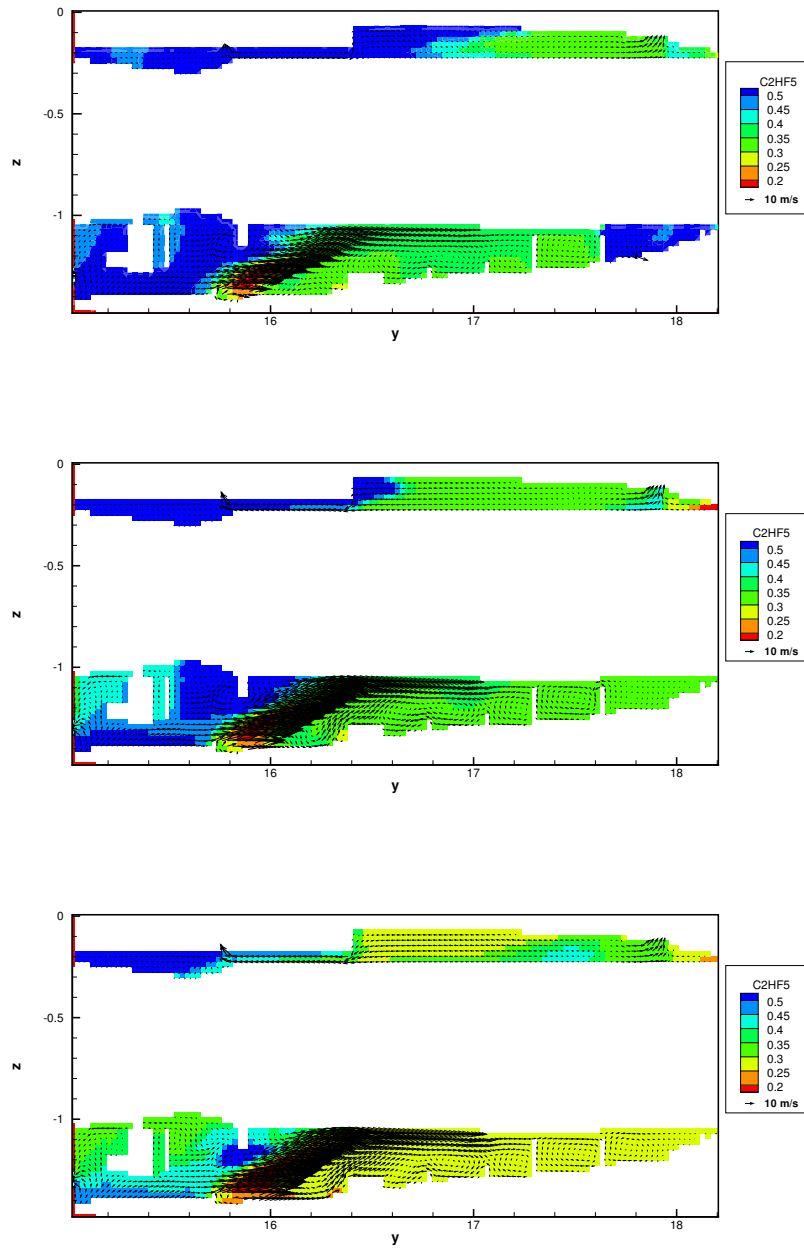
Figure 7: Contour plots of C_2HF_5 at 2.5 s after start of suppressant injection near the nacelle centerline, 0.63 m from the starboard reference point. Air flow into the nacelle is 0.66 kg/s (top) or 1.0 kg/s (center, bottom). Suppressant flow is 3.2 kg over 3 s (top, center) or over 4 s (bottom).
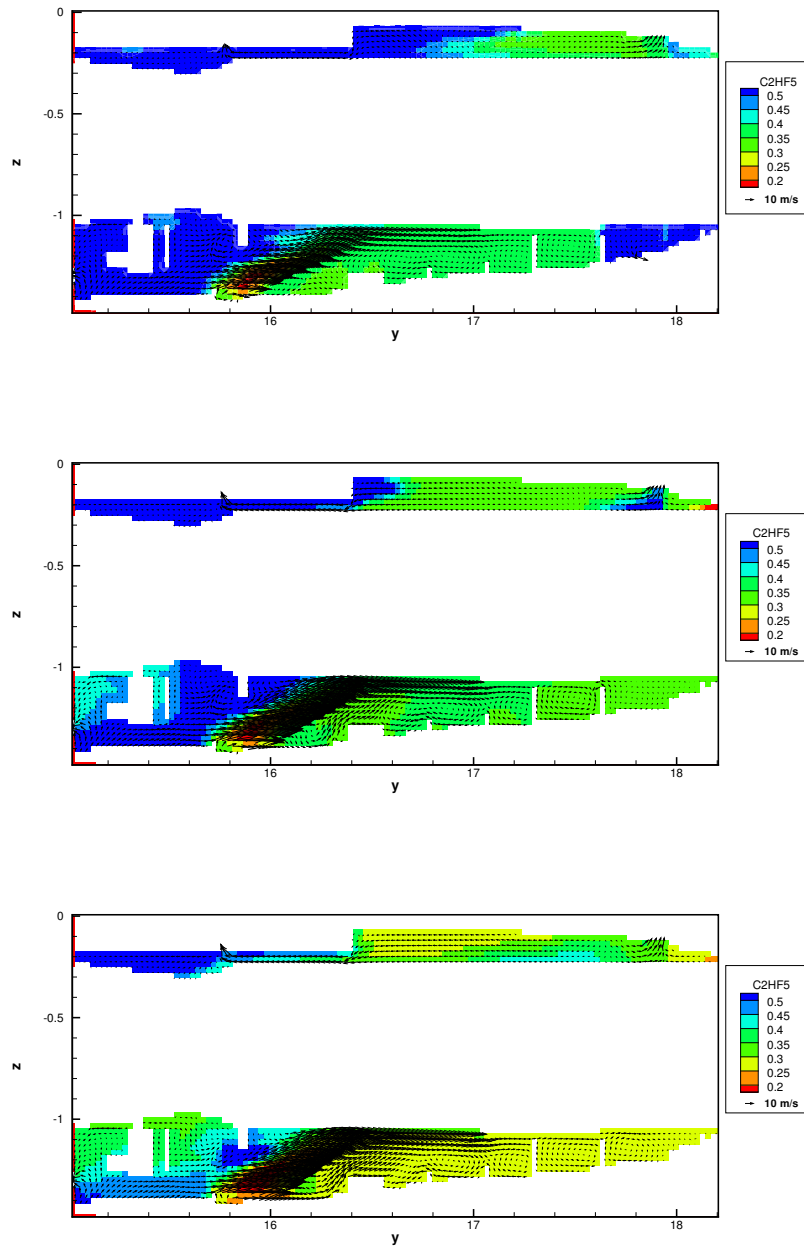
Figure 8: Contour plots of C_2HF_5 at 3.0 s after start of suppressant injection near the nacelle centerline, 0.63 m from the starboard reference point. Air flow into the nacelle is 0.66 kg/s (top) or 1.0 kg/s (center, bottom). Suppressant flow is 3.2 kg over 3 s (top, center) or over 4 s (bottom).
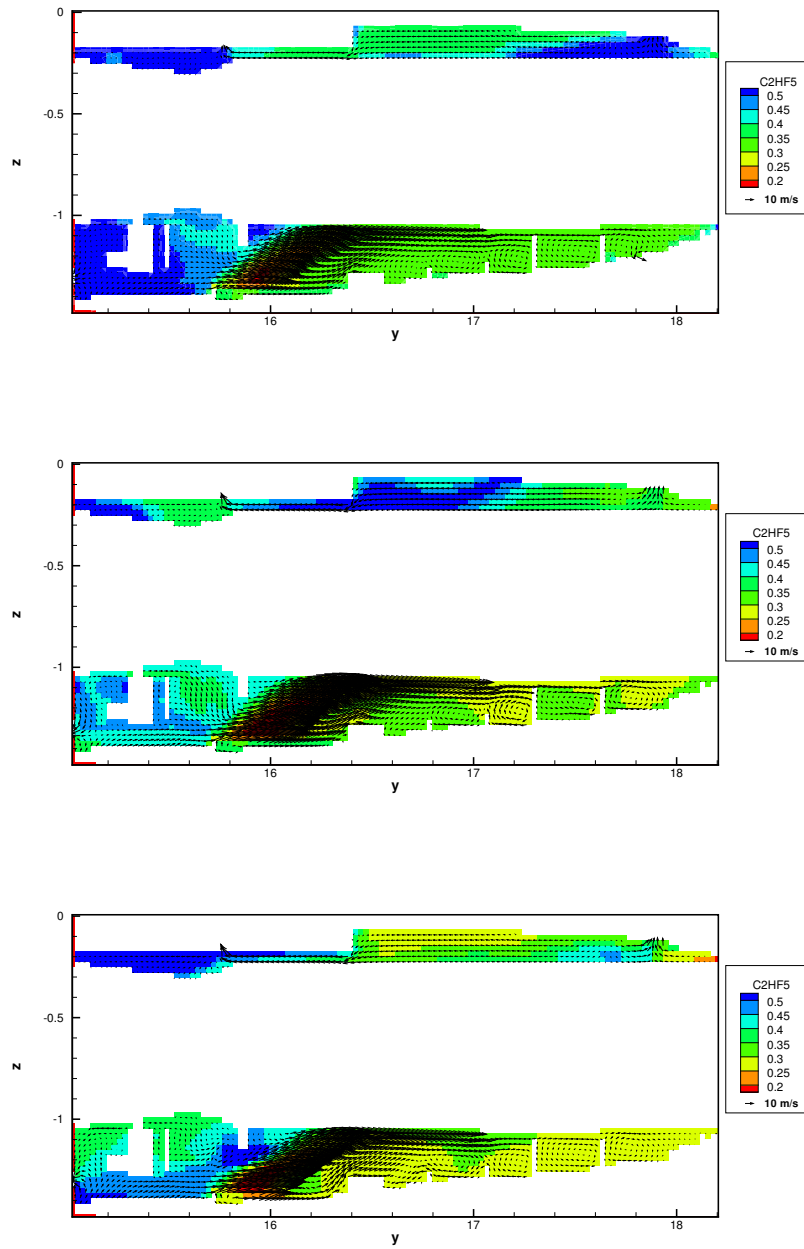
Figure 9: Contour plots of C_2HF_5 at 3.5 s after start of suppressant injection near the nacelle centerline, 0.63 m from the starboard reference point. Air flow into the nacelle is 0.66 kg/s (top) or 1.0 kg/s (center, bottom). Suppressant flow is 3.2 kg over 3 s (top, center) or over 4 s (bottom).
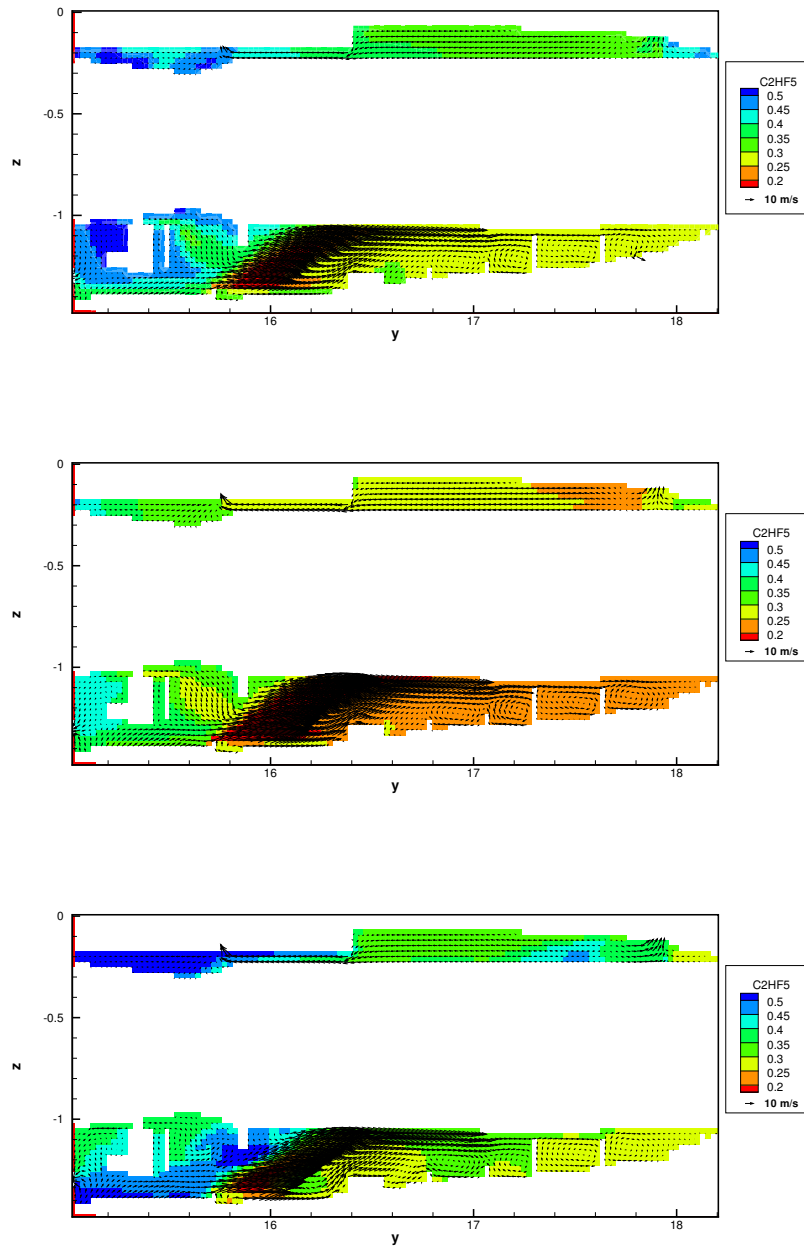
Figure 10: Contour plots of C_2HF_5 at 4.0 s after start of suppressant injection near the nacelle centerline, 0.63 m from the starboard reference point. Air flow into the nacelle is 0.66 kg/s (top) or 1.0 kg/s (center, bottom). Suppressant flow is 3.2 kg over 3 s (top, center) or over 4 s (bottom).
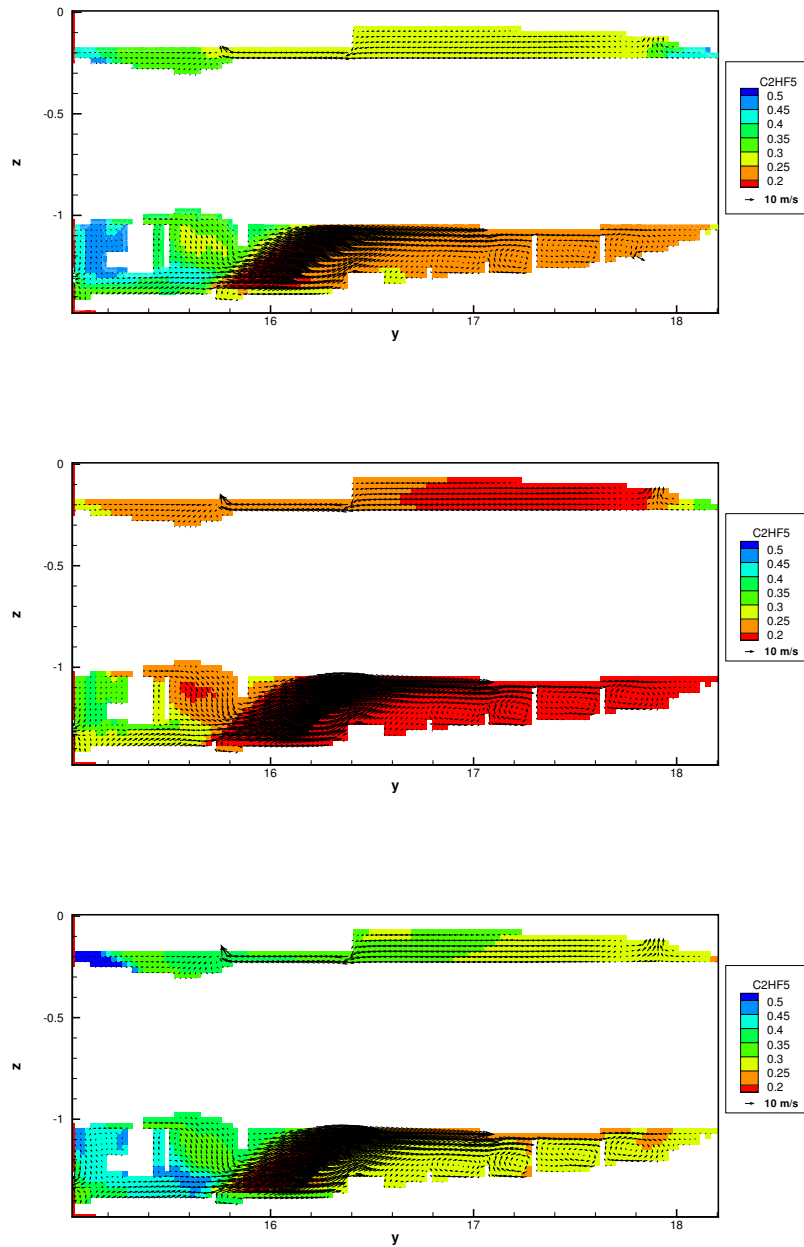
Figure 11: Contour plots of C_2HF_5 at 4.5 s after start of suppressant injection near the nacelle centerline, 0.63 m from the starboard reference point. Air flow into the nacelle is 0.66 kg/s (top) or 1.0 kg/s (center, bottom). Suppressant flow is 3.2 kg over 3 s (top, center) or over 4 s (bottom).
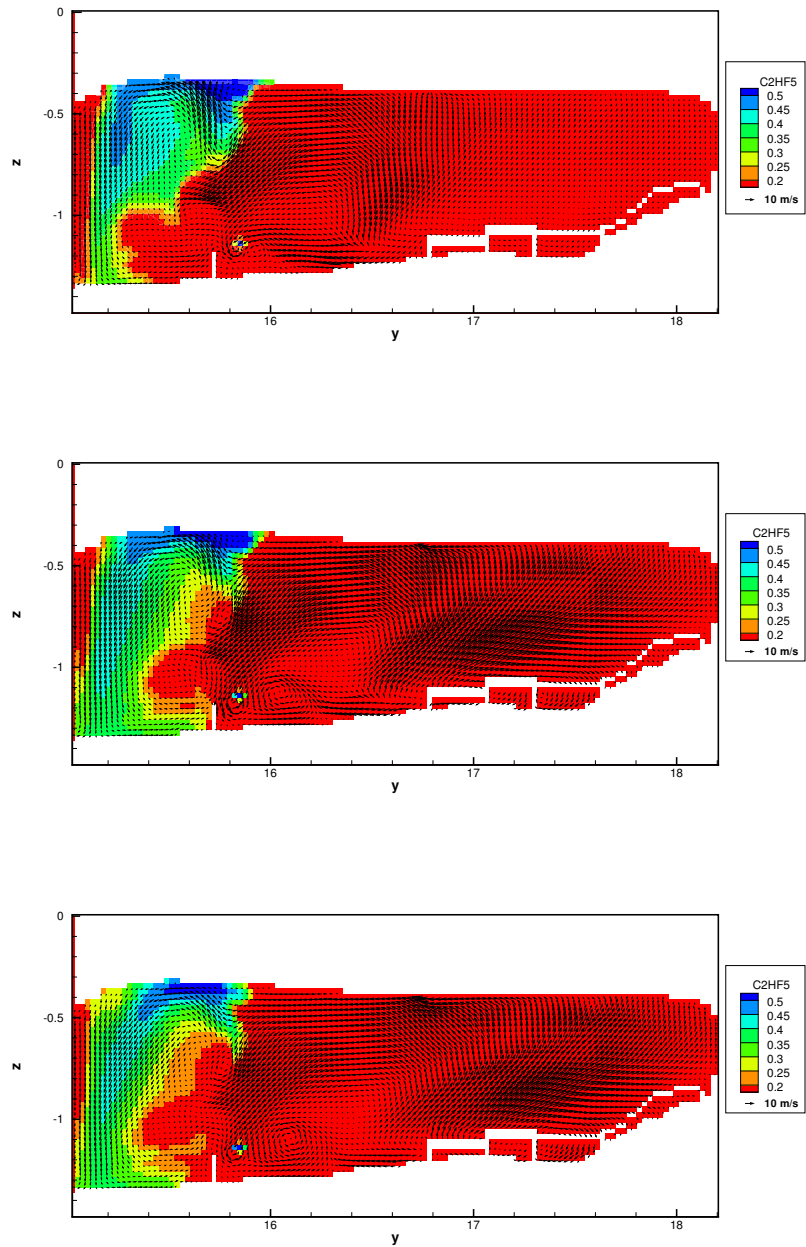
Figure 12: Contour plots of C_2HF_5 at 0.5 s after start of suppressant injection on the starboard side of the engine, 0.20 m from the starboard reference point. Air flow into the nacelle is 0.66 kg/s (top) or 1.0 kg/s (center, bottom). Suppressant flow is 3.2 kg over 3 s (top, center) or over 4 s (bottom).
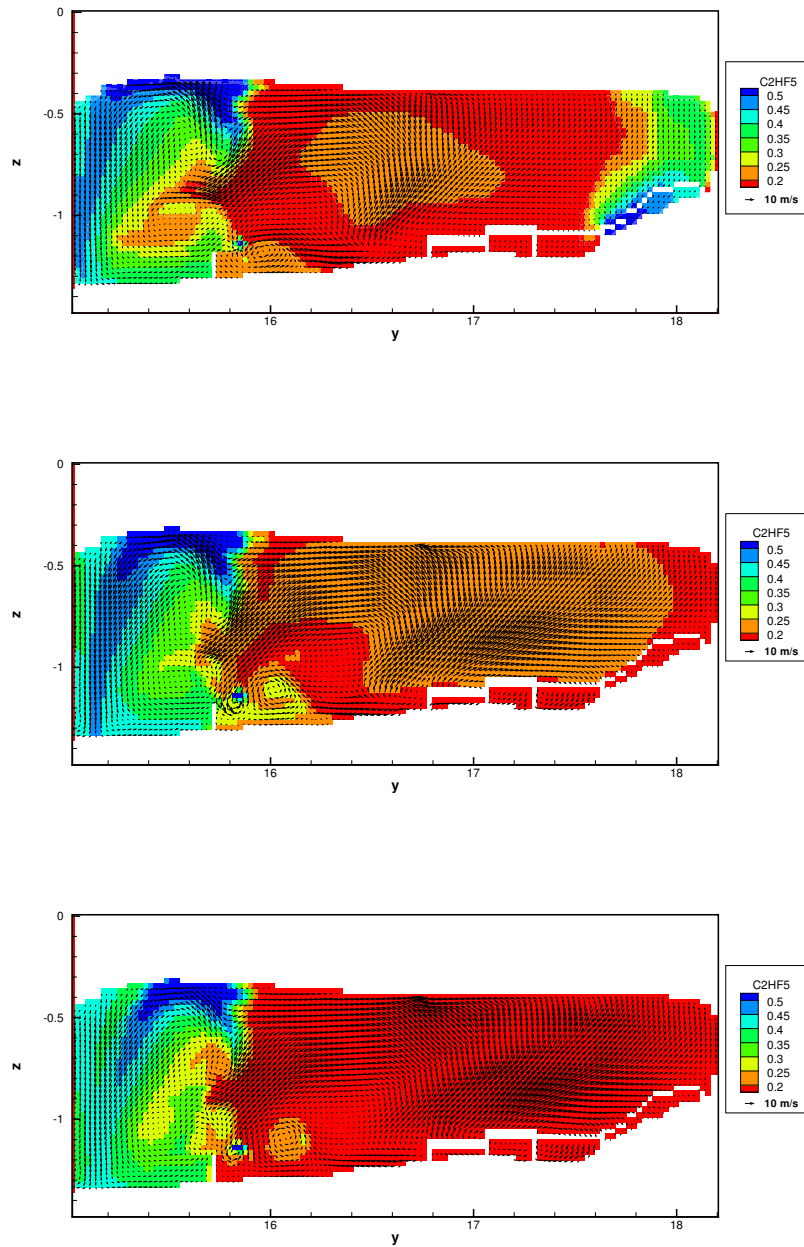
Figure 13: Contour plots of C_2HF_5 at 1.0 s after start of suppressant injection on the starboard side of the engine, 0.20 m from the starboard reference point. Air flow into the nacelle is 0.66 kg/s (top) or 1.0 kg/s (center, bottom). Suppressant flow is 3.2 kg over 3 s (top, center) or over 4 s (bottom).
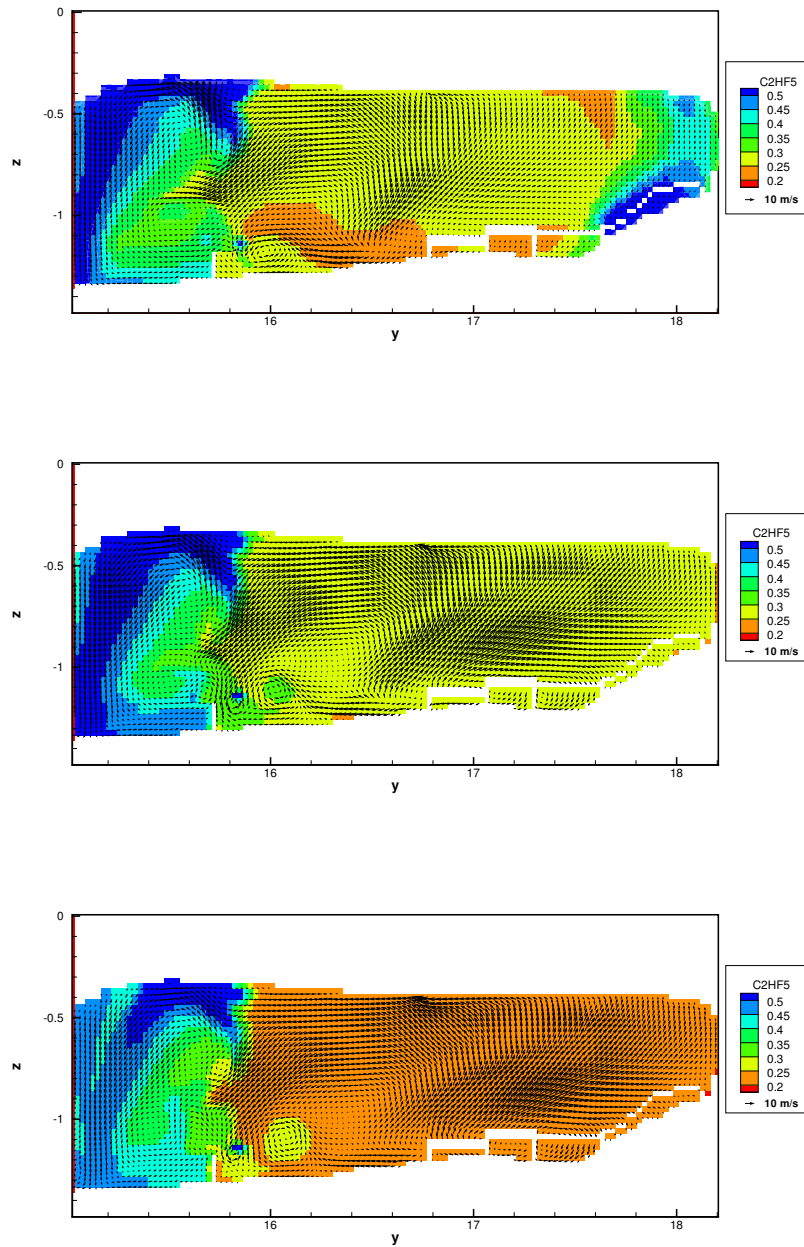
Figure 14: Contour plots of C_2HF_5 at 1.5 s after start of suppressant injection on the starboard side of the engine, 0.20 m from the starboard reference point. Air flow into the nacelle is 0.66 kg/s (top) or 1.0 kg/s (center, bottom). Suppressant flow is 3.2 kg over 3 s (top, center) or over 4 s (bottom).
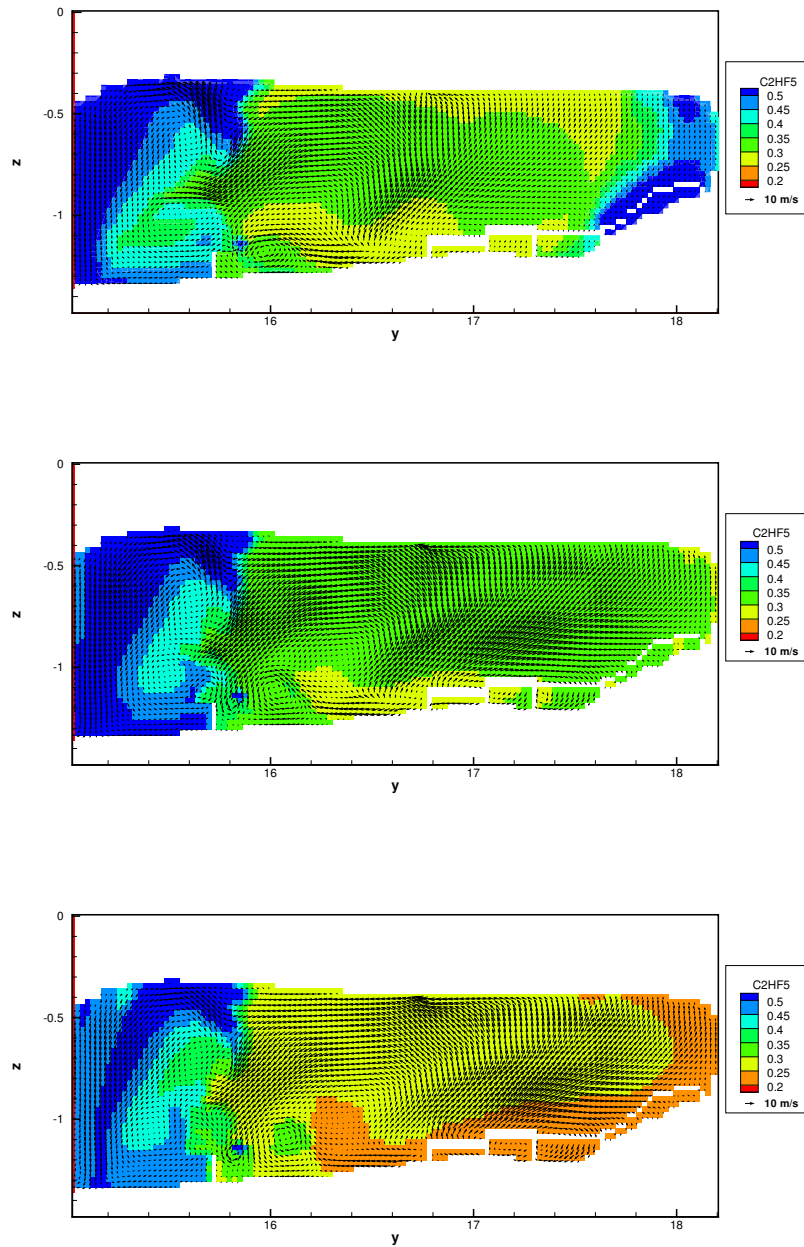
Figure 15: Contour plots of C_2HF_5 at 2.0 s after start of suppressant injection on the starboard side of the engine, 0.20 m from the starboard reference point. Air flow into the nacelle is 0.66 kg/s (top) or 1.0 kg/s (center, bottom). Suppressant flow is 3.2 kg over 3 s (top, center) or over 4 s (bottom).
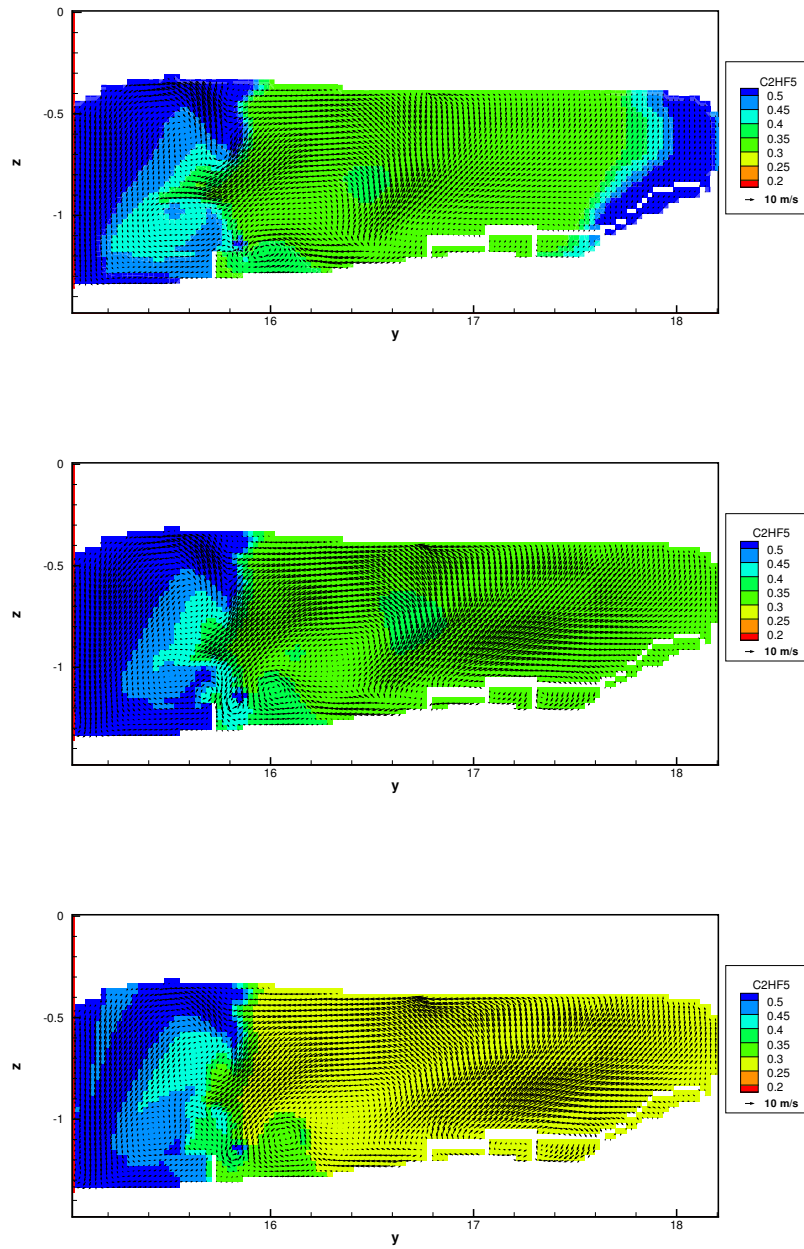
Figure 16: Contour plots of C_2HF_5 at 2.5 s after start of suppressant injection on the starboard side of the engine, 0.20 m from the starboard reference point. Air flow into the nacelle is 0.66 kg/s (top) or 1.0 kg/s (center, bottom). Suppressant flow is 3.2 kg over 3 s (top, center) or over 4 s (bottom).

43
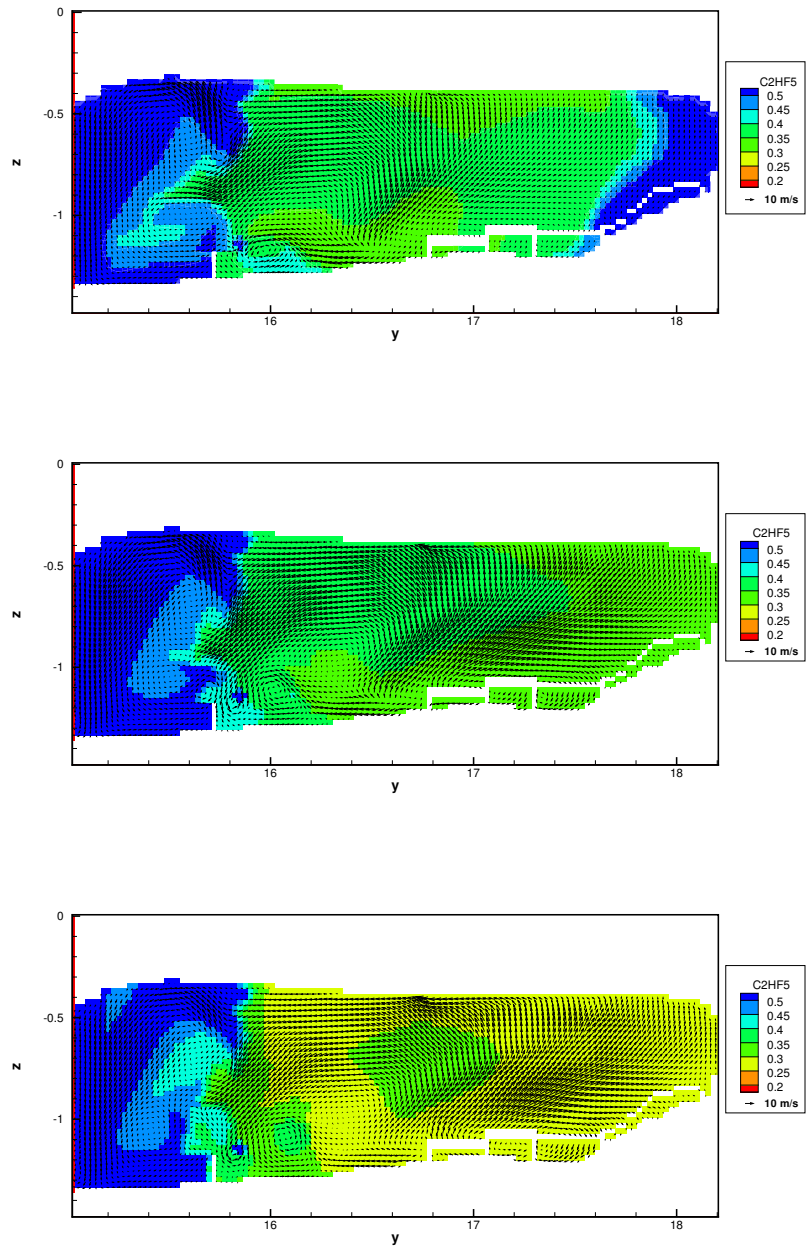
Figure 17: Contour plots of C_2HF_5 at 3.0 s after start of suppressant injection on the starboard side of the engine, 0.20 m from the starboard reference point. Air flow into the nacelle is 0.66 kg/s (top) or 1.0 kg/s (center, bottom). Suppressant flow is 3.2 kg over 3 s (top, center) or over 4 s (bottom).
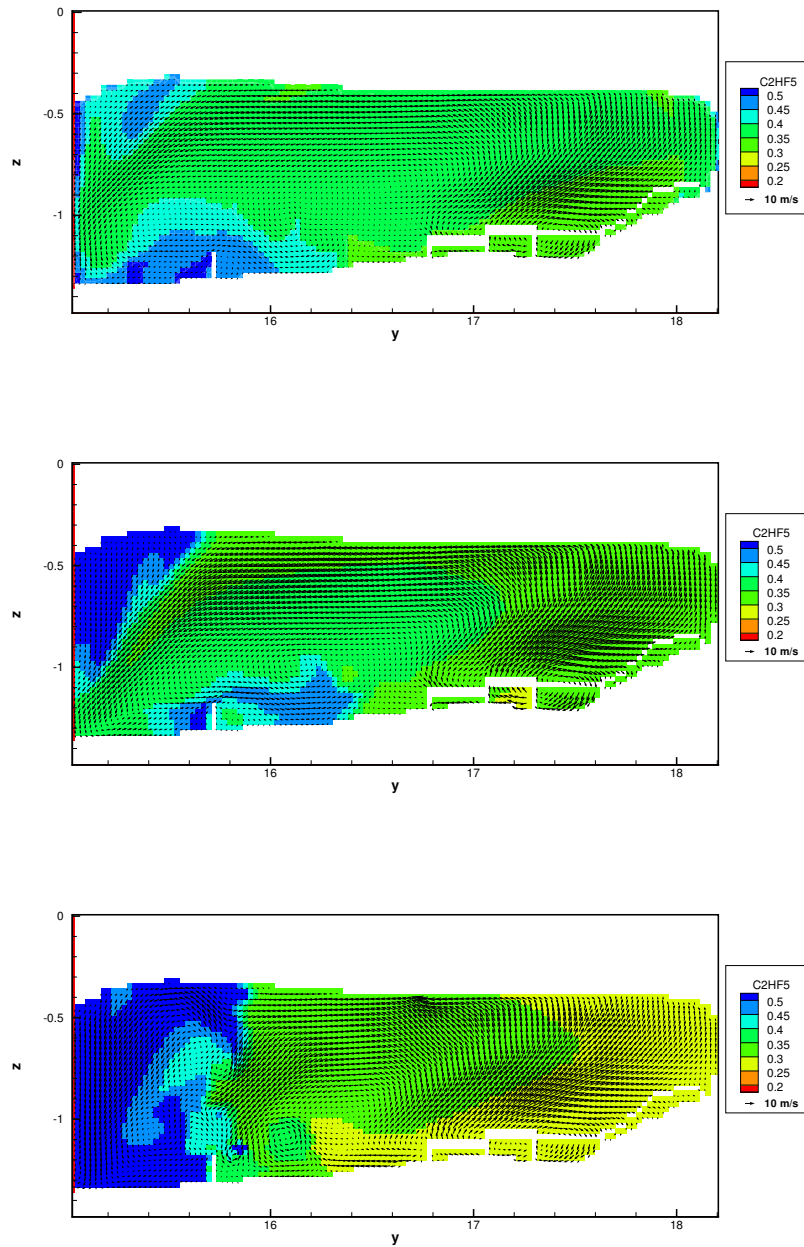
Figure 18: Contour plots of C_2HF_5 at 3.5 s after start of suppressant injection on the starboard side of the engine, 0.20 m from the starboard reference point. Air flow into the nacelle is 0.66 kg/s (top) or 1.0 kg/s (center, bottom). Suppressant flow is 3.2 kg over 3 s (top, center) or over 4 s (bottom).
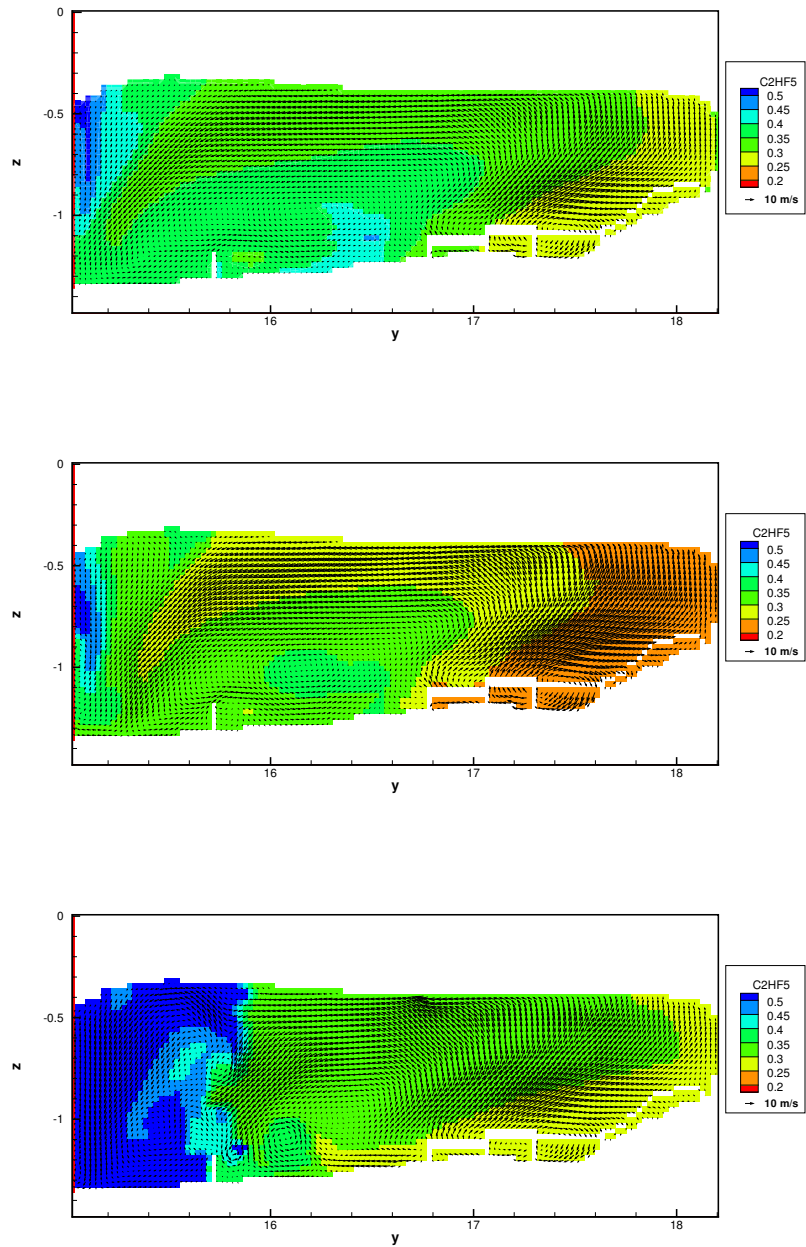
Figure 19: Contour plots of C_2HF_5 at 4.0 s after start of suppressant injection on the starboard side of the engine, 0.20 m from the starboard reference point. Air flow into the nacelle is 0.66 kg/s (top) or 1.0 kg/s (center, bottom). Suppressant flow is 3.2 kg over 3 s (top, center) or over 4 s (bottom).
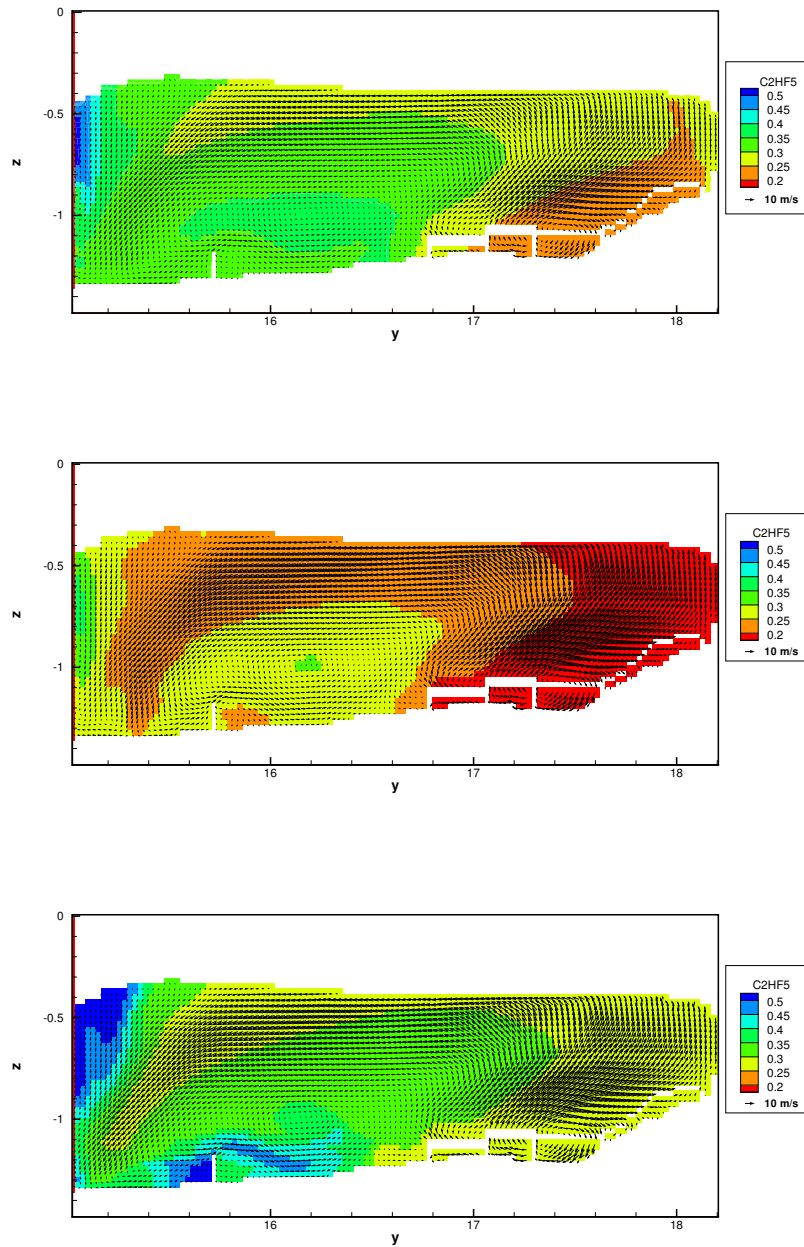
Figure 20: Contour plots of C_2HF_5 at 4.5 s after start of suppressant injection on the starboard side of the engine, 0.20 m from the starboard reference point. Air flow into the nacelle is 0.66 kg/s (top) or 1.0 kg/s (center, bottom). Suppressant flow is 3.2 kg over 3 s (top, center) or over 4 s (bottom).
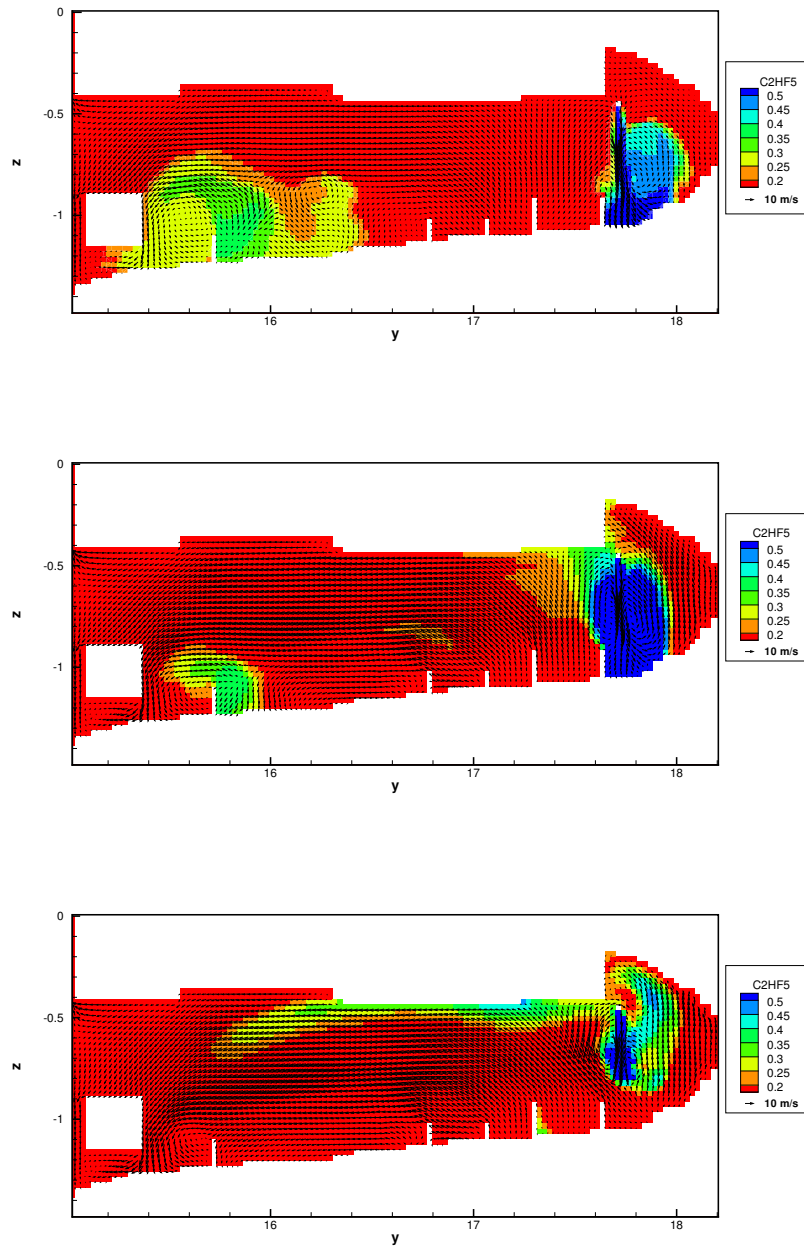
Figure 21: Contour plots of C_2HF_5 at 0.5 s after start of suppressant injection on the port side of the engine, 1.06 m from the starboard reference point. Air flow into the nacelle is 0.66 kg/s (top) or 1.0 kg/s (center, bottom). Suppressant flow is 3.2 kg over 3 s (top, center) or over 4 s (bottom).
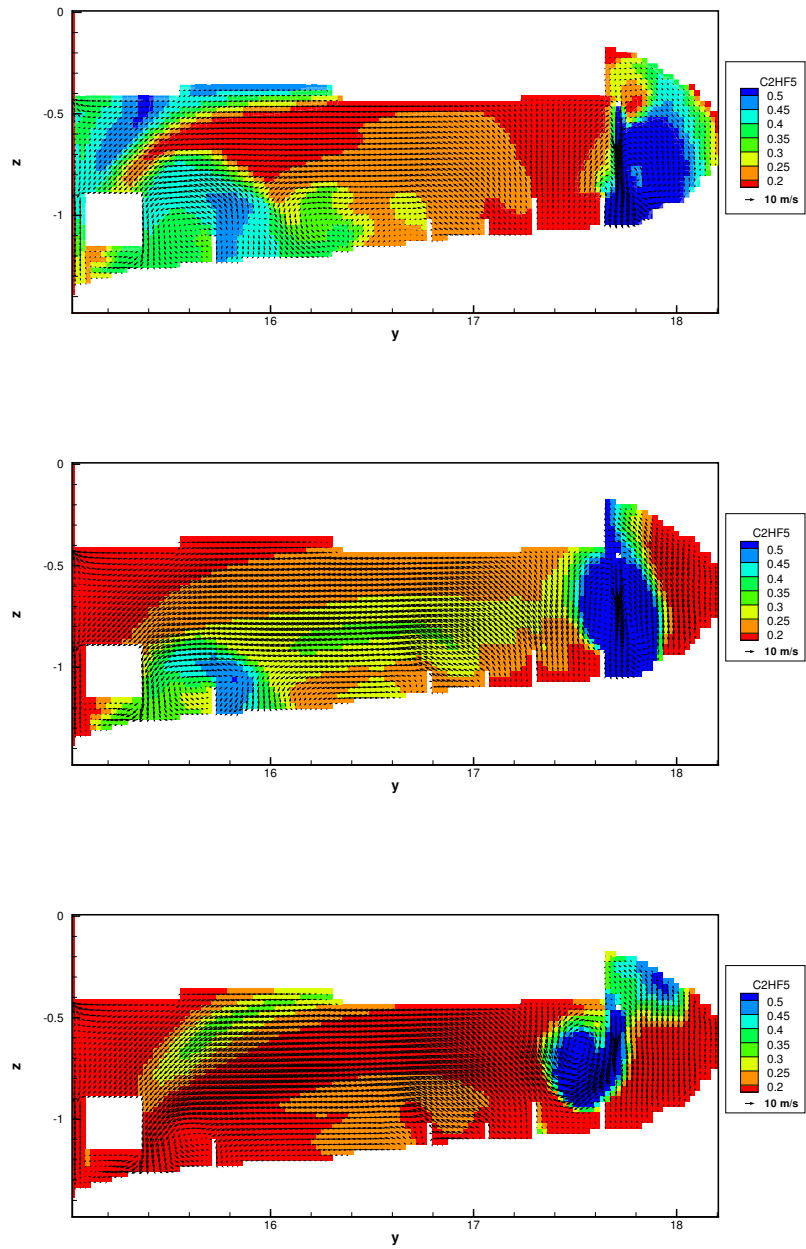
Figure 22: Contour plots of C_2HF_5 at 1.0 s after start of suppressant injection on the port side of the engine, 1.06 m from the starboard reference point. Air flow into the nacelle is 0.66 kg/s (top) or 1.0 kg/s (center, bottom). Suppressant flow is 3.2 kg over 3 s (top, center) or over 4 s (bottom).
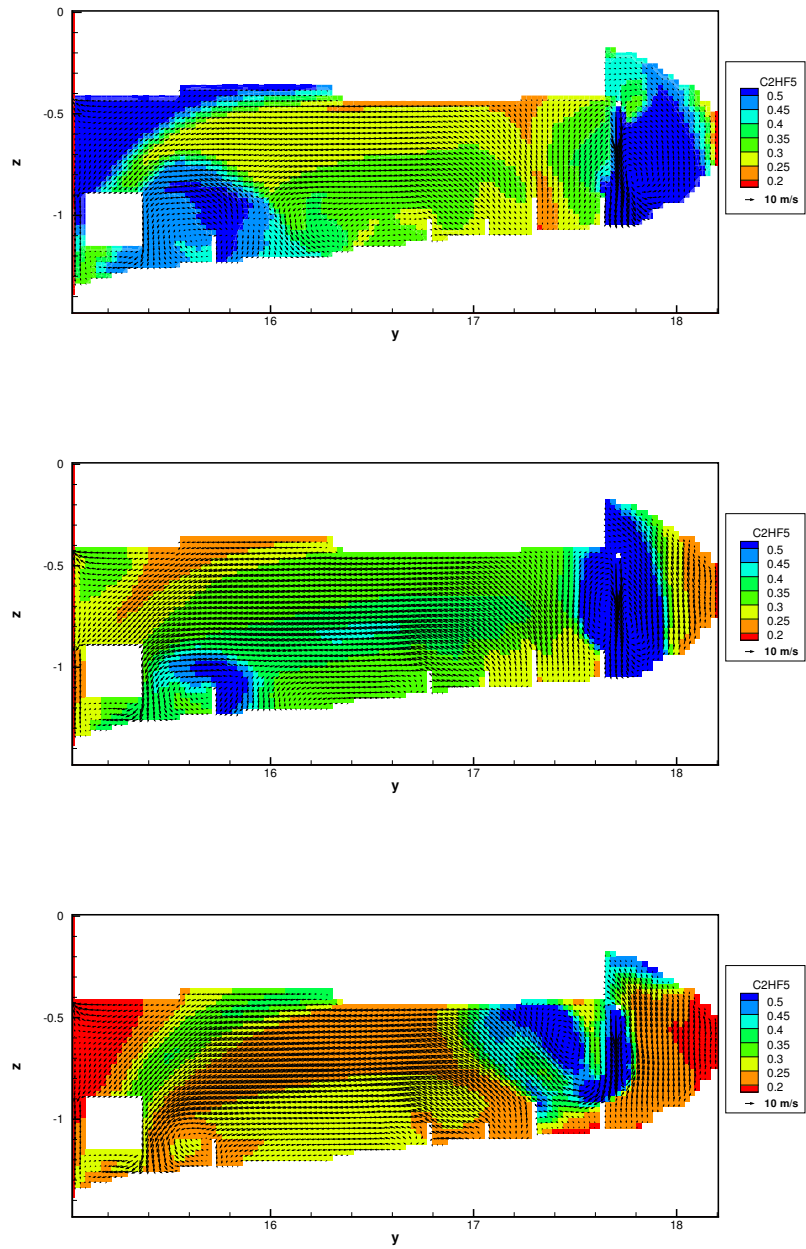
Figure 23: Contour plots of C_2HF_5 at 1.5 s after start of suppressant injection on the port side of the engine, 1.06 m from the starboard reference point. Air flow into the nacelle is 0.66 kg/s (top) or 1.0 kg/s (center, bottom). Suppressant flow is 3.2 kg over 3 s (top, center) or over 4 s (bottom).
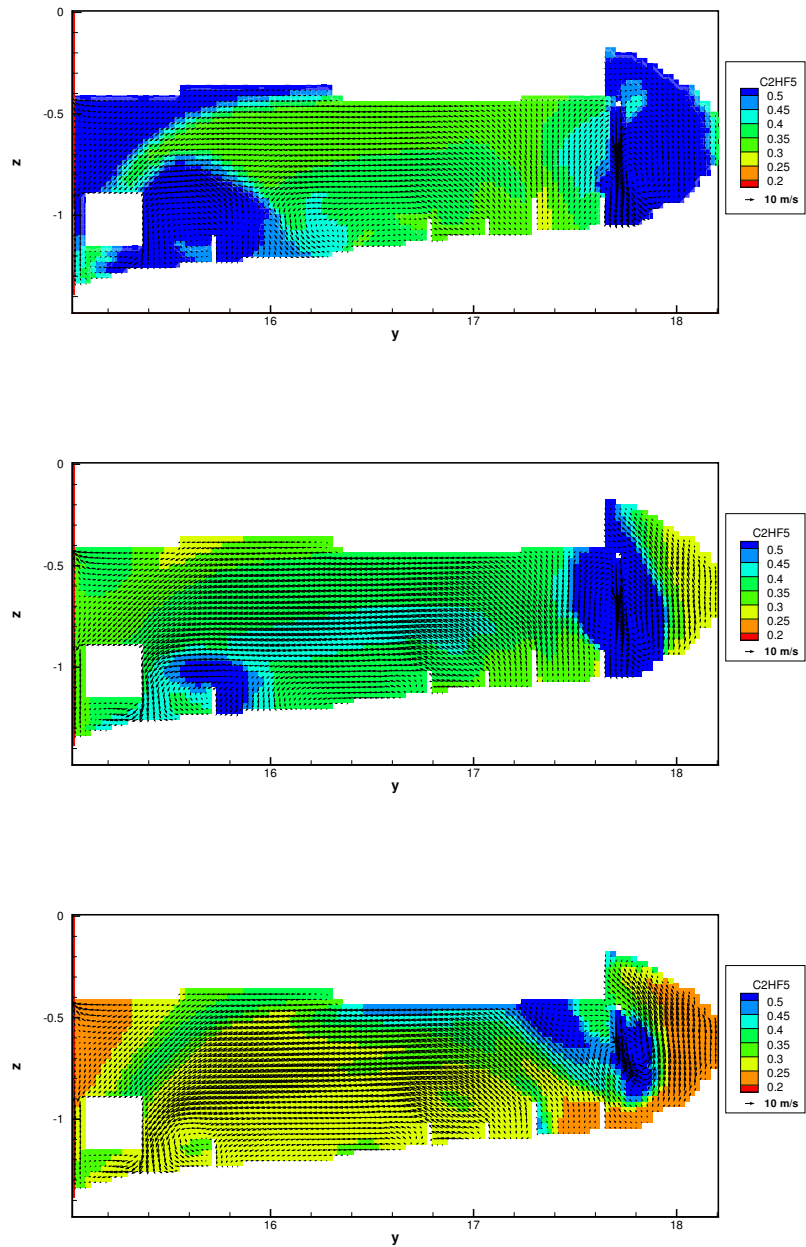
Figure 24: Contour plots of C_2HF_5 at 2.0 s after start of suppressant injection on the port side of the engine, 1.06 m from the starboard reference point. Air flow into the nacelle is 0.66 kg/s (top) or 1.0 kg/s (center, bottom). Suppressant flow is 3.2 kg over 3 s (top, center) or over 4 s (bottom).
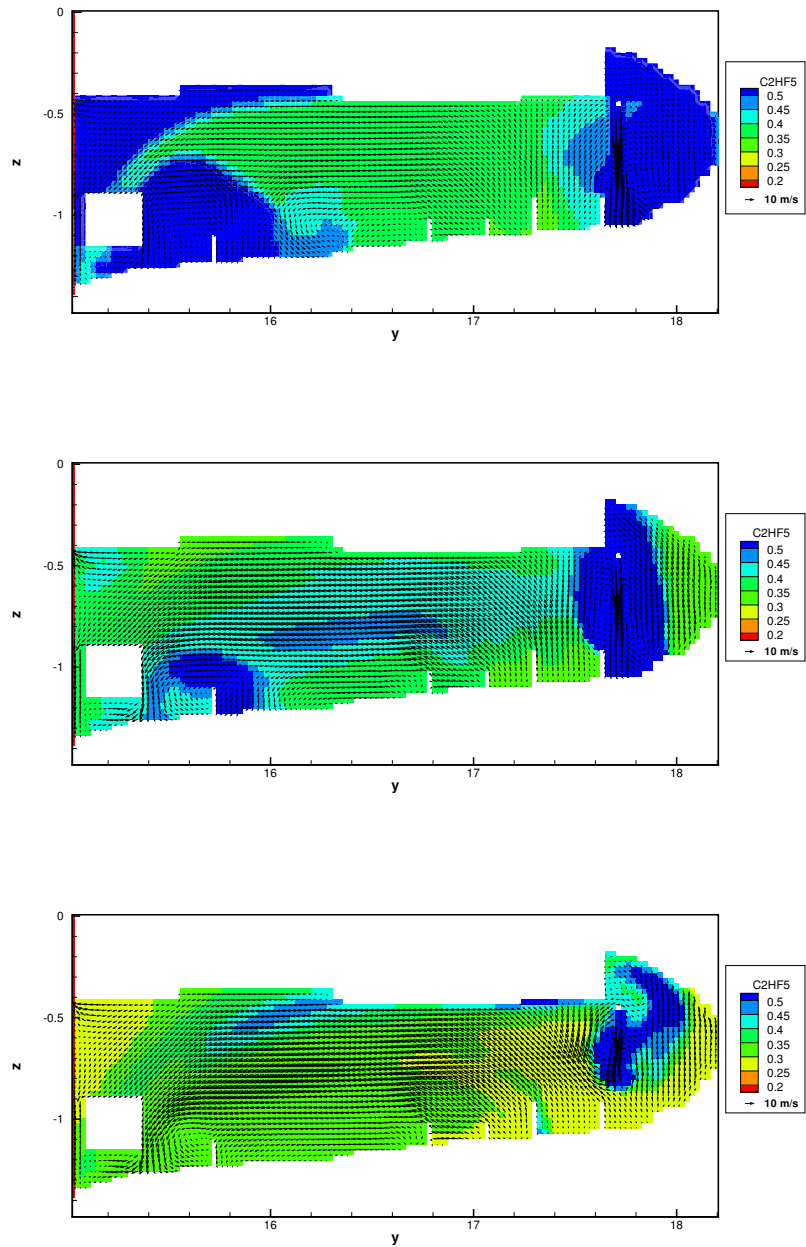
Figure 25: Contour plots of C_2HF_5 at 2.5 s after start of suppressant injection on the port side of the engine, 1.06 m from the starboard reference point. Air flow into the nacelle is 0.66 kg/s (top) or 1.0 kg/s (center, bottom). Suppressant flow is 3.2 kg over 3 s (top, center) or over 4 s (bottom).
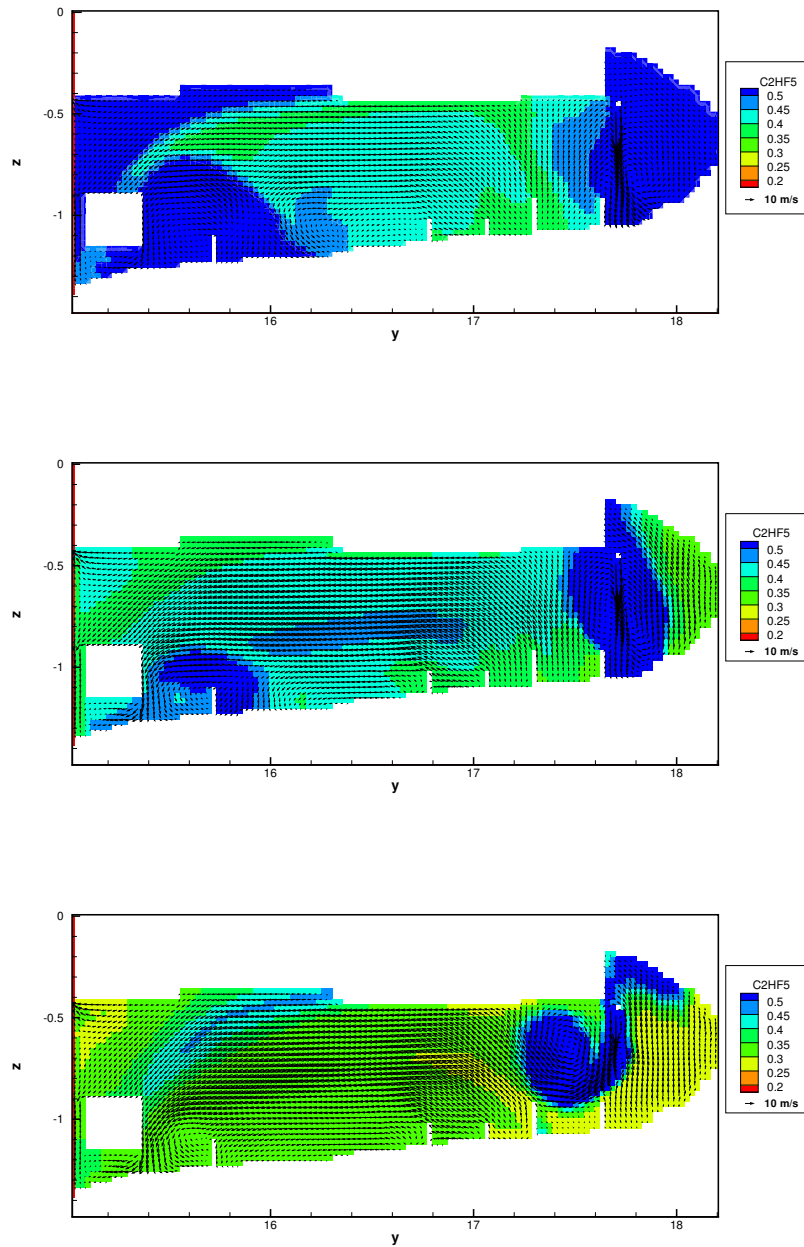
Figure 26: Contour plots of C_2HF_5 at 3.0 s after start of suppressant injection on the port side of the engine, 1.06 m from the starboard reference point. Air flow into the nacelle is 0.66 kg/s (top) or 1.0 kg/s (center, bottom). Suppressant flow is 3.2 kg over 3 s (top, center) or over 4 s (bottom).
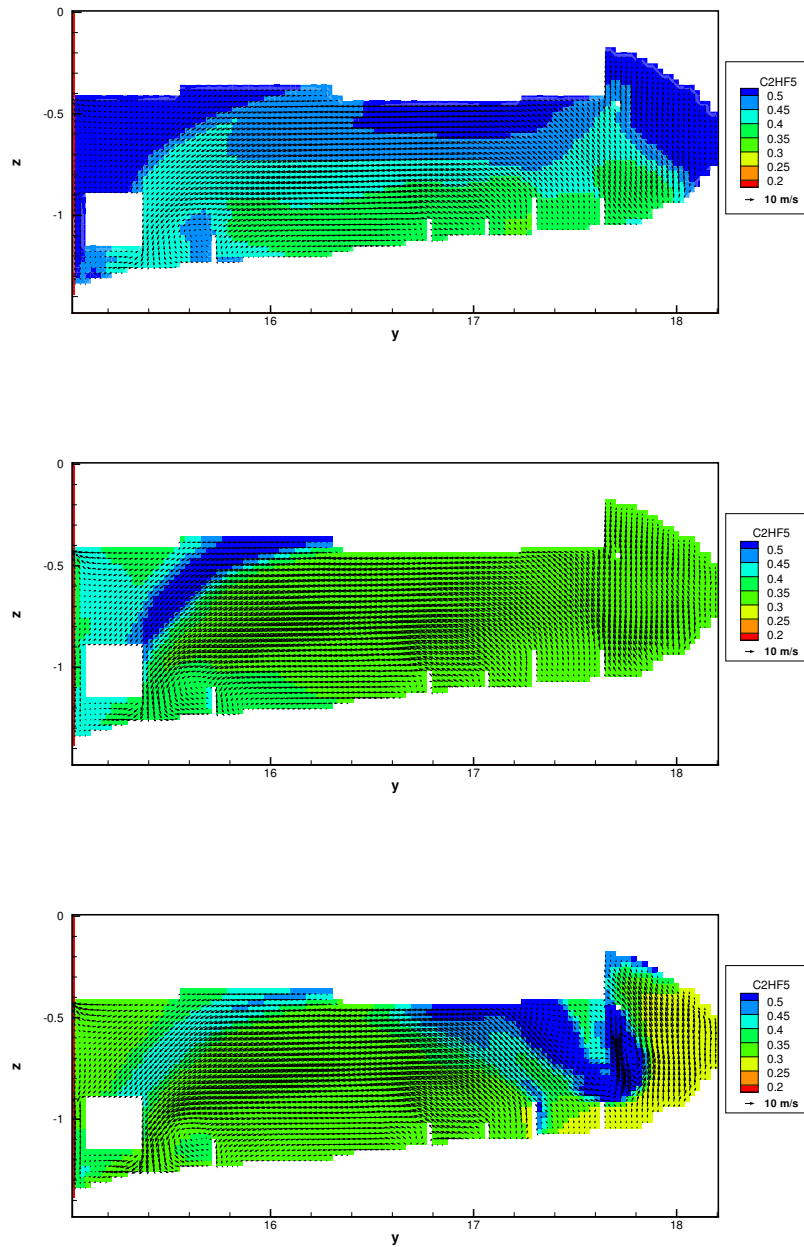
Figure 27: Contour plots of C_2HF_5 at 3.5 s after start of suppressant injection on the port side of the engine, 1.06 m from the starboard reference point. Air flow into the nacelle is 0.66 kg/s (top) or 1.0 kg/s (center, bottom). Suppressant flow is 3.2 kg over 3 s (top, center) or over 4 s (bottom).
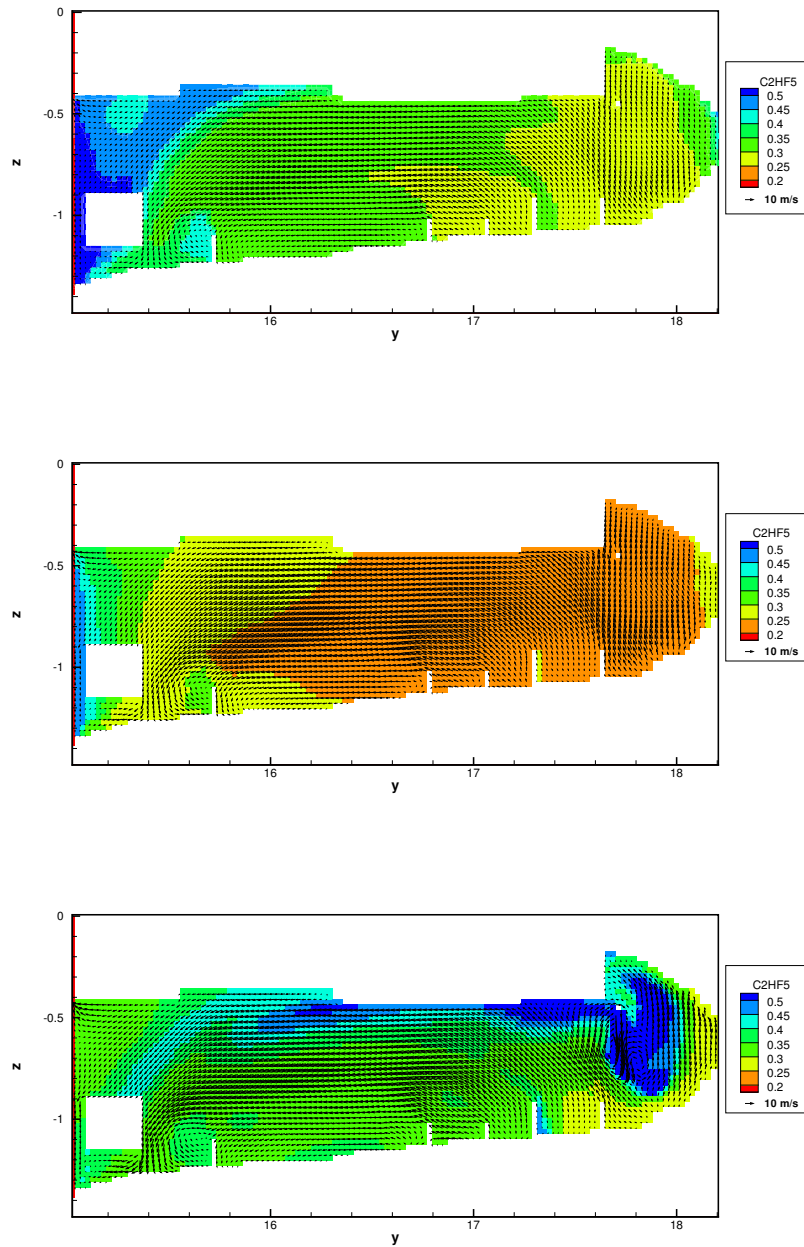
Figure 28: Contour plots of C_2HF_5 at 4.0 s after start of suppressant injection on the port side of the engine, 1.06 m from the starboard reference point. Air flow into the nacelle is 0.66 kg/s (top) or 1.0 kg/s (center, bottom). Suppressant flow is 3.2 kg over 3 s (top, center) or over 4 s (bottom).
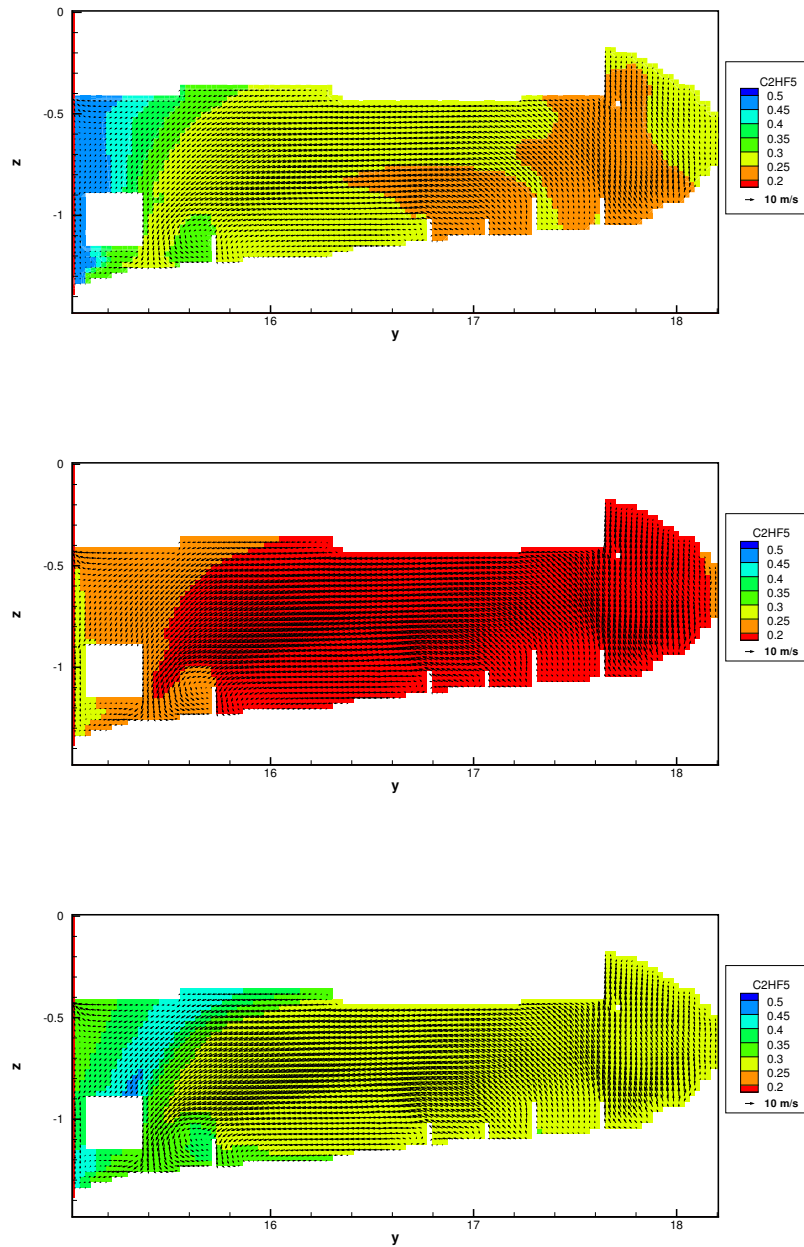
Figure 29: Contour plots of C_2HF_5 at 4.5 s after start of suppressant injection on the port side of the engine, 1.06 m from the starboard reference point. Air flow into the nacelle is 0.66 kg/s (top) or 1.0 kg/s (center, bottom). Suppressant flow is 3.2 kg over 3 s (top, center) or over 4 s (bottom).

Table II: The locations of Halonizer probes

	Qualification Report [25]		Simulation		
Channel	y [m]		x [m]	y [m]	z [m]
1	15.27	7:00	.84	15.27	-1.07
2	15.29	12:00	.60	15.29	-.23
3	16.35	3:00	.15	16.35	-.65
4	16.35	12:00	.58	16.35	-.20
5	17.26	2:30	.17	17.26	-.46
6	17.26	6:00	.60	17.26	-1.18
7	17.26	10:30	1.00	17.26	-.46
8	17.98	12:00	.60	17.98	-.20
9	17.98	4:30	.25	17.98	-.97
10	17.98	7:30	.95	17.98	-.97
11	15.63	7:30	.82	15.63	-1.02
12	15.81	7:30	.98	15.81	-1.05

7 HFC-125 concentration histories at specific locations

To evaluate the predictive capability of the simulations in describing the suppressant distribution in the na-celle, we have compared HFC-125 concentration-time traces with those measured using a Halonizer in the F-18 qualification tests [20, 25]. These comparisons are shown in Figs. 30 and 31. There is an unknown uncertainty associated with the Halonizer concentration measurements, both in terms of the absolute con-centration measured and, significantly, in the locations where the measurements were taken. The indications from the qualification test report are that the measurements are fairly repeatable so that significant errors are most likely of the systematic type. The probe locations are not specified in detail in the report; for example, the probe corresponding to channel 1 is identified as being 604 inches aft of the aircraft nose and at 7:00. This places it roughly in front of the upper port edge of the gearbox assembly, but there is some latitude on the exact placement. The stated locations and the coordinates used in the simulations are indicated in Table II. Each probe location within the simulation represents an average over one cubic inch of volume.

While the agreement described in the following paragraphs is reasonable, it also highlights model sen-sitivities in the areas of (1) the suppressant spray momentum vector direction and magnitude relative to the air inflow and (2) the rate of suppressant vaporization. To indicate the effect of the relative momentum, simulations are conducted with the 3.2 kg of HFC-125 injected in the gas phase over either a 3 or 4 s in-jection period; this represents a 30% change in the jet momentum. It is evident in Figs. 30 and 31 that this modest change in the suppressant momentum can lead to as much as a 50% change in the concentration predicted at a specific point. This substantial concentration variation arises because the high-concentration suppressant-jet centerlines either hit a measurement location or are shifted by perhaps 10 cm to the side of

the measurement location. This highlights both the sensitivity to the spray momentum and the sensitivity to the Halonizer-probe locations. Because of this enormous sensitivity, we have only moderate confidence in the significance of agreement or disagreement in these results. More significant are the general trends discussed below.

In these simulations, the suppressant has been assumed to enter the nacelle in the vapor phase or instantly vaporize upon entering. Other simulations, not reported here, indicate that there is a finite vaporization time. This actual vaporization time will depend on the square of the initial particle diameters, assuming a d^2-vaporization rate, but reasonable droplet diameters (100 to 500 μm) have estimated evaporation times of 0.1 to 2.5 s. These estimates assume flash vaporization of roughly a third of the suppressant acts to substantially cool the remaining liquid suppressant to its boiling point. While relatively few large droplets are expected, this highlights the need to understand the droplet size distribution leaving the suppressant nozzles. The effects of finite-rate evaporation are clear in the qualification test measurements in Figs. 30 and 31 where the suppressant concentrations drop off more gradually than simulated after the end of the 3 or 4 s injection. The concentrations also rise more gradually than predicted.

The various Halonizer measurement channels have been grouped roughly according to their locations in the nacelle. In the upper pane of Fig. 30 are measurements located in the upper forward quadrant of the nacelle, channels 2, 3 and 4. Channel 2 is near the front of the nacelle while 3 and 4 are almost half way aft. Channels 2 and 4 are located at 12:00, along the top of the nacelle, while 3 is located on the starboard side. Results for channels 3 and 4 are reasonably good, with 3 and 4 s injection periods roughly bounding the measurements. Predictions for channel 2 are consistently high and this implies that much more suppressant is predicted to move to the forward nacelle than is measured. This implies that the flow from nozzle 1 (up the starboard side) should be turned forward less than shown in Figs. 3 through 29. The reason that this would occur is unclear, but it could imply that much more suppressant goes out the balance piston or that the dominant flow path is circumferentially around the engine where it narrows at 15.6 m.

In the lower pane of Fig. 30 are the Halonizer channels that are located in the lower forward quadrant of the nacelle with channel 1 in front of and channels 11 and 12 behind the gearbox assembly and over the air inlet. Suppressant in this region comes primarily from nozzle 1 (over the top of the engine) and from nozzle 2 (under the engine). Measurements for all three channels here bounded by the 3 and 4 s injections with the shorter, higher momentum injection giving the higher concentrations since it is better able to cross the air inlet and reach the probe locations without being dispersed downstream. For channel 12 the concentration differences for the two suppressant injection rates exceed a factor of two.

Because the turbulence generated by the suppressant injection is also not well known, we have also varied this parametrically to determine its sensitivity. The concentrations measured by probe channels 11 and 12 do show some sensitivity to turbulence levels generated by the spray nozzles: a two-order of magnitude increase in the level of turbulence in the initial spray (3 s injection) brings the concentration profiles for

channels 11 and 12 into good agreement with the Halonizer measurements. These are the only results reported that show more than a few percent variation with a substantial change in the suppressant-injection turbulence levels; we conclude that the sensitivity to the injection momentum and the turbulence generated as the suppressant mixes is more substantial than the sensitivity to the turbulence imposed as a boundary condition.

In the upper pane of Fig. 31 are sensors located between nozzles 3 and 4, roughly two-thirds of the way aft. Channel 6 has been located below the engine and just in front of one large rib while channels 5 and 7 are located on the upper starboard and port sides respectively. Simulated results for channels 5 and 6 are relatively insensitive to the rate of injection and these simulations bound the measurements for those channels. Results for channel 7, which is located just ahead of nozzle 4, show that as the momentum of nozzle 4 is reduced there is a competition between the downward momentum from the suppressant injection and overall upward flow caused by the flow from the air inlet to the upper diamond vent. This creates strong oscillations in the flow field for the 4 s duration injection that are visible Figs 21 through 29 as well as in Fig. 31. The relatively high suppressant concentrations measured for channel 7 with the Halonizer imply that some (steady) forward flow from nozzle 4 is occurring in the simulator that is not picked up for these conditions in the simulations (or that nozzle 4 is directed in a forward direction by a few degrees).

Certain probes (channels 8, 9, and 10) were listed in the qualification test report [25] with locations beyond the aft end of the aircraft; we have located these in the afterburner vane region where there were sensor ports in the fuselage that did not correspond to listed probe locations. The Halonizer measurements shown in the lower pane of Fig. 31 correspond to these channels. The predictions are substantially lower because we have neglected to model the afterburner control vanes that are in the vicinity of these probes; such vanes would act to better mix the flow in this region.

We note that the discrepancies noted above in the measured concentrations do not indicate a change in state from one where suppression is expected to one where suppression is not expected, or vice versa. When the simulations or Halonizer probe measurements differ noticeably, one shows a concentration that is sufficient to suppress a fire while the other shows a concentration markedly higher than the mean concentration, indicating that the suppressant spray is still highly concentrated when it reaches that probe location.

8   On the sufficient distribution of suppressant throughout the nacelle

As an integral measure of the sufficiency of suppressant distribution in the nacelle, we have tracked the fraction of the nacelle volume for which the suppressant mass fraction exceed 30%. Even with low intensity mixing, this is a generally sufficient level for suppression and represents a conservative estimate of suppression ability. Figure 32 shows this fraction when the air flow rate is 1.0 kg/s with varying rates of suppressant injection (same mass over different durations). The mass of suppressant to be injected was fixed at 3.2 kg
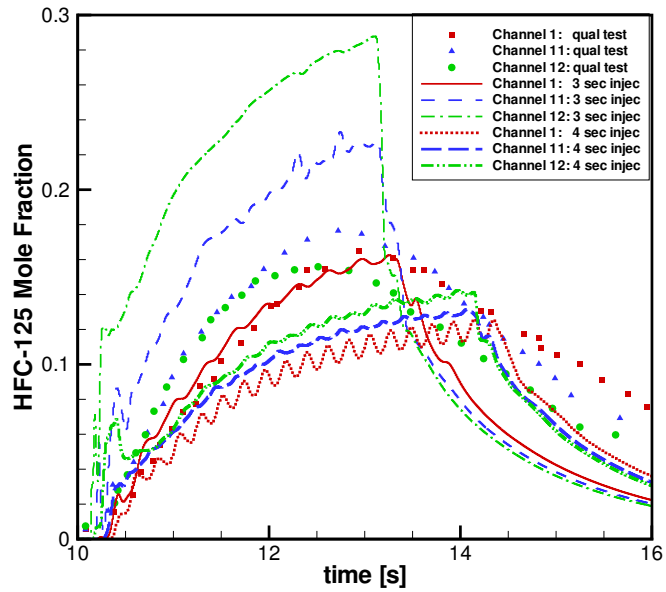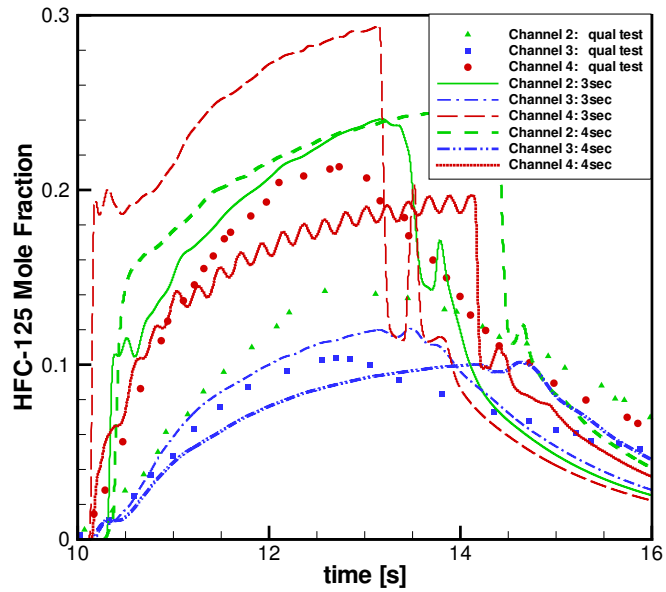
Figure 30: HFC-125 mole fractions at Halonizer sensor locations. Measurements during the qualification tests [25] are compared with simulations with 3.2 kg of HFC-125 injected over 3 s and 4 s. Air flow into the nacelle is 1.0 kg/s and suppressant mass flow is proportional to the nozzle area for four production nozzles.
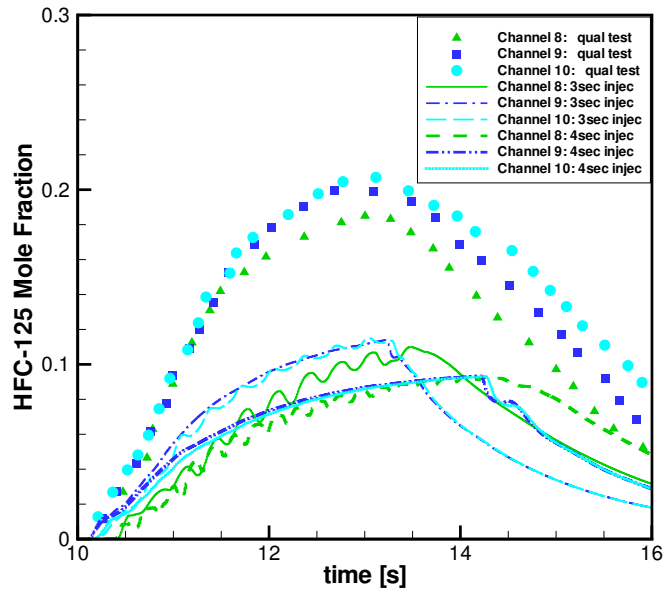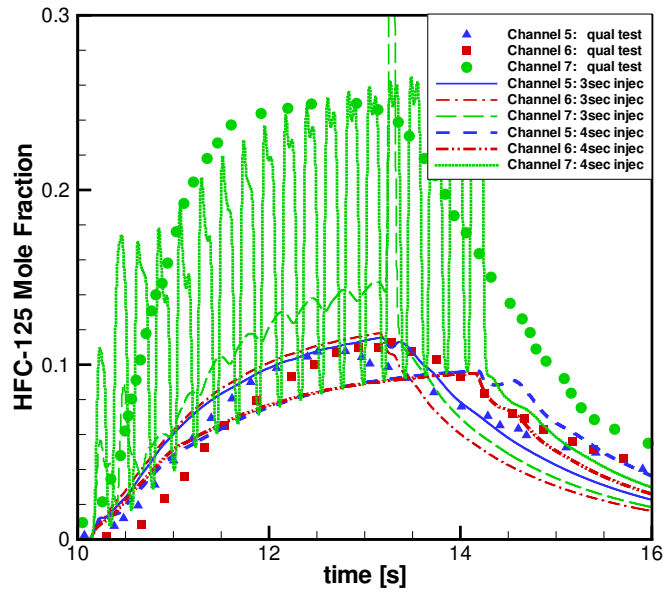
Figure 31: HFC-125 mole fractions at Halonizer sensor locations. Measurements during the qualification tests [25] are compared with simulations with 3.2 kg of HFC-125 injected over 3 s and 4 s. Air flow into the nacelle is 1.0 kg/s and suppressant mass flow is proportional to the nozzle area for four production nozzles.

and the period over which it was released varied from 2 to 6 s. Shorter injection periods would correspond to higher bottle pressures driving the injection process. To the extent that suppressant vaporization is slow, the period over which the suppressant is *effectively* injected will increase. Figure 32 shows that the entire volume is essentially filled for at least one second for injection durations of 3 s or less. For longer periods of injection, the volume is not filled with high concentrations since suppressant is continually swept out the various vents. The failure to completely fill the nacelle does not indicate that suppression will not occur, but that one is in a less conservative regime where suppression confidence is reduced.
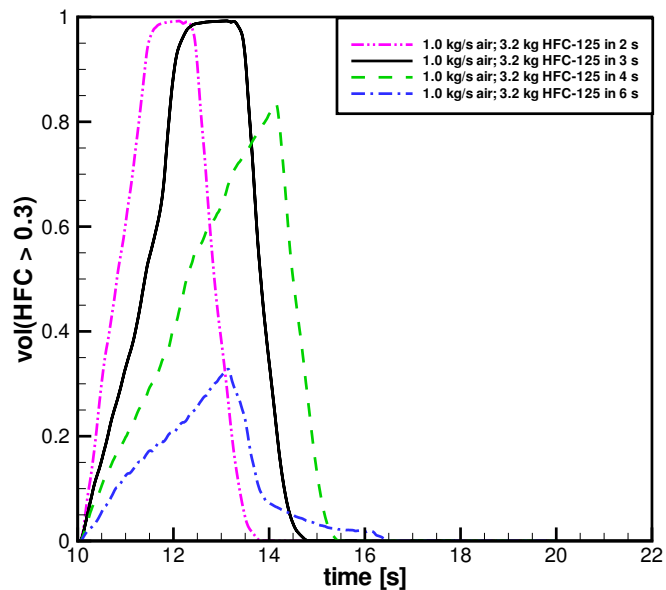
Figure 32: Fraction of the nacelle internal volume for which HFC-125 mass fractions exceeds 0.3 with 1.0 kg/s air flow into the nacelle. The mass of HFC-125 injected is 3.2 kg, injected over various periods as indicated with mass flow through each nozzle proportional to the measured nozzle-throat area.

The peak average suppressant mass fraction estimated with Eq. 9 for the simulations shown in Fig. 32 are 0.59, 0.51, 0.44 and 0.35 with smaller mass fractions corresponding to the longer injection duration. This indicates that, if the the turbulent mixing in the nacelle were sufficient to create homogeneity, the mass fraction throughout the nacelle would exceed 0.3 for all of these scenarios. Clearly, inhomogeneities arising from imperfect mixing are significant. This indicates that, while an analysis as in Sec. 3 does provide an indication of the trends, the CFD analysis can provide significant information on the degree of inhomogeneity. Specifically the CFD analysis can provide an estimate of the volume that fails to meet a criteria such as the one indicated here (suppressant mass fractions exceeding 0.3). The inhomogeneities that are observed

62

in the simulations are attributable to finite turbulent mixing rates. That is, the nacelle vapors are swept out of the nacelle (displaced by incoming air and suppressant) before they have had time to become sufficiently homogeneous. The rate of turbulent mixing is largely dependent on the turbulent kinetic energy and the length scales in the nacelle. Within this given nacelle the length scales do not change (changing clutter would affect this, though), so that the turbulent kinetic energy drives the relative rates of mixing here. When the suppressant is injected at a slower rate (i.e. over 6 s), the suppressant injection generates less kinetic energy for mixing. This leads to greater inhomogeneities along with the lower average suppressant mass fraction, and this is reflected in Fig. 32.

Similar results are shown in Fig. 33 where the air flow rate is varied from 0.5 kg/s to 1.0 kg/s while the suppressant injection is held fixed at 3.2 kg over 3 s. Except for the fact that the suppressant resides in the nacelle for somewhat longer after the end of injection, the air flow rate has little effect on the distribution when all four nozzles are employed (different results are obtained in the following section with with some nozzles capped). This is not necessarily true if the suppressant is not filling the nacelle volume. In Fig. 34 the volume of the nacelle filled for the slowest rate of suppressant injection shown in Fig. 32 is compared with the volume filled when the air flow rate is reduced by half. While this is an extreme case, the volume filled does increase as the rate of dilution by the air is reduced.
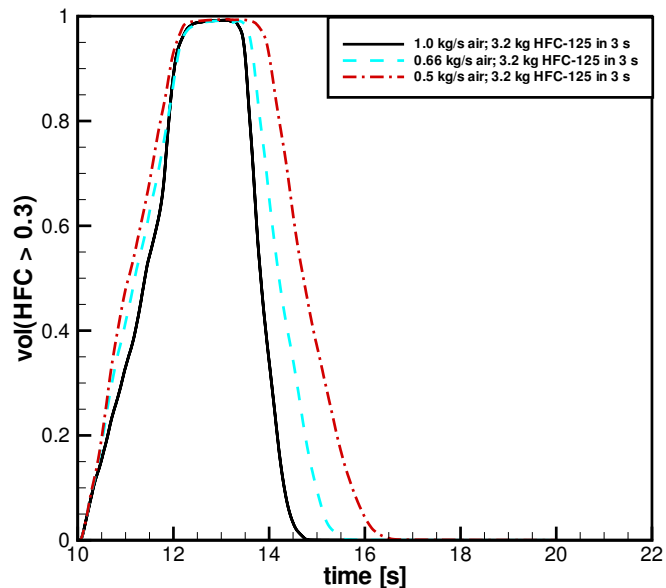
Figure 33: Fraction of the nacelle internal volume for which HFC-125 mass fractions exceeds 0.3 when 3.2 kg of HFC-125 is injected over 3 s. The air flow rate into the nacelle is 0.5, 0.66 or 1.0 kg/s as indicated.
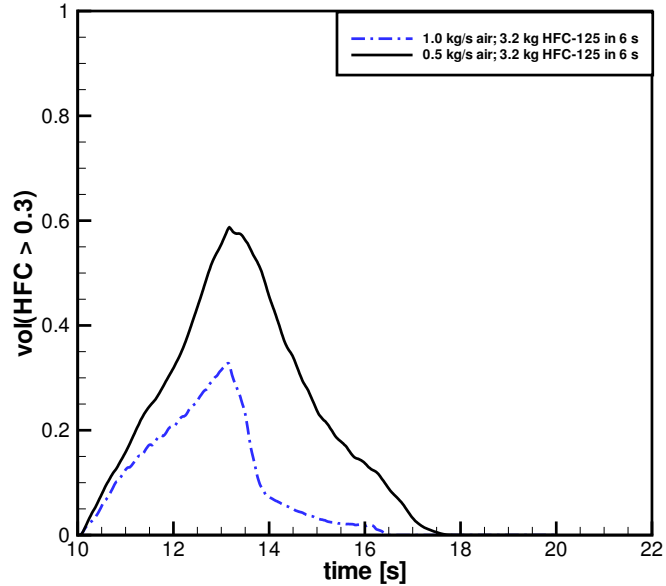
Figure 34: Fraction of the nacelle internal volume for which HFC-125 mass fractions exceeds 0.3 when 3.2 kg of HFC-125 is injected over 6 s. The air flow rate into the nacelle is 0.5 or 1.0 kg/s as indicated.

9   Suppressant distribution without single nozzles

A series of simulations have been conducted to ascertain the effect of removing a single suppressant nozzle while keeping the overall mass of suppressant injected constant. In conducting simulations with specific nozzles removed, the mass flow rate out of the remaining nozzles was kept at the values used in other simulations (i.e. those in Figs. 32 to 34). This corresponds to an assumption of choked flow (driving pressure and nozzle area determine flow rate) where the pressure driving the suppressant is not affected by the removal of a nozzle, and that the individual nozzle areas have not been changed. The injection duration is thus increased somewhat to allow the full 3.2 kg of HFC-125 to flow with a somewhat reduced overall flow rate.

The nacelle volume fraction where the suppressant mass fraction exceeds 0.3 is indicated in Figs. 35, 36 and 37 for air flow rates of 1.0, 0.66 and 0.5 kg/s, respectively. In all of these scenarios, it appears that removing nozzle 3 has no detrimental effect since the complete volume is indicated as filled, and the duration for which it is filled is somewhat increased because of the slightly slower rate of injection with only three nozzles employed. Figure 38 shows the distribution of the suppressant mass fraction with nozzle 3 assumed
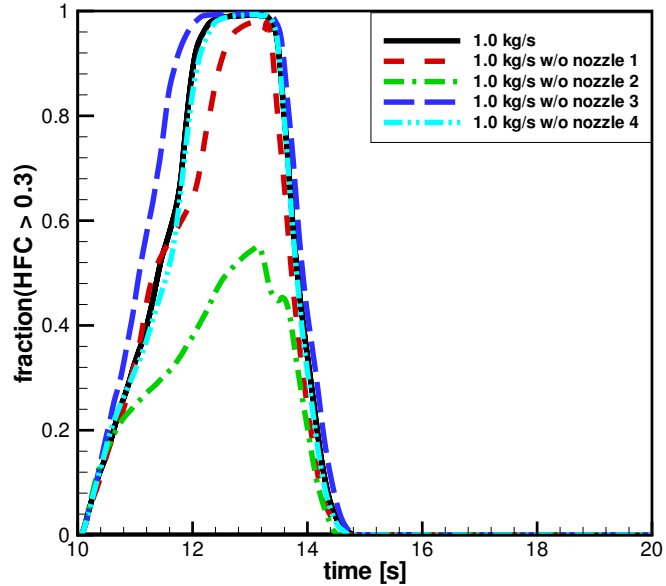
Figure 35: Fraction of the nacelle internal volume for which HFC-125 mass fractions exceeds 0.3 with all nozzles and with indicated nozzles blocked. The mass of HFC-125 injected is 3.2 kg, injected over 3 s. Air flow into the nacelle is 1.0 kg/s and suppressant mass flow through active nozzles is proportional to the measured nozzle-throat area.

to be capped. Nozzle 3 is located on the starboard side of the nacelle, about halfway back, and it discharges into the upper recessed region visible in the centerline plot. The flow from nozzle 3 serves the purpose of filling the recessed area above the engine. However, it appears that this area would be filled even in the absence of nozzle 3 with flow convected upwards around the engine from nozzle 2 visible in on the port and starboard side in Fig. 38. Also, the suppressant from nozzle 3 flowing out of the upper recessed areas is convected into two regions where suppressant is provided for by other nozzles. Suppressant convected towards the forward portions fills a volume that is also filled by nozzle 1. Suppressant transported aft towards the port side fills a region that is also filled by nozzle 4. It appears that the coverage provided by the other nozzles is sufficient. This assumption will be revisited in the later-described fire suppression simulations.

Based on the criteria shown in Figs. 35 through 37, removing nozzle 4 also has little apparent effect on the sufficient distribution of the suppressant. The distribution of the suppressant mass fraction with nozzle 4 assumed to be capped is shown in Fig. 39. Nozzle 4 is located in the aft section of the nacelle, on the port side directed downwards just behind the sixth and last rib. In the absence of nozzle 4, the aft section of the nacelle fills with suppressant more slowly because it relies on the general aft-ward flow to convect
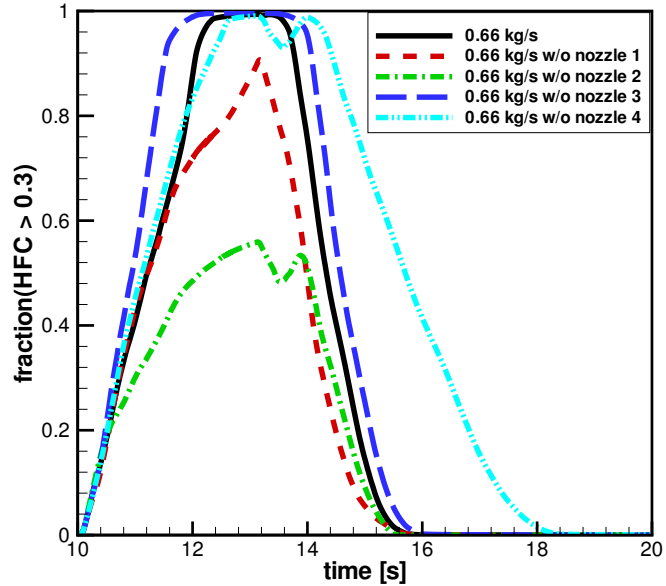
Figure 36: Fraction of the nacelle internal volume for which HFC-125 mass fractions exceeds 0.3 with all nozzles and with indicated nozzles blocked. The mass of HFC-125 injected is 3.2 kg, injected over 3 s. Air flow into the nacelle is 0.66 kg/s and suppressant mass flow through active nozzles is proportional to the measured nozzle-throat area.

suppressant from other nozzles. The mass fraction contour plots indicate that, except for a small region at the very aft of the nacelle where the afterburner control vanes would be, the suppressant is well distributed even in the absence of nozzle 4. We note that the lower diamond vent in the nacelle simulator is modeled here as essentially blocked based on observations of the test simulator; assuming that this vent is not blocked on fleet aircraft, the removal of suppressant in the aft region may be substantially faster making the retention of nozzle 4 highly desirable. Also, the additional vent in the aft region would mean that an even more substantial portion of the suppressant injected through nozzle 4 would rapidly leave the nacelle. Additional simulations to consider the effect of an open diamond vent could help to address this question.

The removal of nozzle 1 or, in particular, nozzle 2 appears to have a significant effect on the distribution of suppressant throughout the nacelle. Based on the criteria shown in Figs. 35 through 37, removing nozzle 1 can leave 10-20% of the nacelle with insufficient suppressant converage while removing nozzle 2 can leave as much as half of the nacelle with insufficient coverage.

The distribution of suppressant mass fraction in the nacelle with nozzle 1 assumed to be capped is shown for vertical planes near the nacelle center and near the starboard and port sides in Figs. 40. As indicated

66
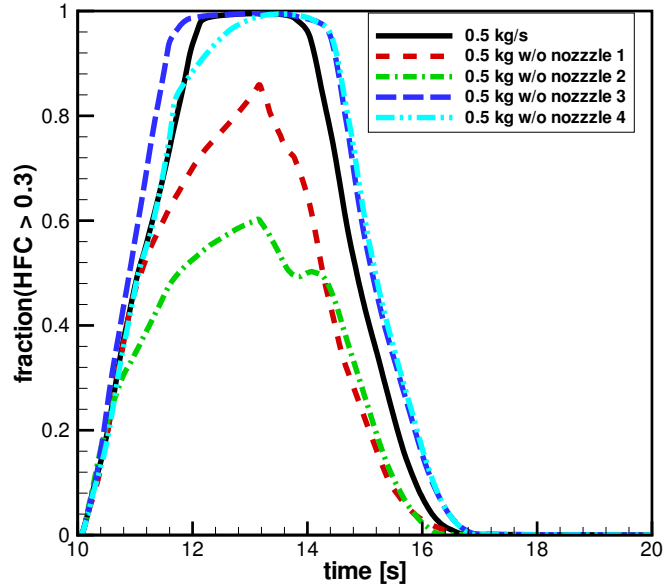
Figure 37: Fraction of the nacelle internal volume for which HFC-125 mass fractions exceeds 0.3 with all nozzles and with indicated nozzles blocked. The mass of HFC-125 injected is 3.2 kg, injected over 3 s. Air flow into the nacelle is 0.5 kg/s and suppressant mass flow through active nozzles is proportional to the measured nozzle-throat area.

earlier, nozzle 1 is located in the forward starboard area of the nacelle and directed upward. The most significant deficiencies in the suppressant distribution with nozzle 1 capped occur on the starboard side, especially in the vicinity of nozzles 1 and 2. The mass fraction in the lower nacelle, both forward and aft of the inlet jet, is also reduced; this is most critical in the region aft of the inlet jet where the mass fractions were closer to the critical levels for suppression. These lower mass fractions arise because less suppressant from nozzle 1 is present in the forward areas to be entrained by the inlet jet.

It is noteworthy that the volume fraction over which the suppressant mass fraction exceeds 0.3 with nozzle 1 capped is less when the air flow rate is less (c.f. Figs. 35 through 37). That is, the coverage is less sufficient when the air flow rate is less. If one considers the analysis in Sec. 3, this results is counterintuitive. In Sec. 3 it was shown that the *average* suppressant mass fraction is greater when the air flow rate is less. This is true here, where the nacelle-averaged suppressant mass fraction (not shown) is increasing as the air flow rate is reduced while the volume fraction covered is decreasing. This indicates that there are more substantial inhomogeneities at lower air flow rates, which is something that the global analysis of Sec. 3 cannot identify. Only a series of measurements or a CFD analysis can identify this phenomena. The reason
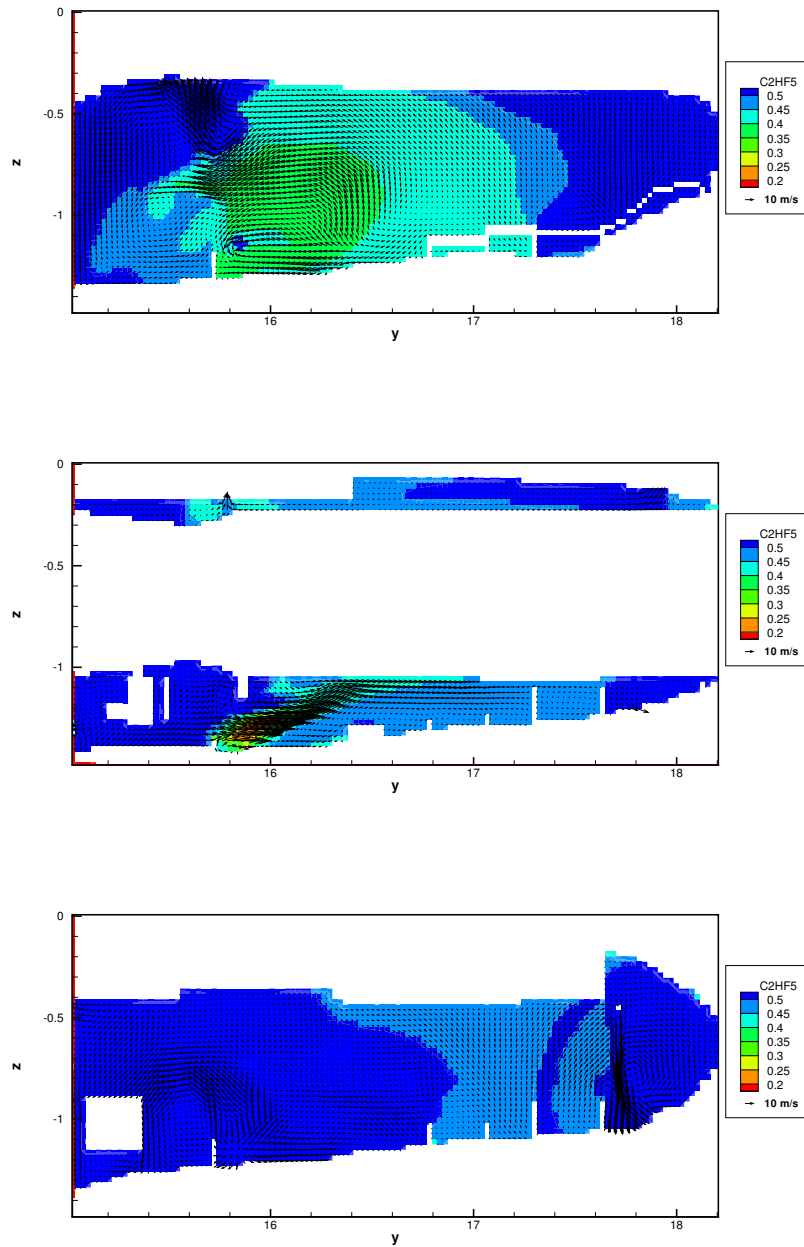
Figure 38: Contour plots of C_2HF_5 at 3.0 s after start of suppressant injection on the starboard side (top), near the nacelle centerline and on the port side (bottom). Nozzle 3 has been capped and suppressant flows through nozzles 1, 2 and 4 only. Air flow into the nacelle is 0.66 kg/s.
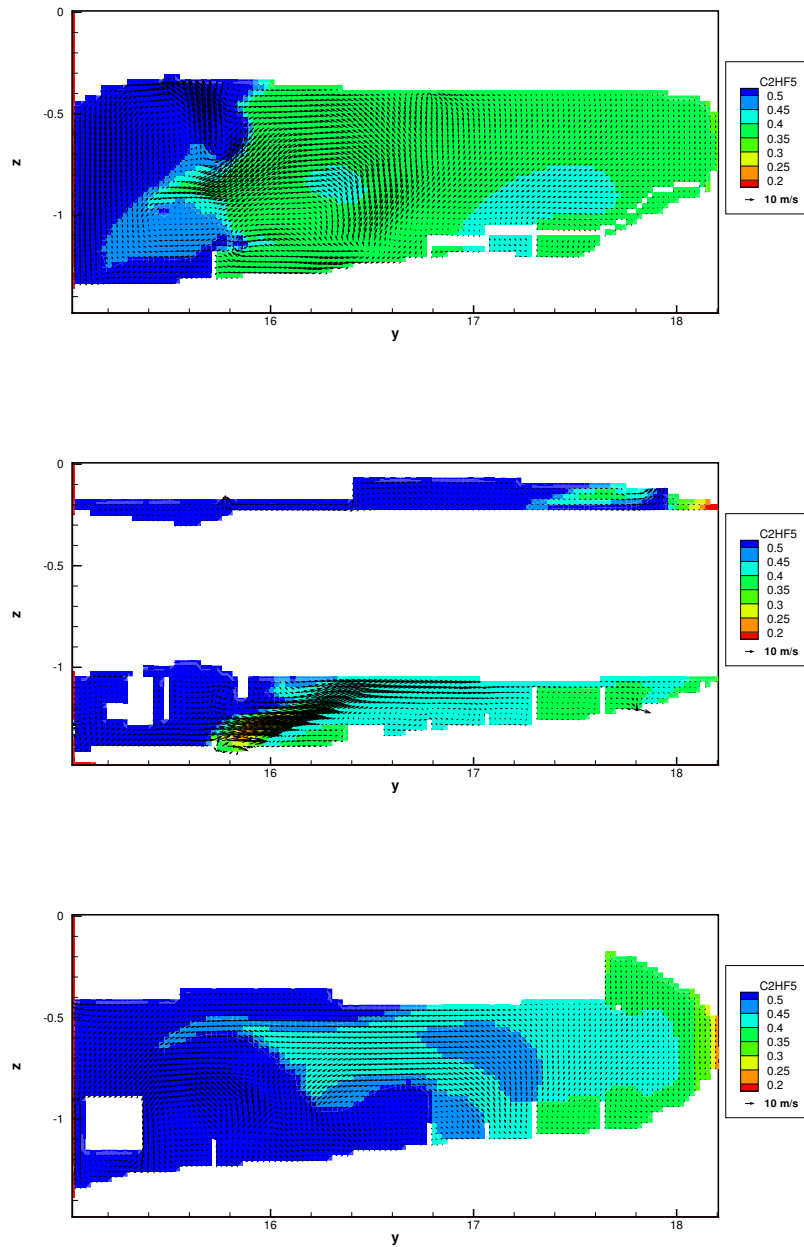
Figure 39: Contour plots of C_2HF_5 at 3.0 s after start of suppressant injection on the starboard side (top), near the nacelle centerline and on the port side (bottom). Nozzle 4 has been capped and suppressant flows through nozzles 1, 2 and 3 only. Air flow into the nacelle is 0.66 kg/s.

for this behavior is related to the initial momentum of the inlet air and the role this plays in the suppressant mixing within the nacelle. The momentum associated with the inlet air flow that drives overall nacelle circulation and the flow past the injection nozzles. This affects the volume of air into which the remaining nozzles are injecting suppressant. Doubling the inlet air velocity moves roughly twice the volume of air past the other nozzles, and thus initially distributes the suppressant over twice the volume of nacelle vapors. The most relevant nozzles here are nozzle 2 and 3, since suppressant from these nozzles circulates into the forward nacelle and does so at a greater rate when the air flow is greater.

The distribution of the suppressant mass fraction is shown in Fig. 41 with nozzle 2 assumed to be capped. Nozzle 2 is located in the forward starboard area of the nacelle and directed across the lower nacelle in the port or outboard direction. Without nozzle 2 present, the inlet jet entrains relatively little suppressant and this results in little suppressant along the lower nacelle where pool fires might exist. The suppressant injected through nozzles 1 and 3 is observed to be largely concentrated in the upper forward nacelle while that injected through nozzle 4 is observed to be primarily restricted to the region aft of the sixth rib. It is only after the suppressant injection is complete that the agent becomes well distributed, and the mass fractions in the lower nacelle at these times are low enough, due to continuous ventilation, that suppression is questionable or doubtful. It is clear that nozzle 2 plays a key role in distributing the suppressant throughout the nacelle through its interaction with the air inlet. The fact that the flow rates in front of nozzle 2, which feeds directly into the inlet air, are so great leads to the great importance of this nozzle in creating a sufficient suppressant distribution.

To summarize, the sufficiency of the suppressant distribution depends on the locations of the nozzles relative to the air flow, the rate of air flow past the nozzles and the rate of turbulent mixing. The nozzle of greatest significance for providing a uniform distribution is the one that feeds into the highest velocity air flows (nozzle 2 here) since this suppressant is distributed most uniformly by the air flow. Nozzle 1 is also significant in this respect since it fills the forward region where the air inlet entrains additional vapors. The kinetic energy of the flow is important for mixing the suppressant, and reducing the kinetic energy by reducing the suppressant injection rate (or the air flow rate in other scenarios) tends to increase the inhomogeneities because of reduced mixing rates. The momentum associated with the initial air flow is also significant since it determines the overall mass of vapors passing the various suppressant nozzles; for this reason, when nozzle 1 was capped the suppressant coverage was increased with greater air flow even while the average mass fraction is decreasing. We note here that later fire-suppression evidence indicates that the Vulcan simulations could be under-predicting the mixing rates to some degree and therefore the actual uniformity of coverage may be somewhat greater than indicated here. The overall conclusions appear to remain valid, despite this minor correction.
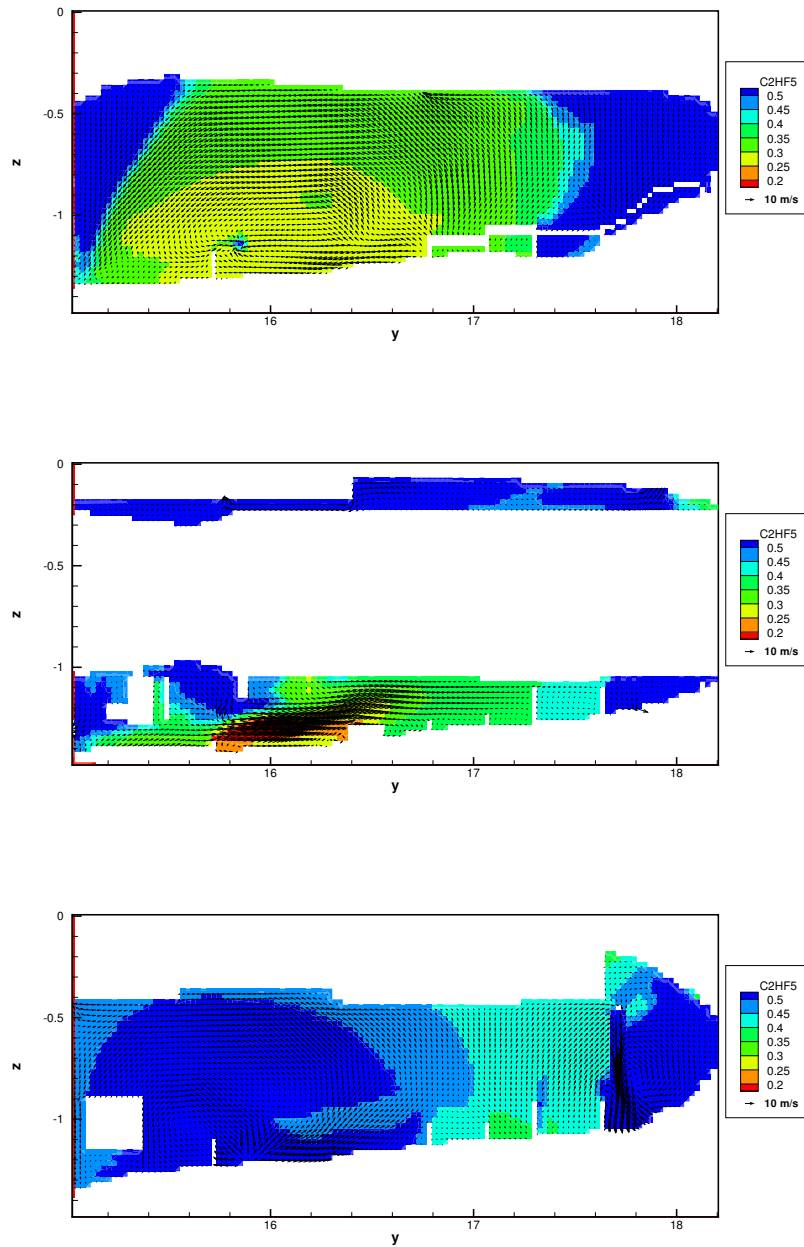
Figure 40: Contour plots of C_2HF_5 at 3.0 s after start of suppressant injection on the starboard side (top), near the nacelle centerline and on the port side (bottom). Nozzle 1 has been capped and suppressant flows through nozzles 2, 3 and 4 only. Air flow into the nacelle is 0.66 kg/s.
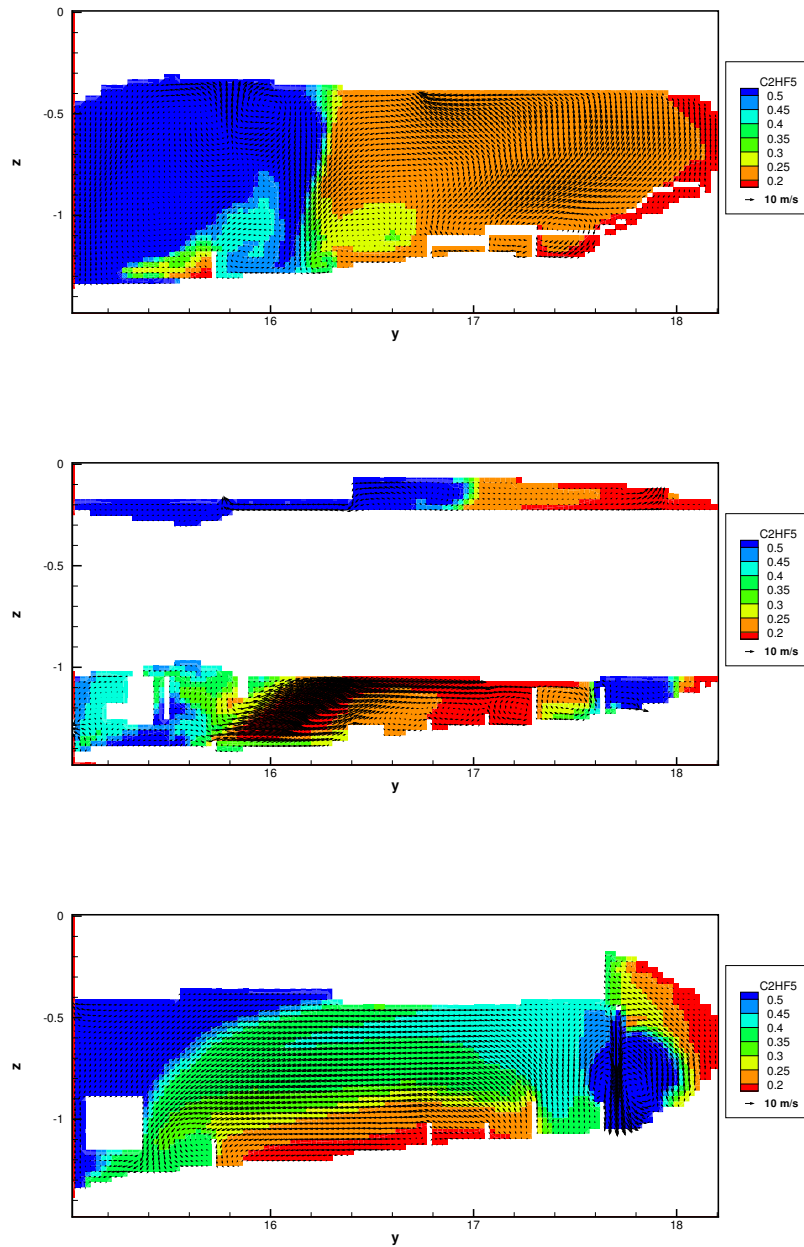
Figure 41: Contour plots of C_2HF_5 at 3.0 s after start of suppressant injection on the starboard side (top), near the nacelle centerline and on the port side (bottom). Nozzle 2 has been capped and suppressant flows through nozzles 1, 3 and 4 only. Air flow into the nacelle is 0.66 kg/s.

Part II

Fire suppression predictions

The following sections address predictions of fire suppression in the nacelle simulator. Following the predictions described in this section, a series of fire-suppression tests were conducted at Patuxent River Naval Air Station. The results of these tests are compared with the Vulcan predictions throughout these sections. It is noted that the test facility capabilities and required procedures prevented a direct match with the simulated conditions, so that most comparisons are subject to some additional uncertainty associated with known differences in the test conditions. These differences are identified throughout this section.

10   Pool fires in the nacelle

Pool fires stabilized behind obstructions have been identified as among the most challenging fires to suppress [14–16]. Obstructions such as structural ribs provide a region of recirculating flow where hot products help stabilize the flame that suppressant is relatively slow to penetrate. In certain scenarios, such as those described in [9,13,28], the suppressant concentration must be maintained at an elevated level in the flow past the stabilization region for a substantial period of time to ensure that suppressant penetrates the stabilization region. In the current simulator the mixing times in the flame stabilization regions are estimated to be short compared to the suppressant injection times (see Sec. 12), but the stabilization region is still important in stabilizing the fire.

10.1   Vulcan pool-fire simulation procedures

Because the previous tests with the nacelle simulator [25] focused on spray fires and because obstruction-stabilized pool fires are known to be challenging to suppress, the present study focuses on pool fire suppression. We consider pools located in four sections of the nacelle as indicated in the schematic in Fig. 42. These sections are delineated from the forward to the aft end with increasing numbers as each rib is passed. The letter 'B' is applied as a prefix to the pool location to indicate that the pool is located between the two central longerons. These are the only locations where substantial quantities of fuel can collect. To augment the quantity of fuel, the basin just to the port of that indicated by 'B' is sometimes assumed to hold some fuel also; this basin is denoted with the prefix 'C.' The pool located at B1 is between the forward end of the nacelle and before the first rib. That denoted B2 is located just aft of the first rib; the inlet air flows partially over this pool. The pool denoted B3 is located behind the second rib. The pool denoted B5C5 is located between the fourth and fifth ribs; these are the two larger ribs. The simulations indicated that pool fires at locations that would be denoted B4 and B6 are more sensitive to heat losses and therefore difficult

to stabilize because of the particular predicted flow circulation. Also, these pools were determined to hold less fuel than the others. Pools B4 and B6 are not considered further here. The approximate surface area of the largest possible pools was measured in the F-18 simulator. Similar pool areas have been used in the simulations; the pool areas are indicated in Table III. The pools are assumed to be filled with two liters of JP-8 and the net evaporation rate based on heat feedback to the pool is also indicated in Table III. The JP-8 is modeled as a single component liquid with a boiling temperature of 423 K, a enthalpy of vaporization of 280 kJ/kg, an enthalpy of combustion of 43.2 MJ/kg, a heat capacity of 2.47 kJ/kg/K and a density of 808 kg/m^3. The pool is assumed to start at a temperature of 293 K and evaporation occurs in the simulations as a consequence of thermal feedback from the fire to the pools. The heat flux to the pools is partitioned between pool heating and evaporation. Initially roughly 70% of the heat flux goes to pool heating and 30% of the heat flux going to pool evaporation for the current simulations, but by the time the suppression occurs the pools have heated substantially towards the boiling temperature. These pool evaporation and heating rates presume that the pool is not losing heat through conduction to the nacelle wall during the course of the fire; as is noted later, it is possible to include heat loss if warranted. In general, it is difficult to accurately predict the thermal feedback to a pool from a fire. Because these fires are partially blown beyond the pools by the advective flows in the nacelle, it is particularly hard to determine whether the evaporation rates are reasonable without suitable measurements. The evaporation rate is viewed as one of the significant uncertainties in the simulation with uncertainties as high as 50% not being unreasonable.

The simulations are conducted by simulating the ignition of the pools with quiescent flow followed by a six-second ramp up in the air-flow rate to the appropriate flow rate for the test. After this, the simulation was allowed to run for ten seconds to insure steady state had been reached. In Sec. 10.4, it will be shown that the simulated flow reached steady state in roughly two seconds. This procedure was followed because the test procedure was expected to be similar. One of the things that the simulations identified was the difficulty of igniting the pools in the strong air flow that occurred in the nacelle at operating conditions. In the later tests, it was determined that it was impossible to ignite the pool fires except at low air-flow rates, and the test procedure did follow the simulation procedure, although the time to light the pool fires was appreciably longer, and in a few tests the air flow was held at moderate air-flow rates in an attempt to heat up the nacelle, ostensibly making it more difficult to extinguish or easier for relight to occur.

Following approximately ten seconds of steady-state simulation, the suppressant was injected. For the purposes of these simulations, the suppressant, HFC-125 was injected as in its vapor phase. That is, the suppressant was presumed to flash vaporize upon leaving the nozzle at ambient temperatures. At the time of the simulations, data was not available regarding the variation of the mass flow rate during the injection process, and a fixed injection rate over a specified duration was employed as described in Part I. The two parameters that were used to specify the injection rate were the total mass to be injected and the duration over which that mass was to be injected. Over that duration, the mass flow rate of the suppressant was
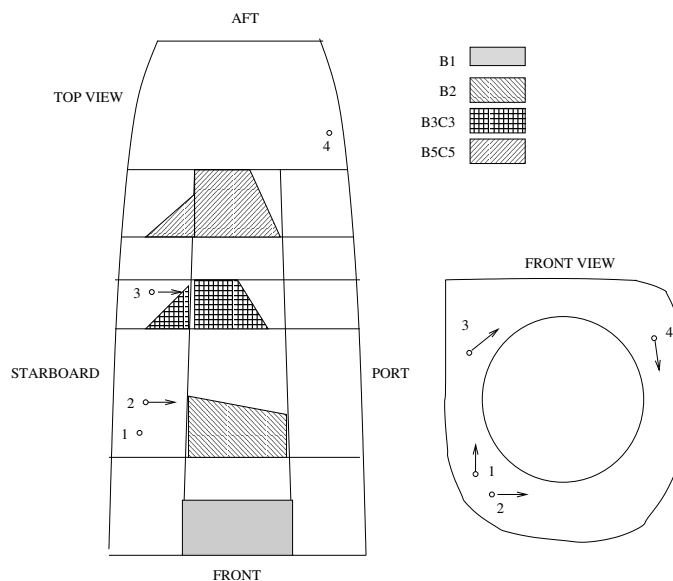
Figure 42: Schematic representation of the relative locations of the pool fires and the suppressant injection nozzles showing the ribs and central longerons. Not to scale.

Table III: Pool characteristics. Here "All" refers to pools B1, B2, B3C3 but not B5C5, the latter being to difficult to reach in the course of the tests.

Pool	Area [kg/s]	Air Flow [m^2]	Pred. Evaporation rate [kg/s]	Volume of combustion	Volume where T > 700 K
B1	0.084	1.0	0.0089	5.9%	4.6%
B2	0.100	1.0	0.011	4.6%	22%
B3C3	0.094	1.0	0.0082	5.5%	37%
B5C5	0.043	1.0	0.0043	1.5%	5.2%
All	0.321	1.0	0.057	16.6%	98.4%
All	0.321	0.5	0.050	7.6%	94.5%

fixed except for 0.1 s ramp-up and ramp-down periods at the start and end of the injection. It is now known that the injection rate over the first half second is probably substantially larger than the fixed rate, while the injection rate tapers off after around two seconds (see Sec. 10.2).

10.2 Nacelle test pool-fire procedures

The basic test procedure followed involved (1) the filling of the suppressant bottle with the desired mass of suppressant, (2) the capping of any suppressant nozzles that were to be turned off for a particular test,

(3) the installation of the suppressant bottle on the test fixture, (4) the filling of the each pool (Table III) with 2 l of JP-8 fuel, (5) the establishment of a minimum air flow and the ignition of each pool fire, (6) a stabilization period where the pool fires became fully engulfed, (7) a gradual increase of the inlet air-flow rate to its target value, (8) another stabilization period at the target air-flow rate and (9) the discharge of the suppressant. Following suppression a reduced air flow was maintained to cool the nacelle and remove potentially flammable vapors, and then the remaining fuel was collected and measured in the graduated cylinders. For fires that were not successfully suppressed, the air flow was reduced and a flight-line fire extinguisher was employed to suppress the fire. Air-flow rates were measured using a 6 inch turbine meter. Details regarding the measurement equipment employed as well as uncertainties are available in [20].

Igniting the pools of JP-8 fuel at ambient temperatures is not trivial. The bottom of the nacelle was warmed with hot air to enhance the volatility of the fuel and to reduce heat losses. A minimum air flow from the blower was established to provide sufficient air for combustion. An electric igniter was inserted over each pool in turn while a more volatile fuel, pure ethyl alcohol, was sprayed onto the pool. Once the pool ignited, it required about 30 seconds to become vigorously inflamed. After all pools had established a durable flame, the air flow was ramped up to the predetermined rate–either 1 kg/s or 0.5 kg/s–as measured with a turbine meter. This steady flow was maintained for about 15 to 30 seconds before the agent was released. The elapsed period of burning was recorded with stopwatches as well as the digital data acquisition system. Four video cameras recorded the views inside and outside the nacelle by which elapsed times for extinguishment were recorded. This data acquisition system also recorded the signals from an array of 21 thermocouples in the nacelle. The temporal response of these thermocouples was not sufficient to determine the temperatures in the interior of the nacelle; the indicated temperatures had not attained steady state over the duration of the fires (see Sec. 10.4).

10.3   Pool evaporation rate results

Evaporation rates in the tests are estimated and these can be compared with those predicted in the Vulcan simulations. The evaporation rates in the tests are estimated by measuring the difference between the volume of fuel put into the nacelle and the volume of fuel drained after each test. The volume difference is divided by the fuel density, estimated at 808 kg/m^3, and the estimated duration of the burn. Unfortunately, it is difficult to assign a duration to the burn since the pools were ignited in sequence and in quiescent air. Once fires were established the air-flow rate was gradually ramped up to the specified flow rate of 0.5 to 1.0 kg/s. As a consequence, it is also difficult to assign an air-flow rate to the duration of the burn, and only peak air-flow rates are used for comparison. The air-flow rates from test data are compared with those from Vulcan predictions in Fig. 43 where it is evident that the measured evaporation rates tend to be lower than those predicted by Vulcan. The tests shown in Fig. 43 correspond to those described in Sec. 14. In light of the
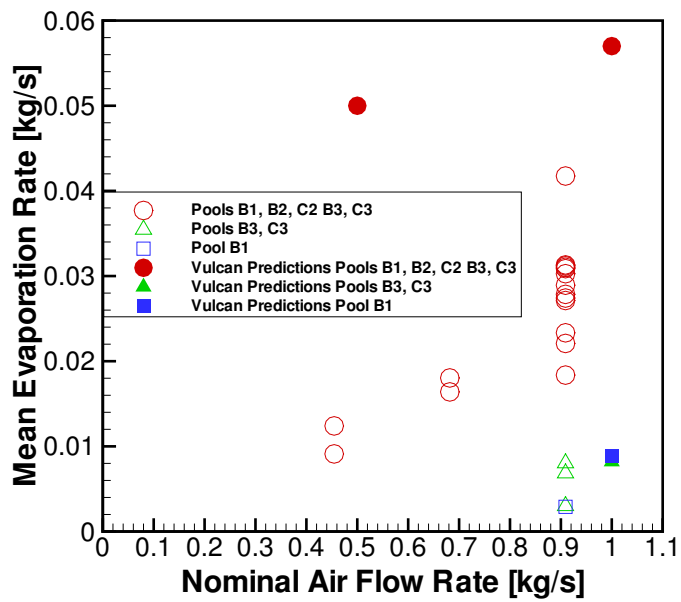
Figure 43: Evaporation rates predicted in the simulations (closed symbols) and measured in the tests (open symbols).

uncertainties in the burn duration and the air-flow rate, it is expected that the indicated measurements from the test data in Fig 43 are lower than the actual evaporation rates during the most intense burning rates at high air-flow rates. It is estimated, based on the time that it took to light the fires and ramp up the air-flow rate, that the actual burning rates are between 30% and 80% higher than indicated. This suggests that the evaporation rates predicted in Vulcan using a simple pool model with are still too high. Since the Vulcan simulations were conducted with no specific heat losses (heat flux to the pool is partitioned between pool heating and evaporation) it is expected that the Vulcan-predicted evaporation rates would represent an upper bound. It is possible to employ a heat loss model in conjunction with the pool model but this was not done because there was not adequate information regarding heat losses when the simulations were conducted (prior to the tests).

10.4   Nacelle temperatures

During the course of the tests, thermocouple measurements were conducted. An array of 21 thermocouples was distributed in the nacelle. The temporal response of these thermocouples was not sufficient to determine the temperatures in the interior of the nacelle, however. The indicated temperatures did not attain steady state over the duration of the fires. Here the predicted temperatures in the nacelle are compared with the thermo-couple measurements. Note that the Vulcan thermocouple model was not employed so that corrections for convection and radiation balances are not incorporated here. Rather this provides a qualitative indication of the temperature field.

As a measure of the degree to which fires in different sections are predicted to spread throughout the nacelle, Figs. 44 and 45 show the volume over which combustion is occurring. For pools denoted B1, B2 and B3C3 combustion (heat release) is occurring in 4 to 6% of the volume as indicated in Table III; for pool B5C5 the volume over which combustion occurs is only about 1.5% of the nacelle internal volume because the fire is contained between the larger structural ribs surrounding this pool. Also indicated in Table III is the nacelle volume fraction over which hot product gases are spread; the criteria for hot product gases is that the control volume averaged temperatures exceed 700 K (427 C or 800 F). Heat release from pool fires B2 and B3C3 is substantially spread throughout the nacelle by the main air inlet that passes over the fires in these regions. Since the pool evaporation rates are likely over-predicted, the volume over which combustion is occurring should be correspondingly over-predicted.

Temperature-time profiles at locations corresponding to several of the Halonizer probes are presented in Fig. 46. These temperature profiles are indicative of the variations in the nacelle during the course of the simulation. A fire is ignited with minimal air flow near $t = 0$ s. While the air flow is minimal there are substantial fluctuations in the temperature since the hot gases are convected in a chaotic manner around the nacelle. As the air-inflow rate increases linearly from $t = 2$ s to $t = 8$ s the fire approaches a more
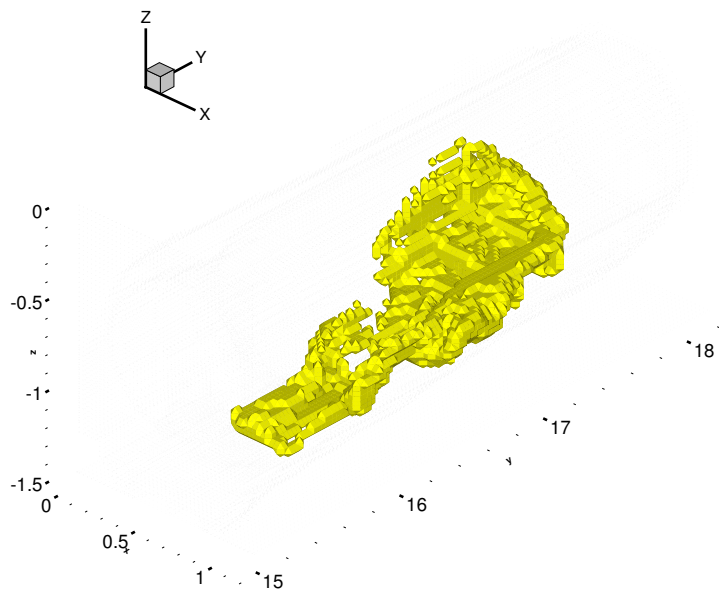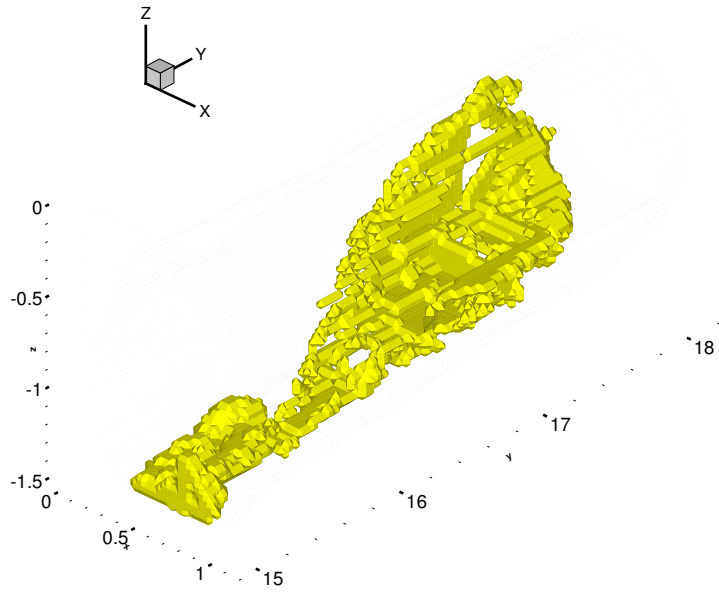
Figure 44: Surface plot showing cells where combustion is taking place for pool fires in locations B1 (top) and B2 (bottom). Surface indicates at least 1 ppm by volume combustion in a computational cell. Air flow into the nacelle is 1.0 kg/s.
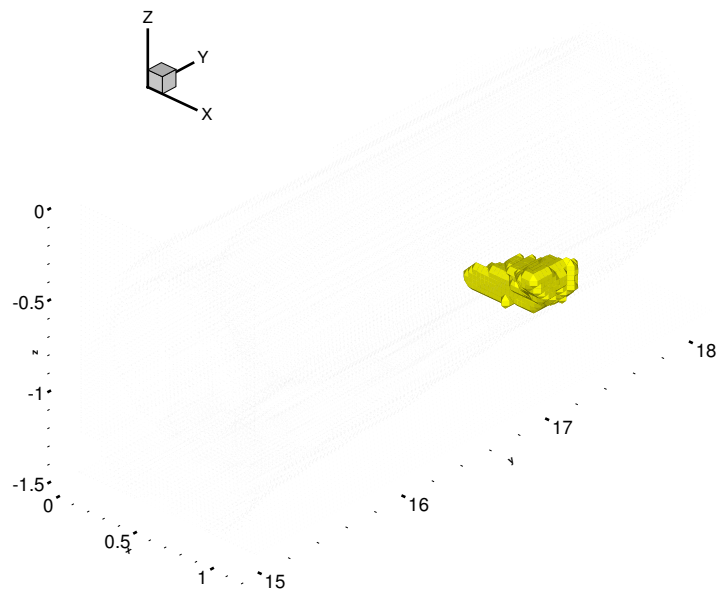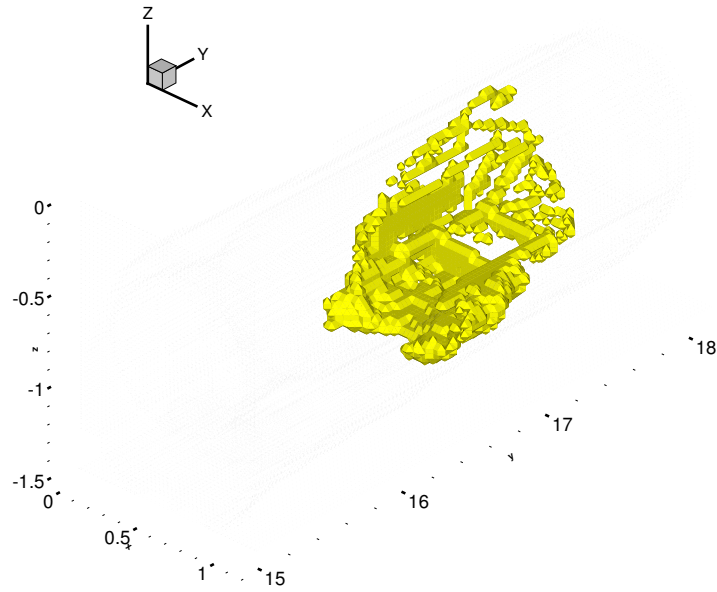
Figure 45: Surface plot showing cells where combustion is taking place for pool fires in locations B3C3 (top) and B5C5 (bottom). Surface indicates at least 1 ppm by volume combustion in a computational cell. Air flow into the nacelle is 1.0 kg/s.
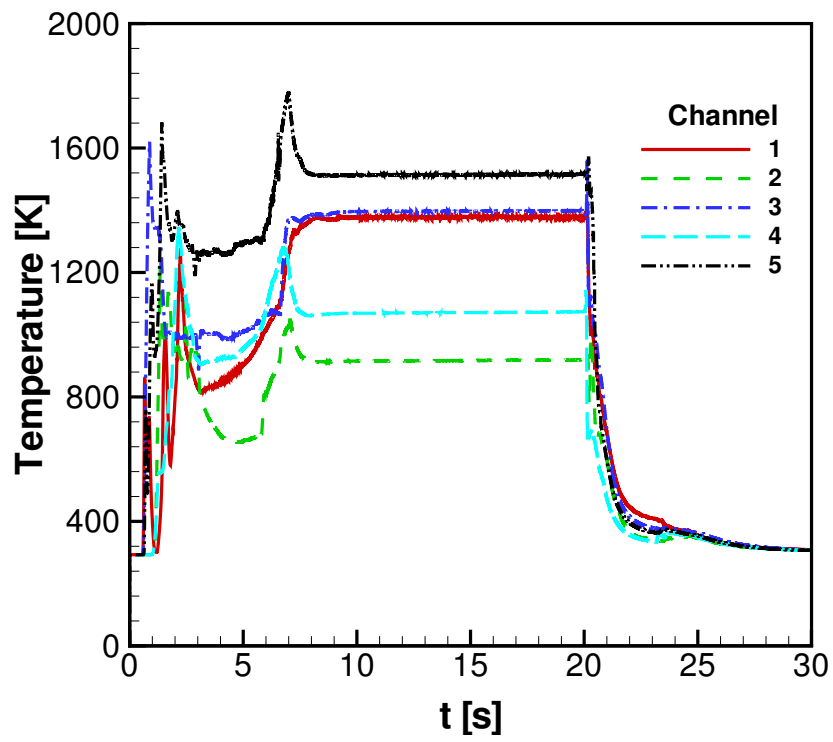
Figure 46: Temperatures at locations in the nacelle corresponding to the locations of channels 1 through 5 of the Halonizer probes are plotted as a function of time for case where air flow is 1 kg/s. All pools are ignited and suppressant injection occurs at 20 s.

determinate state, being driven by the air inflow. The flow field stabilizes before $t = 10$ s and is completely stationary for ten seconds of simulated time. At $t = 20$ s, the suppressant is injected followed quickly by suppression, and the temperature drops rapidly.

The predicted evolution of the temperature can be compared with thermocouple measurements conducted during the course of the tests. An array of twenty-one thermocouples was placed along the lower nacelle in an effort to measure the temperature field and provide an indication of the fire location. The thermocouples were placed in three rows with up to eight thermocouples in a row. The rows extended from the forward to the aft end of the nacelle with thermocouples spaced every eight inches (20 cm). One row was approximately located along the center of the nacelle while the other rows were roughly twelve inches (30 cm) to the inboard and outboard edges of the nacelle. The middle row contained only five thermocouples in order to not interfere directly with the pools. An example of the thermocouple temperature profiles is provided in Figs. 47 and 48 where notable differences with Fig. 46 are evident (note that the test measurements are reported in Fahrenheit in Figs. 47 and 48). Most significant is the fact that the thermocouple time constants are comparable to the duration of the burn, which was generally limited by the time it would take to consume the fuel in pool B2. That is, under the high air-flow rates used in the tests, the fuel evaporation was significant over periods on the order of twenty seconds, which is short compared to the time constant of the shielded thermocouples. In order to avoid uncertainties related to fuel depletion, we were forced to stabilize the flow for only 10-20 seconds at high flow rates before discharging the suppressant bottles. This implies that the thermocouple data does not represent the actual nacelle temperatures. It is noted that the gas temperatures are expected to equilibrate in roughly two seconds, which is the air turnover time scale for the nacelle. The thermocouple data, therefore, is only representative of the combustion temperatures in the nacelle and is not considered accurate because it continues to be influenced by the ambient temperature when the fires were initially ignited. It is also noted that, based on cool-down times, the thermocouple time constants are observed to vary substantially. These differences in the time constant are attributable to the different air-flow rates past the thermocouples; high convection coefficients reduce thermocouple time constants. This suggests that even relative temperatures, between thermocouples in the same test, are not good indicators of even relative temperatures. The test number selected for Fig. 48 was chosen because, for this test, a substantially longer burn duration (on the order of 90 s after the pools were burning at low air-flow rates) was employed before suppression, allowing the thermocouples to rise nearer to their steady-state values. It is clear from Fig. 48 that the thermocouple temperatures are still rising after this long duration burn. The burn time corresponding to the test in Fig. 47 was approximately 15 s so that the thermocouple temperatures can be expected to rise substantially further if a steady state is reached.

Thermocouple measurements conducted along the lower portion of the nacelle during the course of the tests are presented in Figs. 47 and 48. The simulations also predict the full temperature field throughout the nacelle. With the understanding that the higher predicted fuel-vaporization rates lead to higher overall
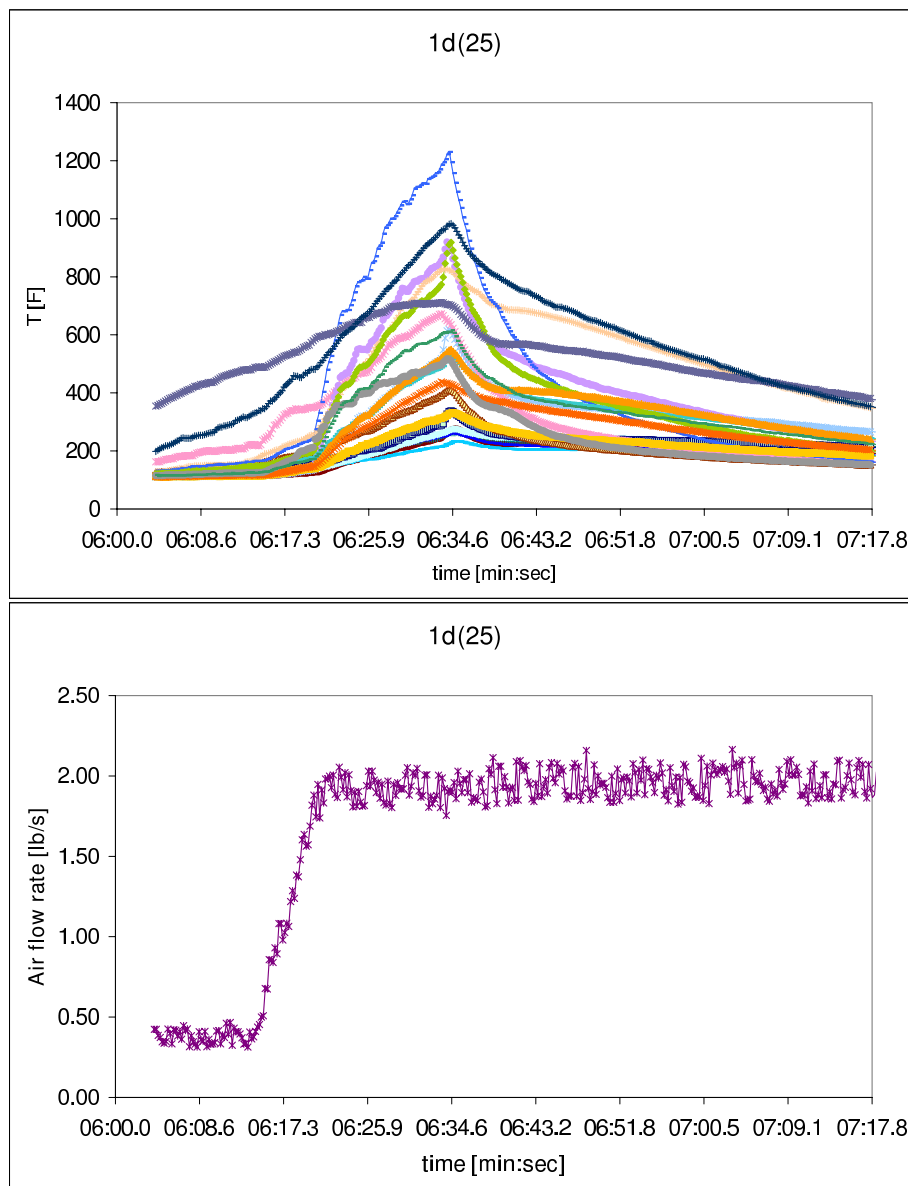
Figure 47: Thermocouple measurements (uncorrected) along the lower nacelle for run 1d(25) are shown in the upper figure as a function of the test time. The air flow is nominally 1 kg/s and the lower figure shows the temporal variation in the measured air mass flow rate (in lb/s). All pools are ignited prior to the start of data acquisition.
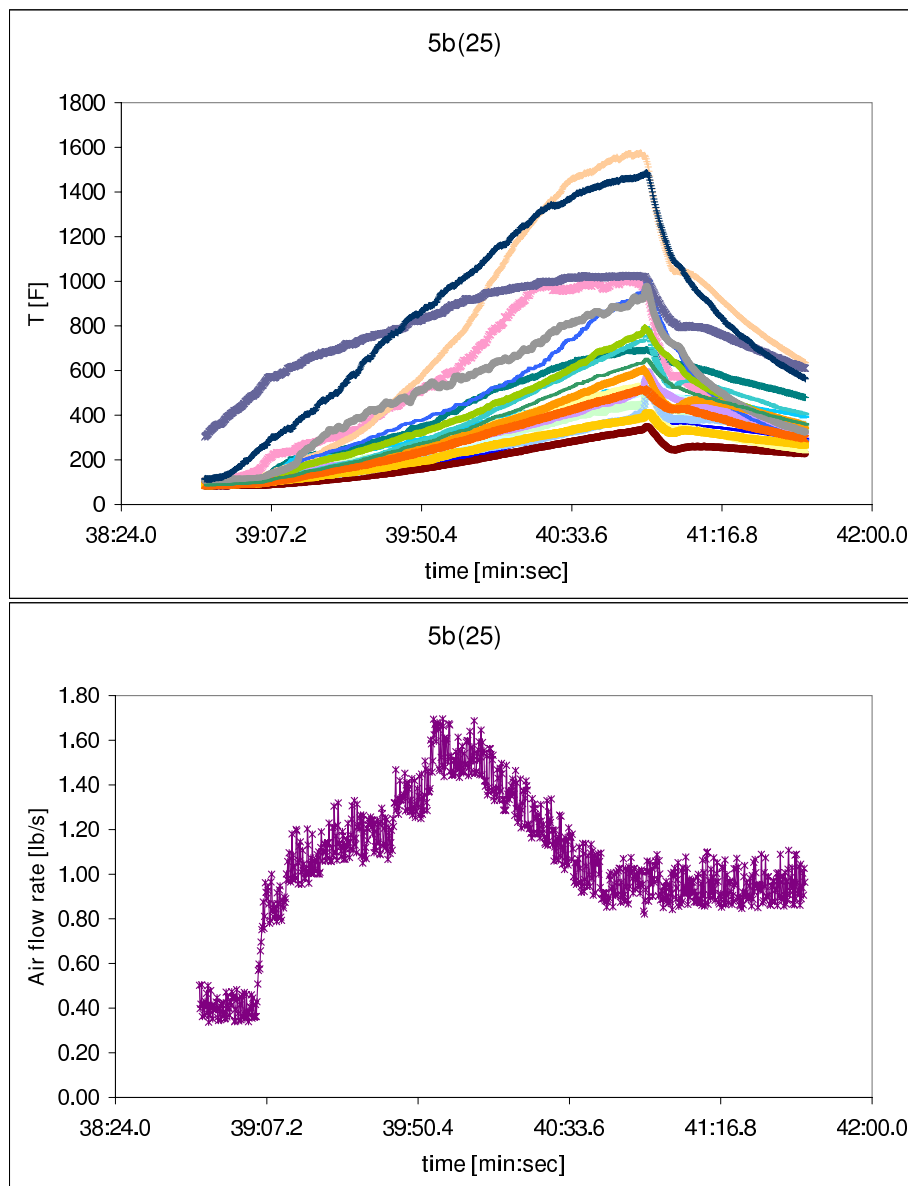
Figure 48: Thermocouple measurements (uncorrected) along the lower nacelle for run 5b(25) are shown in the upper figure as a function of the test time. The air flow is nominally 0.5 kg/s and the lower figure shows the temporal variation in the measured air mass flow rate (in lb/s). All pools are ignited prior to the start of data acquisition.

heat release and correspondingly higher temperatures, Vulcan-predicted temperature contours are provided at roughly the axial locations where temperature measurements along the lower nacelle are also available. These are presented in Figs. 49 through 52 for air-flow rates of 0.5 kg/s on the left pane and 1.0 kg/s on the right pane. In these figures, the peak (not yet steady-state) temperatures taken from Figs. 47 and 48 are imprinted on the contour plots in white lettering. Note that the indicated positions of the temperatures are only approximate and because the temperatures do not reach a steady state the actual gas temperatures are expected to be higher. In general the agreement between the Vulcan-predicted temperatures and the thermocouple measurements is only moderate. The disagreement is attributable to the long thermocouple time constants, differing time constants among different thermocouples, the lower-than-predicted pool burning rates, and the uncertainty in the thermocouple positions. The thermocouple measurements in the forward section of the nacelle are generally the lowest, in agreement with the temperature contours in Fig. 49. However, the thermocouple temperatures rise relatively little compared to the predicted temperatures. It is noted that the higher thermocouple temperatures in the left column are indicative of the longer test run time for the 0.5 kg/s air-flow case (Fig. 48) and these do not necessarily indicate that the temperatures of the low-flow-rate tests are higher. In Fig. 50 the low and high air-flow rate simulations show a different trend regarding the fire around the air inlet: at low flow rates the fire is concentrated around the inflow jet while at high flow rates the inflow velocity is high enough that there is little heat release evident around the jet. In the tests, it was observed that at the highest air-flow rates, the fire over pool B2 was largely blown back towards pool B3. This could be evidence of local extinction just from high rates of mixing, a phenomena referred to as blow out. The thermocouple measurements indicate the highest temperatures in those planes shown in Fig. 51. The thermocouple temperatures in the last two planes indicate cooling that is not evident in Fig. 52; this is likely a consequence of the lower observed evaporation rates in the tests relative to the simulations.

The thermocouple results do corroborate other observations. The thermocouple temperatures are appreciably lower than the Vulcan simulations, even if attempts are made (not presented here) to correct for radiative losses and to predict the steady-state temperatures. The highest five temperatures in Fig. 47 at an air-flow rate of 1 kg/s range from approximately 700 K to 950 K (800 F to 1250 F). The highest six temperatures in Fig. 47 at an air-flow rate of 0.5 kg/s range from approximately 800 K to 1150 K (1000 F to 1600 F). The lower-than-predicted temperatures corroborate the observed reduced fuel-evaporation rates that are measured relative to those predicted by Vulcan. Reduced evaporation rates will lead to less heat release per unit air inflow and lower averaged gas temperatures.

10.5 Suppressant bottle test procedure and discharge rate

The mass of agent to be used in each test was measured by the difference over the tare of the empty bottle on a calibrated scale. HFC-125 (C_2HF_5) was the agent used in all tests. The rate of injection was controlled by the
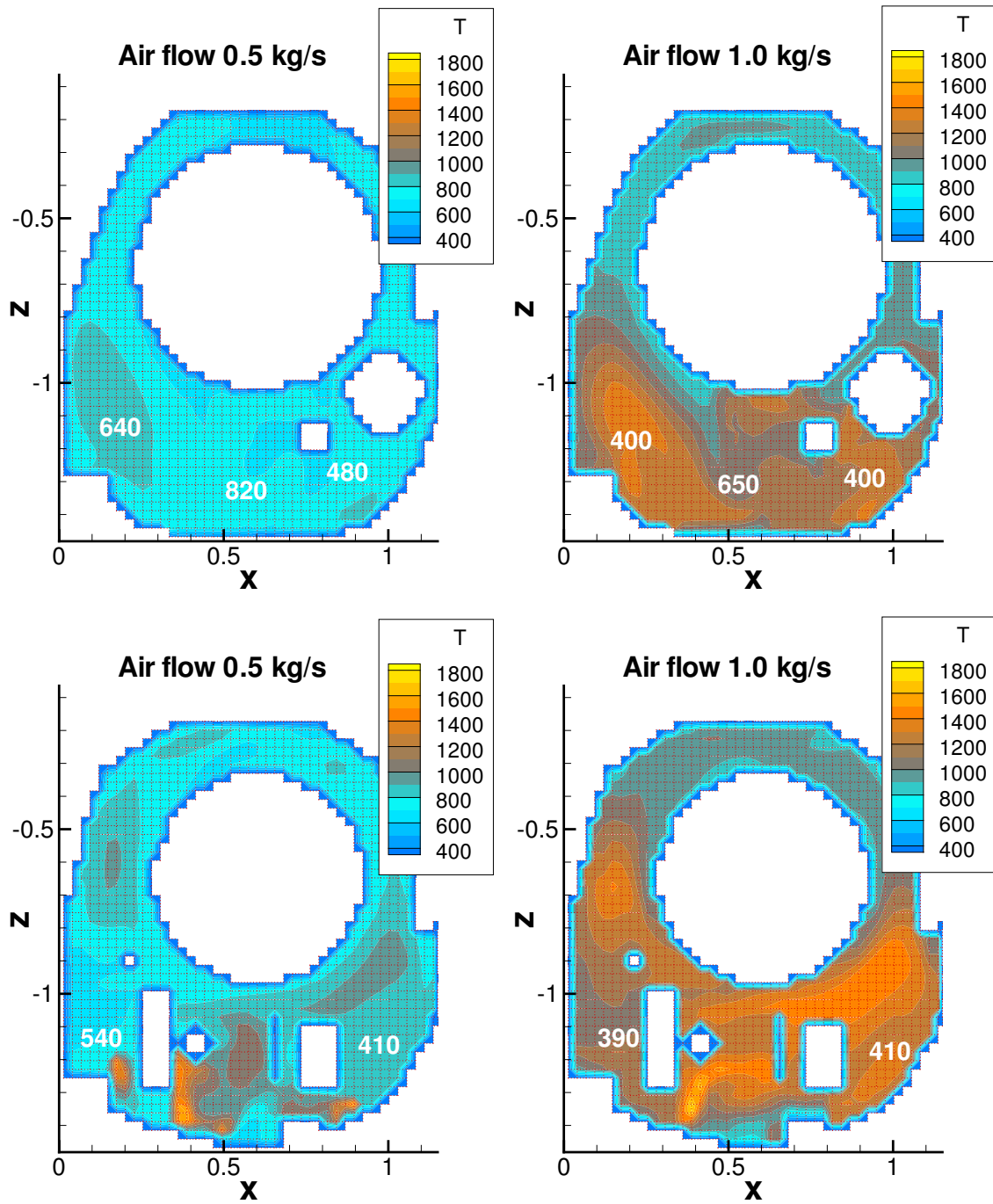
Figure 49: Temperature contours at locations 15.16 m (top) and 15.55 m (bottom). The air flow rate is 0.5 kg/s in the left panes and 1.0 kg/s in the right panes. The peak indicated thermocouple temperature from Figs. 47 and 48 (in degrees K) is shown with white lettering.
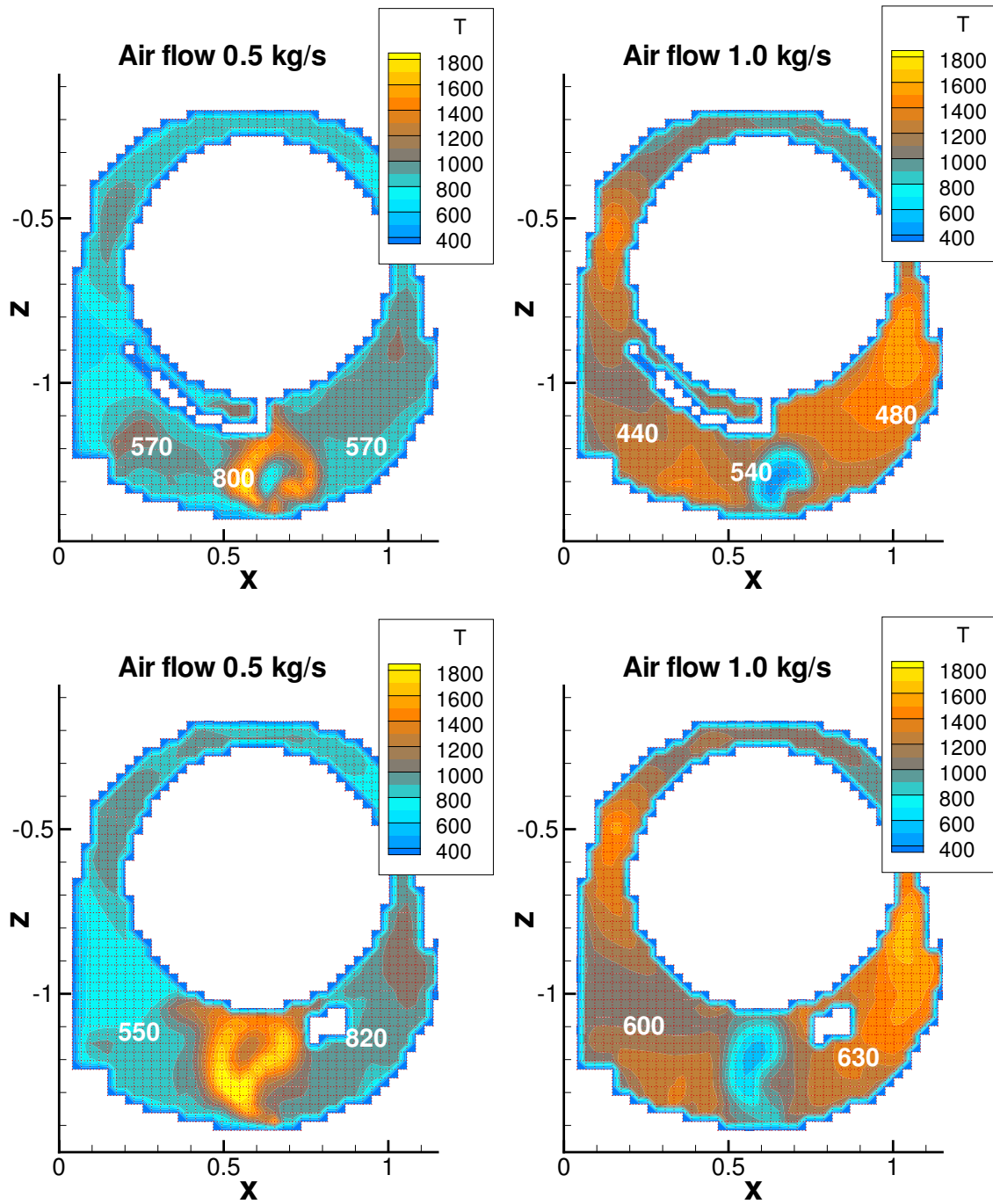
Figure 50: Temperature contours at locations 15.81 m (top) and 16.20 m (bottom). The air flow rate is 0.5 kg/s in the left panes and 1.0 kg/s in the right panes. The peak indicated thermocouple temperature from Figs. 47 and 48 (in degrees K) is shown with white lettering.
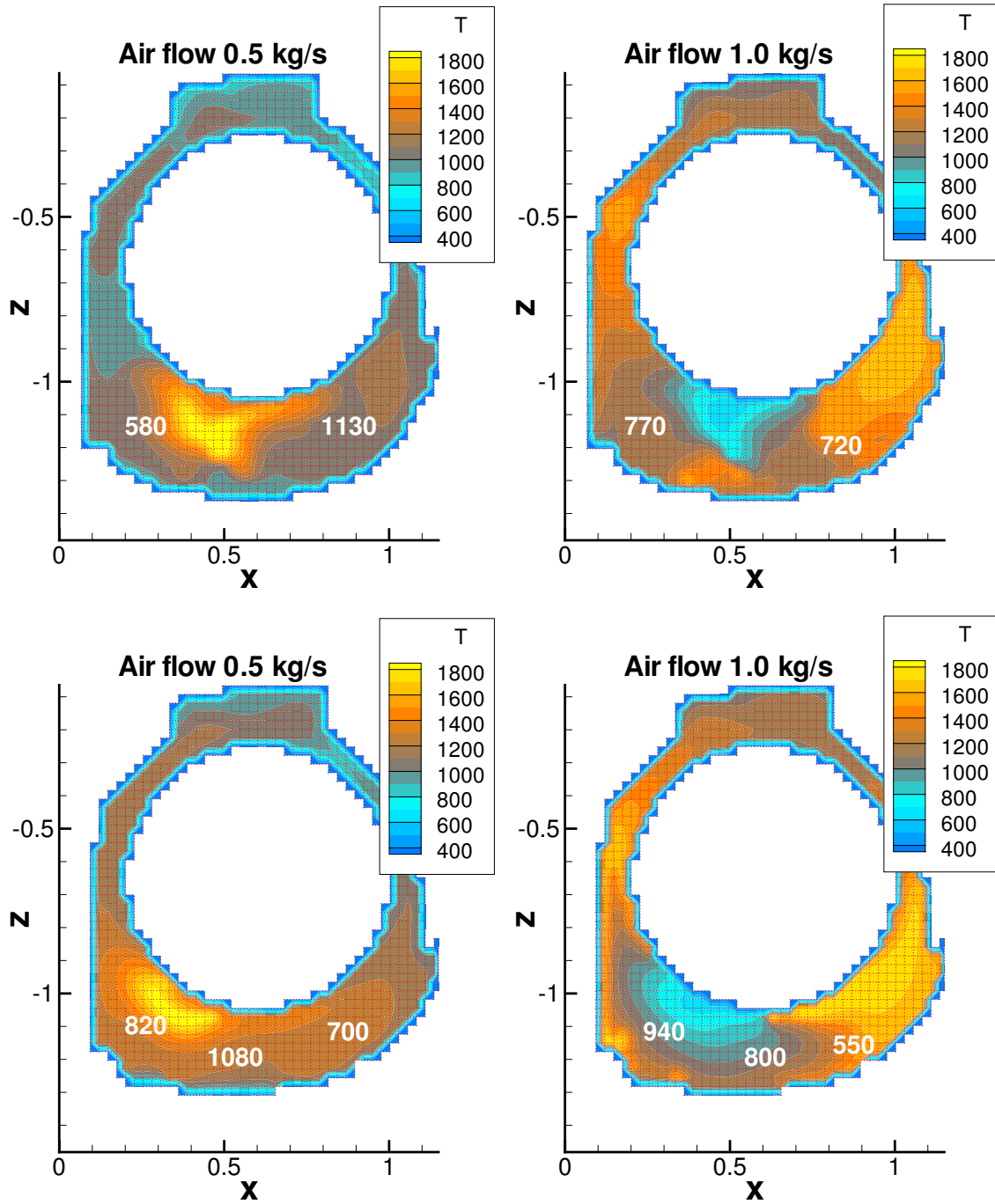
Figure 51: Temperature contours at locations 16.59 m (top) and 17.01 m (bottom). The air flow rate is 0.5 kg/s in the left panes and 1.0 kg/s in the right panes. The peak indicated thermocouple temperature from Figs. 47 and 48 (in degrees K) is shown with white lettering.
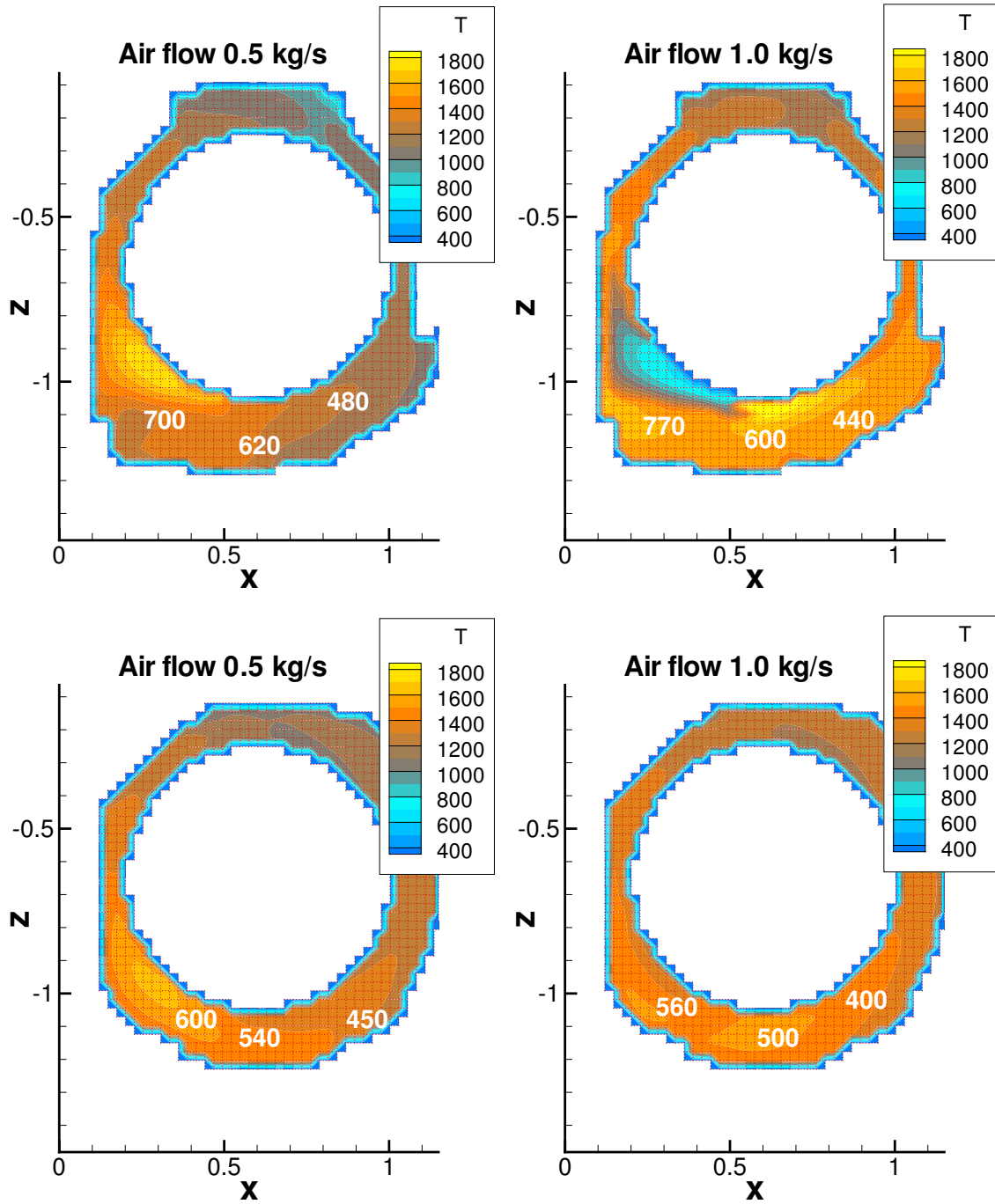
Figure 52: Temperature contours at locations 17.41 m (top) and 17.83 m (bottom). The air flow rate is 0.5 kg/s in the left panes and 1.0 kg/s in the right panes. The peak indicated thermocouple temperature from Figs. 47 and 48 (in degrees K) is shown with white lettering.

nitrogen pressure level in this bottle, and three rates of injection were targeted by setting the bottle pressure to one of three values. These values targeted injection rates that were expected to roughly correspond to a designed system (515 psig, 35.5 bar), a rate roughly 75% of the designed system (275 psig, 19 bar) and a rate roughly 50% of the designed system (122 psig, 8.5 bar); at these ambient temperatures the vapor pressure of HFC-125 was about 122 psig (8.5 bar) so that no nitrogen charge was added for the lowest pressure. Nitrogen is somewhat soluble in this agent, and consequently the fire-suppression agent in these tests was a mixture of both HFC-125 and nitrogen; the latter is ignored in the Vulcan simulations. The pressure measurements suggest a three-stage discharge process. The suppressant bottle discharges downward so that the initial stage of the discharge is driven by the nitrogen pressure, which drops as liquid agent is displaced from the bottle. At an intermediate pressure the rate of pressure change slows; this is associated with agent discharge being driven largely by the boiling of the agent or the dissolved nitrogen. That is, once the bottle pressure approaches the agent vapor pressure, the agent boiling keeps the bottle pressure approximately constant. Note that for the lowest bottle pressure there is no initial nitrogen-driven stage. The last stage of the discharge follows, in which the gaseous agent and nitrogen in the bottle flow from the bottle. The pressure profiles from several tests, where discharge was through all of the nozzles, are shown in Fig. 53. Test labels will be described below in Sec. 14.2 and given in Table VI. The discharges from the two tests denoted 1a(21) and 1a(25) are essentially the same conditions, as are the four tests denoted 1b(21), 5b(25), 8a(26) and 1b(26). The spread in these pressure profiles is indicative of uncertainties attributable to, for example, ambient temperature changes that may heat the bottle during the few minutes that the test is being set up. Such uncertainties are thought to be the most significant and are estimated to affect the discharge rate by roughly $\pm 10\%$. Note that the discharge rate is proportional to the square root of the pressure, to leading order.

Attempts to model this discharge based on the pressure data with simple pipe flow network models have proven challenging, and the results indicate that the flow at the nozzle where most of the pressure drop occurs is most likely multiphase flow. We estimate somewhat more gas than liquid phase (by volume) at the nozzles, with our best estimate being 60% gas and 40% liquid by volume. This volume ratio is expected to vary during the evolution of each discharge, moving towards 100% vapor at the end of the discharge. Note that the majority of the agent mass remains liquid (volume fractions are given in the previous sentence), but the presence of the gas phase dramatically reduces the rate at which the agent flows into the nacelle.

11 Suppression model

The fire suppression model contained within Vulcan [13] is key to its ability to predict the nacelle physics. Because the full range of chemical and fluid dynamic length scales cannot be resolved in engineering-scale turbulent flows, the effects of chemical kinetics are captured within subgrid-scale models. To predict
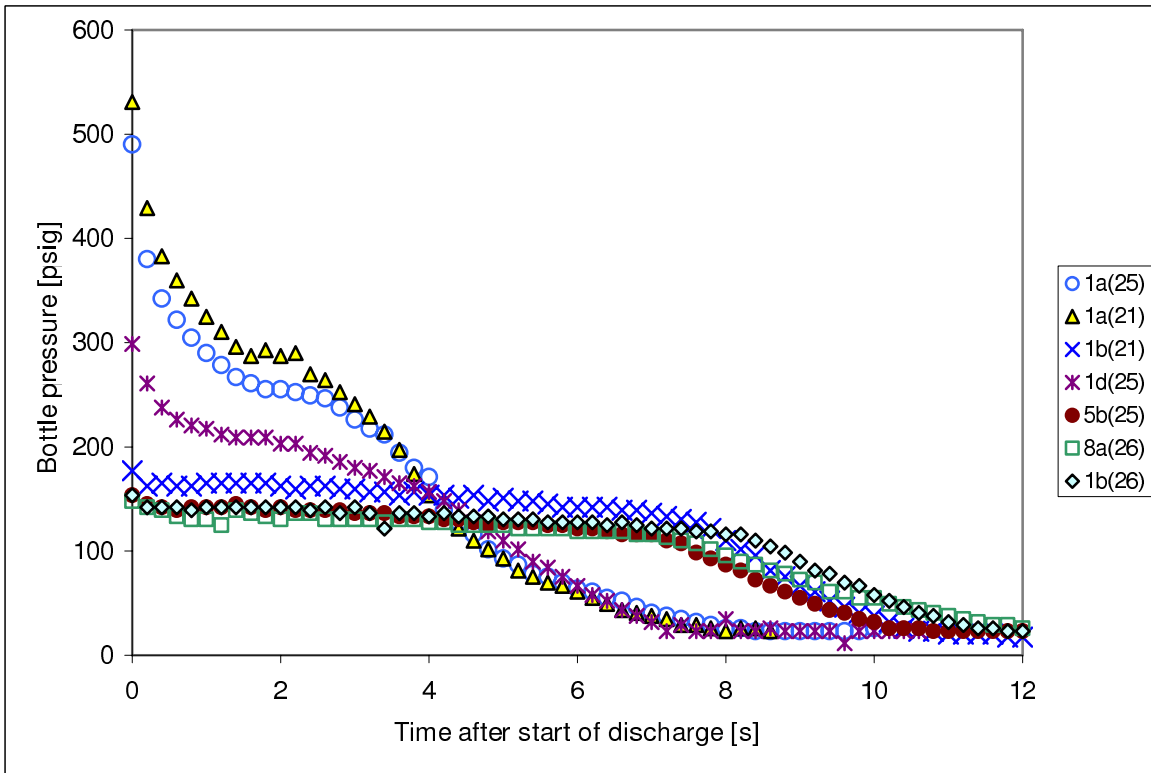
Figure 53: The suppressant discharge pressure, measured at the bottle, for various initial pressures with all nozzles discharging and a total of 3.2 kg of agent. The curves are labeled with the test label to be given below in Table VI.

fire suppression requires a prediction of local flame extinction. An extinction criterion can be expressed in terms of a Damköhler number, $Da = \tau_\eta/\tau_{ext}$, the ratio between fluid mixing and chemical times. A suitable chemical time relevant to flame extinction, τ_{ext}, can be defined as a perfectly stirred reactor (PSR) mixing time corresponding to a switch from combustion occurring to combustion being impossible. In other words, τ_{ext} is the chemical time scale representing the fastest possible chemical-reaction rates. For Damköhler numbers smaller than a critical value, Da_{crit} , the flame will be extinguished, so that for

$$\tau_\eta/\tau_{ext} > Da_{crit} \tag{10}$$

combustion may occur, while for

$$\tau_\eta/\tau_{ext} < Da_{crit} \tag{11}$$

combustion may not occur. Combustion in Vulcan is modeled using the EDC model that can be thought of as a distribution of PSR's that relate the fuel-consumption rate to the fluid-mixing rate, the latter obtained from turbulent time scales. The submodels within Vulcan assume that the fuel-air mixing rates scale with the inverse of the Kolmogorov time scale, τ_η,

$$\tau_\eta = 0.41(\nu/\epsilon)^{1/2} \tag{12}$$

where ν is the molecular viscosity and ϵ is the turbulent kinetic-energy dissipation rate. The actual mass rate of reactant mixing is proportional to τ_η and also a function of the local reactant mass fractions. It is noteworthy that in high-fidelity modeling of turbulent diffusion flames, the fluid time scales corresponding to extinction are found to be very close to the Kolmogorov time scale [12]. For mixing rates that exceed a critical value, the chemical kinetics and the associated heat release cannot keep up with the rate of reactant influx and the rate of product out flux. In this case, the flame will be extinguished. This critical mixing rate is true of both PSR's and turbulent flows, but as indicated below, τ_η is not exactly the same as the critical mixing rate in PSR's.

The chemical time scale corresponding to extinction, τ_{ext}, is a function of the reactant composition and enthalpy. This time scale is essentially the inverse of the maximum possible rate of reaction within the flame. Fire suppressants typically increase the chemical time scale by slowing down the overall chemical kinetics in at least one of the following manners: (1) dilution reduces the frequency of collisions between reactive molecules, (2) chemical inhibition causes a reduction in the levels of active radicals through an enhancement of chain-termination reactions and (3) cooling of the flame reduces the overall kinetic rates through a reduced probability of a molecular collision crossing an energetic barrier. The chemical time scale is obtained through detailed chemical-kinetic calculations using the hydrocarbon mechanisms from [3] and suppressant mechanisms from [1, 21]. Using these chemical-kinetic mechanisms in the Chemkin PSR
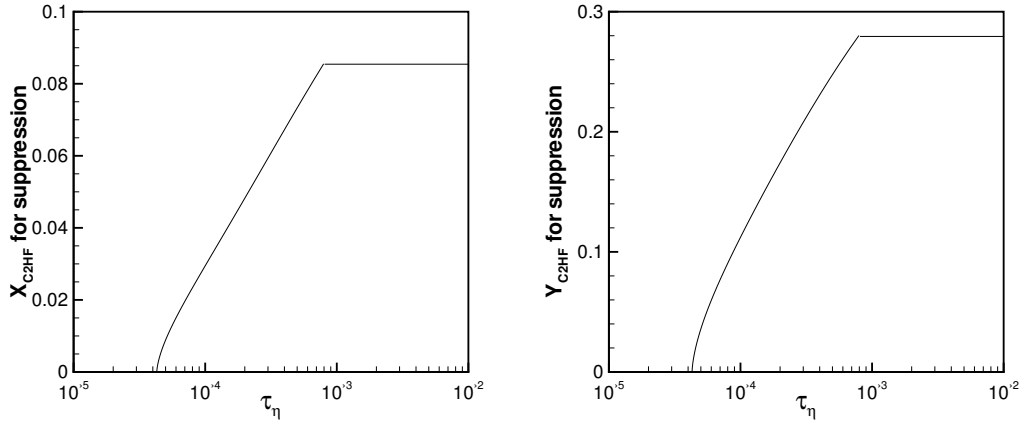
Figure 54: Suppressant mole (left) and mass (right) fractions required to extinguish flames for a given turbulent mixing time scale.

code [26], τ_{ext} was determined for PSR's with varying levels of suppressant mass fraction and varying degrees of cooling.

The critical Damköhler number that determines the ratio between τ_η and τ_{ext} at flame extinction is not known a priori because the PSR mixing rate is not identical to the turbulent mixing rates, but is related by an order-unity constant. The critical Damköhler number is determined empirically by matching blow-off criteria for an ethane jet flame as described in [30]. Because this test involves no suppressant, this measure is independent of knowledge of the suppressant chemistry. A value of $Da_{crit} = 0.563$ is obtained in this manner indicating that the PSR and turbulent mixing rates are indeed of the same order. Combining this extinction criteria with the various chemical times leading to PSR extinction, as described in the previous paragraph, yields an extinction criteria with fire suppressants. For HFC-125 employed here, the extinction criteria are plotted in terms of the suppressant required for a given fluid mixing rate, τ_η, in Fig. 54. It is seen that as the suppressant mass fraction increases, the mixing time required for complete combustion, and thus flame stabilization, increases. This corresponds to the reduction in the chemical rates associated with the introduction of suppressants as described in the previous paragraphs. It is presumed that there is a maximum mixing time in relevant systems that arises because of the expected range of physical scales and the buoyancy generated mixing rates. This time scale is 0.6 ms, and this leads to the maximum required suppressant mass fraction of 0.28 evident in Fig. 54. Such a limit is in agreement with cup-burner test results [9].

12 Mixing times for clutter

There are two key challenges in suppressing clutter-stabilized pool fires. First, clutter creates a region in the recirculation zone where fluid-mixing time scales may increase. As indicated in Fig. 54, this leads to an increase in the required suppressant. Second, there is a delay in the mixing of suppressant from the flow past the obstruction into the recirculation zone. This delay can be approximated using a perfectly-stirred reactor mixing model. Under such an assumption, the mean suppressant mass fraction in the flame stabilization zone, Y_{stab}, can be approximated as

$$Y_{stab} = Y_\infty[1 - \exp(-t/\tau_{mix})] \tag{13}$$

where Y_∞ is the mass fraction in the fluid flowing past the recirculation zone and τ_{mix} is the mixing time constant. For simple flow past a single step or rib with no other obstructions, Takahashi et al [29] measured the mixing time constant to be

$$\tau_{mix} = 34.7(h/u^*) \tag{14}$$

where h is the obstruction height and u^* is the average of the mean flow velocity over the step and the mean flow velocity without the step. Based on the CFD simulation predicted velocities, it is possible to estimate mixing times using Eq. 14 although these estimates are complicated by the facts that the velocity varies laterally across the ribs and that the flow is not exactly normal to the ribs. For flow past the first rib, which stabilizes flames in pool B2, the mixing times range from very small where the inlet flow crosses the rib to 0.9 s where velocities are lower. For flow past the second rib, which stabilizes fires in pool B3, mixing times are in the vicinity of 0.1 to 0.2 s; mixing times for the third rib are similar. For flow past the large fourth and fifth ribs, which stabilize fires in pool B5C5, the mixing times range from 0.6 to 1.5 s. Except for the last set of ribs, the mixing times are generally small relative to the residence time for the suppressant in the nacelle so the finite mixing time is not expected to play a significant role.

Hewson et al [13] showed that additional obstructions can affect the mixing time constant. In general, when obstruction wakes are coincident with the stabilization zone, the associated wake low-pressure region tends to pull the flow away from the stabilization zone and increase the time required for suppressant to mix into the flame stabilization zone. If the obstruction is located so that the high-pressure stagnation region in front of the obstruction is coincident with the wake, the opposite behavior is observed, resulting in reduced suppressant mixing times.

Table IV: Fire suppression tests with an air-flow rate of 1.0 kg/s.

Pool	mass HFC-125 [kg]	injection rate [kg/s]	Nozzles	Suppression Time [s]
B1	3.2	1.07	1,2,3,4	0.8
B1	2.2	1.07	1,2,3,4	0.8
B2	3.2	1.07	1,2,3,4	0.9
B2	2.2	1.07	1,2,3,4	0.9
B3C3	3.2	1.07	1,2,3,4	1.2
B3C3	2.2	1.07	1,2,3,4	1.2
B3C3	3.2	0.53	1,2,3,4	none
B3C3	3.2	0.64	1,2,3,4	none
B3C3	3.2	0.71	1,2,3,4	none
B3C3	2.2	0.73	1,2,3,4	none
B5C5	3.2	1.07	1,2,3,4	1.8
B5C5	2.2	1.07	1,2,3,4	1.8

13   Suppression of pool fires: initial predictions

Suppression simulations were conducted in two phases followed by tests conducted on the physical nacelle simulator. The first series of simulations identified some test-design issues that led to a rethinking of the test procedure. Specifically, the challenge of igniting and stabilizing flames in specific areas of the nacelle was identified in the first stage of simulations. Also, the sensitivity of the suppression to pool heat losses was identified. To overcome concerns raised by these simulation results, the test plan was revised and a second set of simulations was carried out to conform to a set of tests that were expected to be easier to conduct and less sensitive to uncontrollable parameters. In this section, the results of the first series of simulations are presented. Results are first presented using the four-nozzle suppression system for various pool fire configurations presented in Sec. 10, and then for a three-nozzle suppression system in which one of the nozzles was capped. In the following section the results of the second series of simulations are presented along with the test results.

13.1   Results with four nozzle system

In general, suppression is predicted for pool fires at all locations in the nacelle using the four-nozzle con-figuration with 3.2 kg of suppressant when this mass is injected in three to four seconds. A three second injection duration (1.07 kg/s of suppressant injection) corresponds to the nominal suppression system design identified in previous testing, so the present results indicate that the production system should be sufficient to suppress pool fires. In previous sections (see Sec. 3 and 8), it was observed that reducing the mass injec-tion rate of the suppressant reduced the average mass fraction in the nacelle, and also resulted in apparently

insufficient coverage to suppress certain fires. To examine the effect of varying the mass of suppressant injected and the rate of suppressant injection, a series of additional simulations for fires in pool B3C3 were conducted. Simulations with other pools were conducted, but other pools proved easier to extinguish, and these are not reported. When the rate of suppressant injection is reduced to just below 0.75 kg/s, no suppression was predicted in the simulations, although the combustion would certainly be described as tenuous for these conditions since the fire was restricted to a corner of the pool C3. As the rate of suppressant injection is reduced, the fire stability increases, and at 0.53 kg/s the fire is evidently stabilized, at least near the corner of pool C3. The fire tends to stabilize in this location because the mixing rates are lower.

It is noteworthy that the mass of suppressant injected plays little role in determining the occurrence of suppression here. For the two cases with suppressant injection rates of 0.71 and 0.73 kg/s, the resulting tenuous combustion region is very similar. There will certainly be a lower bound in terms of suppressant mass injected over a short period of time, although this has not been identified in the simulations. More significant in terms of the mass of suppressant employed is the duration over which suppressant will act to inhibit reignition and allow cooling of heated surfaces. Thus the suppressant requirements are likely to be dictated by two factors. First, to insure suppression by flooding the compartment with a high enough concentration, a sufficiently high rate of injection is required. Second, to maintain that concentration for long enough to prevent reignition a minimum mass is required. Only the former factor is considered here. In general, the suppression effectiveness is found to correlate most strongly with the mass injection rate.

Though the results are not presented here, suppression is sensitive to heat flux from the fire to the pool. If the heat flux and, hence, the fuel evaporation are reduced by 50% by imposing a 50% heat loss on the pools, suppression is substantially easier for the cases considered in this section. Specifically, the reduced suppressant injection rates shown in Table IV that fail to suppress the fire in pool B3C3 succeed in suppressing the fire if the heat flux is reduced by 50%. The reason for this is that the fire can more readily be completely separated from the fuel source with slower evaporation rates. Similar results are expected if the fuel is cold or if there are substantial heat losses through the nacelle under the pool. While relatively high engine temperatures are expected during operations, temperatures during ground tests may be such that reduced evaporation is experienced.

In light of the lower evaporation rates observed in Sec. 10, it is likely that if tests were carried out for some or all of these simulations, then fires might have been extinguished more readily. However, the sensitivity to heat losses that was identified with a single pool fire led to a shift in the test plan towards tests with several pools simultaneously burning.

96

Table V: Fire suppression tests with an air-flow rate of 1.0 kg/s and individual nozzles capped.

Pool	mass HFC-125 [kg]	injection rate [kg/s]	Nozzles	Suppression Time [s]
B1	3.2	0.83	2,3,4	1.3
B1	2.2	0.83	2,3,4	1.3
B1	3.2	0.74	1,3,4	1.5
B1	2.2	0.74	1,3,4	1.5
B2	3.2	0.83	2,3,4	none
B2	2.2	0.83	2,3,4	none
B2	3.2	0.74	1,3,4	4.6
B2	2.2	0.74	1,3,4	3.2
B3C3	3.2	0.83	2,3,4	1.6
B3C3	2.2	0.83	2,3,4	1.6
B3C3	3.2	0.74	1,3,4	none
B3C3	2.2	0.74	1,3,4	none
B5C5	3.2	0.74	1,3,4	2.4
B5C5	3.2	0.90	1,2,3	1.7

13.2 Results with individual nozzles capped: inhomogeneities

In previous sections, the capping of various nozzles was shown to result in suppressant inhomogeneities that left certain regions with little suppressant as indicated in Figs. 35, through 37. Of significant interest was the flow over pools B2 and B3 when nozzles 1 or 2 were capped as indicated in Fig. 40 and 41. To examine the effects of these inhomogeneities on the predicted suppression, a series of simulations were conducted where one nozzle was assumed to remain capped. For the majority of these simulations, the flow rate out of the other individual nozzles was maintained at the flow rate that corresponds to 1.07 kg/s if *all* the nozzles were opened. This results in a reduced flow rate for the sum of the three remaining nozzles relative to the sum of the four nozzles and an increased injection duration. This was done to facilitate the experimental validation process since the bottle pressure can presumably remain fixed with and without nozzles capped with the per nozzle flow rate primarily related to the bottle pressure driving the flow. Results of these tests are summarized in Table V.

For fires in pools B1 and B5C5, the removal of various nozzles is not found to alter the prediction of suppression. For pool B1 the removal of either nozzle 1 or 2 has little effect beyond delaying the suppression for a short time. This delay in suppression appears to correspond to the overall slower suppressant injection since longer suppression times correspond to slower injection.

For pool B5C5, the removal of nozzle 2 results in an increase in the suppression time because suppressant from nozzle 2 is entrained in the air inflow and carried back across the ribs surrounding the pool. Without nozzle 2, the suppression is delayed until suppressant from other nozzles works its way around the nacelle

to be entrained by the air inflow. The removal of nozzle 4, which is closest to pool B5C5 and injects suppressant around the aft section of the nacelle, has minimal effect on suppression of this pool since the mean flow along the nacelle bottom is aft-ward.

For pool B3C3, the removal of nozzle 1 has little effect other than to slightly delay the suppression. Removing nozzle 2, however, results in a failure to suppress fires in pool B3C3. As indicated in Fig. 41, the removal of nozzle 2 leaves a significant volume with little suppressant. This volume is the volume directly over the pool B3C3, and thus nozzle 2 is necessary to suppress fires in pool B3C3.

For pool B2, eliminating nozzle 1 leads to a predicted failure to suppress because the suppressant from nozzle 1 fills the forward nacelle and is entrained by the inlet air flow. In the absence of the high suppressant concentrations in the forward nacelle, the pool fire over B2 is predicted to be maintained upstream of the suppressant from nozzle 2 which passes over the downstream portion of that pool. Capping nozzle 2 is found to noticeably lengthen the suppression time because the suppressant from nozzle 2 creates strong flows in the vicinity of pool B2. Without the enhanced flow around pool B2 the entrainment of suppressant from the forward nacelle area is substantially slower.

14   Suppression of pool fires: pre-test predictions and test results

In the course of conducting the nacelle fire-suppression simulations and designing the tests, a number of factors were identified that led to a change in the test plan. The resulting test plan is described in this section along with the results of the pretest simulations and the actual tests. In general, the tests indicated that the pretest simulation results were largely correct.

This test series focused on extinguishing JP-8 pool fires contained by structural ribs and longerons along the lower nacelle surface. Prior to the testing, the bottom of the nacelle was lowered and the spaces between the ribs were sealed from their normal drain holes so that each could become a container for fuel. In the test series, three pools were used, beginning at the front of the nacelle and progressing in order to the middle of the nacelle. These pools are designated B1, B2 and B3C3. It was determined that pool B5C5 used in the simulations in the previous section would be too difficult to fill with fuel and ignite given its obstruction by the larger fourth and fifth structural ribs. In most of the tests, all three pools were ignited because this provided the strongest fire source; this was done largely to impose a sufficiently strong heat flux to the pools since the simulations described in the previous section indicated a sensitivity to heat losses. This sensitivity to heat losses is supported by observations of several tests conducted with a single pool. In several tests only the first or third pool was used in conjunction with a reduced number of agent-distribution nozzles in order to assess the spatial distribution of the agent in both the Vulcan model and the real nacelle. The fuel burning rate and the nacelle temperatures were observed to be substantially lower when a single pool was burned as predicted in the Vulcan pretest simulations and indicated in Fig. 43.

14.1 Key results from pretest predictions

Results from the pretest predictions described throughout this report and also the simplified analysis in Sec. 3 helped guide the design of the experimental test plan and test matrix. These results provide estimates of the overall concentration of suppressant in the nacelle, the duration of the transients as the concentrations rise and fall, and the uniformity of the suppressant distribution. To begin with, the simplified analysis of the relative masses of air and suppressant flowing into the nacelle can provide some guidance on the overall suppressant concentration and the transients. The suppressant mass-injection rate relative to the total inflow rate provides a characteristic mean steady-state mass fraction within the nacelle, $Y_{s,st}$ (Eq. 8). The injection must proceed for a long duration for the mean mass fraction to reach this characteristic steady-state value, but the mean mass fraction approaches this value in an exponential manner with an exponential time constant that is proportional to the total nacelle volume divided by the total volumetric influx. This time constant indicates the time scale for transients. In the tests conducted here, it was found that suppression is less sensitive to the total injected mass than it is to the rate of injection. This is a consequence of the short time scale for the transients (τ in Sec. 3), on the order of one to two seconds for the flows considered here, so that the characteristic steady-state mass fraction, $Y_{s,st}$, is approached.

The Vulcan predictions indicate, and the test results confirm, that the *overall* or *average* mass fraction of suppressant resulting in fire suppression is substantially greater than the cup burner value, which is $Y_{cb} = 0.28$ [9]. In general, the estimated average fraction required for suppression is on the order of 30% to 40% greater than the cup-burner value, according to the Vulcan simulations. A similar excess was required for the tests. The fact that a greater overall mass fraction is required indicates that inhomogeneities are significant. In other words, the suppressant mass fraction in certain regions of the flow is substantially less than the mean. Based on the combined test and simulation results, it is expected that the inhomogeneities in the suppressant mass fraction are on the order of 30-40%. Accounting for regions of high strain rate in the flow (near the air inlet) it is likely that the inhomogeneities are substantially larger. High rates of mixing present in the nacelle tend to reduce the mass fraction required to suppress the fire. It is found for HFC-125 that strained laminar flames are indicated to be suppressed at mass fractions as low as 0.16 [9]. This would correspond to $\tau_\eta = 0.2$ ms (Fig. 54), a typical value observed along the lower section of the nacelle in the simulations.

One of the primary objectives of the present study is to ascertain the predictive capabilities regarding the degree of inhomogeneity in the nacelle. To this end it is noted that predictions with the Vulcan models were very successful at reproducing extinction in a geometry where the suppressant was introduced in a uniform manner and the only mixing processes were related to a fire-stabilizing recirculation zone [13]. The present geometry is appreciably more complicated, and the leading challenge was expected to be the transport of the suppressant rather than the well-established suppression model itself. In order to evaluate the mixing

process for several scenarios, simulations and tests were conducted with different rates of injection and with different nozzle configurations. As an added variable, the air inflow rate was varied to simulate varying flight conditions. As indicated above, the ratio of the suppressant injection rate to the combined, total mass rates is indicative of the mean of the suppressant mass fractions in the nacelle.

14.2 Test plan

From the Vulcan simulations of various test conditions, it was predicted that the suppression would be more sensitive to the rate of injection of agent than the amount of suppressant, or equivalently the duration of injection. Further, suppression is indicated to be sensitive to the distribution of agent via the distribution of nozzles about the nacelle. With these results, a test plan was generated in the form of a rule-based sequence of tests. The test sequence is initiated with an approximation of the production suppression system, which is expected to result in successful suppression. From this point subsequent tests reduce the effectiveness of that system by either:

- reducing the suppressant injection rate by reducing the suppressant bottle pressure so that the sup-pressant?s mass fraction is likely to be reduced or

- removing a nozzle so that the distribution of suppressant is likely to be less uniform, or

- reducing the mass of suppressant injected for a given bottle pressure so that the fraction is reduced and held for a shorter duration.

Each of these paths was followed until at least one case was identified with a failure to suppress in the physical tests or until physical limitations on the test equipment were encountered. As indicated above, tests were run also for reduced air-flow rates. However, because of limitations on the rate of injection imposed by the HFC-125 vapor pressure, it was not possible to reach a condition where suppression failed at lower air flows. That is in agreement with predictions for lower air flows: the overall mass fraction of the agent for the physically attainable injection rates is always sufficiently high to extinguish the fires. Because the suppressant injection rate was identified throughout the pretest simulations as the most significant variable (among those that could physically be varied), for every other system variable tested, the suppressant in-jection rate was varied, attempting to reduce it until the suppression failed or until the minimum attainable injection rate had been tested.

For the tests in which a nozzle was removed (by capping the end), the sequence was repeated also by lowering the bottle pressure until suppression failed. The general sequence for changing the injection rate was to reduce the injection rate by 50% if the previous attempt succeeded and to increase the injection rate back to 75% of the original rate if the second attempt succeeded in suppressing the fire. The lowest injec-tion rate that is attainable is 50% of the nominal design injection rate, so this process results in bracketing

the suppression in proximity to 100%, 75%, and 50% of normal injection rates. The nominal pressures corresponding to these tests were 122, 275, and 515 psig (8.5, 19.0, and 35.5 bar) though these pressures vary somewhat with the mass of agent in the bottle. While these are relatively wide margins, the available resources did not allow for additional tests to narrow these bands. The tests actually conducted are summarized in Table VI. The tests in Table VI are labeled in the manner in which they were coded in executing the actual tests. The first digit, a number, is unique if one of the following is varied with respect to the baseline test configuration: the air flow rate is varied, a nozzle is capped, the suppressant mass is reduced. The second digit, a letter, varies in the sequence that a subset of tests were conducted. Typically the second digit varies according to the varying of the suppressant bottle pressure, and thereby the suppressant mass injection rate, although in some instances the number of pools burning or the mass of suppressant was varied within a subset of tests to address questions that arose during the test sequence. The final four digits, a day of the month in parenthesis, indicates the day of October, 2004, on which a test was conducted. A pair of tests, 1a and 1b were conducted in preparation during the prior week and duplicated on the week on which the remainder of the tests were conducted.

14.3 Summary of test results and corresponding pretest simulations

A total of twenty-five tests were conducted following the plan in Table VI to explore the edges of the suppression envelope for this ground test nacelle simulator. Two of these tests were conducted to determine whether or not individual pools (B1 and B3) could stabilize a fire. It was demonstrated that these pools could sustain a fire. This is in agreement with Vulcan simulations, although the Vulcan simulations indicated that the stability of fires in individual pools was sensitive to heat losses. Specifically, if the heat losses associated with conduction through the pool to the nacelle is 50% of the heat flux to the pool (essentially reducing the vaporization rate by 50%), then pools in sections B4 and B6 not employed in the present series of tests could fail to sustain themselves. Since it was not feasible to reach these locations to fill them with fuel and ignite them, this could not be confirmed. In the tests it was necessary to apply heat sources (heat lamps) to the nacelle under the pools to minimize heat losses just to get the fires stabilized under quiescent conditions, and this lends support to the Vulcan observations.

Of the remaining twenty-three tests, two tests were replications of the first two tests in order to gain confidence in the results; in each repeated test the results, in terms of whether suppression was successful or not, were identical. Because of the physical limitations, namely the vapor pressure of the HFC-125 and the inability to light or stabilize fires in certain pools, certain Vulcan simulations could not be reproduced. Consequently certain tests were run without pretest simulation results, but by using the arguments in Sec. 14.1 a similar range of parameter space was identified, and these results were in agreement with the Vulcan simulation trends. The results of the testing are described now for:

Table VI: Summary of tests conducted.

Test label	air inflow rate [lb/s]	pools	nozzles	supp. mass [lb]	bottle press. [psig]	targ supp rate [lb/s]
1a(21)	2	all	all	7	515	2.33
1a(25)	2	all	all	7	515	2.33
1b(21)	2	all	all	7	122	1.16
1b(26)	2	all	all	7	131	1.16
1d(25)	2	all	all	7	265	1.75
2a(27)	2	3	not 2	7	515	1.6
2b(27)	2	all	not 2	7	515	1.6
2c(27)	2	3	not 2	7	275	1.2
2d(27)	2	all	not 2	7	275	1.2
3b(27)	2	all	not 1	7	515	1.8
3d(27)	2	all	not 1	7	275	1.35
3e(28)	1.5	all	not 1	7	275	1.35
3f(28)	2	1	not 1	7	275	1.35
3g(28)	2	3	not 1	7	275	1.35
4a(28)	2	all	not 3	7	275	1.2
4b(28)	2	all	not 3	7	122	0.8
5b(25)	1	all	all	7	122	1.16
5d(25)	1	all	all	7	265	1.75
7a(26)	2	all	all	4.84	458	2.33
7d(26)	2	all	all	4.84	270	1.75
7e(28)	2	all	all	3	515	2.33
7f(28)	2	all	all	2.25	600	2.33
8a(26)	1.5	all	all	7	121	1.16

1. tests with all nozzles in which the ratio of the suppressant mass injection rate to the total mass injection rate was varied,

2. tests where the total mass of agent was reduced, and

3. tests where one of the nozzles was capped.

The results will be presented in terms of the target ratio of the suppressant mass injection rate to the total mass injection rate. Ideally, the pressure data indicated in Fig. 53 would be used to determine the actual suppressant discharge rate to a level of accuracy similar to the accuracy of the inlet flow meter. However, the unknowns associated with the phase transitions occurring both in the bottle and in the distribution piping prevent such a determination, as discussed in Sec. 10.5. Instead, the discharge rate is estimated. For this purpose, target discharge rates identical to those in the Vulcan simulations are employed. Specifically, with all nozzles discharging, the 3.2 kg of HFC-125 was presumed to discharge uniformly over 3, 4.5 and 6 s for bottle pressures of 515 (35.5 bar), 275 (19 bar), and 122 psig (8.5 bar). The discharge rate was presumed to be reduced in accordance with the reduction in the total nozzle area when nozzles were capped. Clearly, the assumption of constant discharge rates in the Vulcan model will be a source of test uncertainty, especially in light of the nonlinearity of the curves in Fig. 53. This uncertainty varies over the duration of the suppressant injection period, and the errors in the estimates provided here are likely to be greatest in the earliest (fraction of the first second) and latest periods of the injection. If the rate of suppressant injection is considered averaged over the significant couple of seconds, say the first 2-3 s of the injection process, then based on the results of our analysis, we estimate uncertainties on the order of 15%.

The results of the tests employing all nozzles are shown in Fig. 55. We first discuss the results of tests with labels starting in '1' '5' or '8' because they correspond to baseline cases using approximately seven pounds (3.2 kg) of suppressant at varying bottle pressures and air flows. This series can be viewed as varying the ratio of the suppressant mass injection rate to the total mass influx rate. Suppression is observed to fail when this ratio is below (approximately) 0.4 ($\pm$10% uncertainty in this value, but the total uncertainty is estimated at $\pm$19%). This corresponds to those cases where the air-flow rate is greatest (2 lb/sec, 0.9kg/s) and the bottle pressure is lowest (122 psig, 8.5 bar). For reduced air-flow rates (1.5 lb/sec, 0.68 kg/s) or increased bottle pressures (265 psig, 18.2 bar) suppression is successful. The Vulcan predictions are in agreement with the test results for all of these tests. The fact that the ratio of injection rate exceeds the cup burner mass fraction by a factor of 1.4 (0.4/0.28) is indicative of the degree of inhomogeneity in the system.

The results in Fig. 55 with labels starting '7' are those tests where the mass of suppressant was reduced from 7 lbs, to 4.84 lbs, 3 lbs and 2.2 lbs (from 3.2 kg to 2.2, 1.4 and 1 kg). All of these tests resulted in successful suppression of the fire. In all of these cases, the rate of injection was close to that for the designed conditions; in other words, the suppressant was injected just as fast, but for a shorter duration, in these tests.
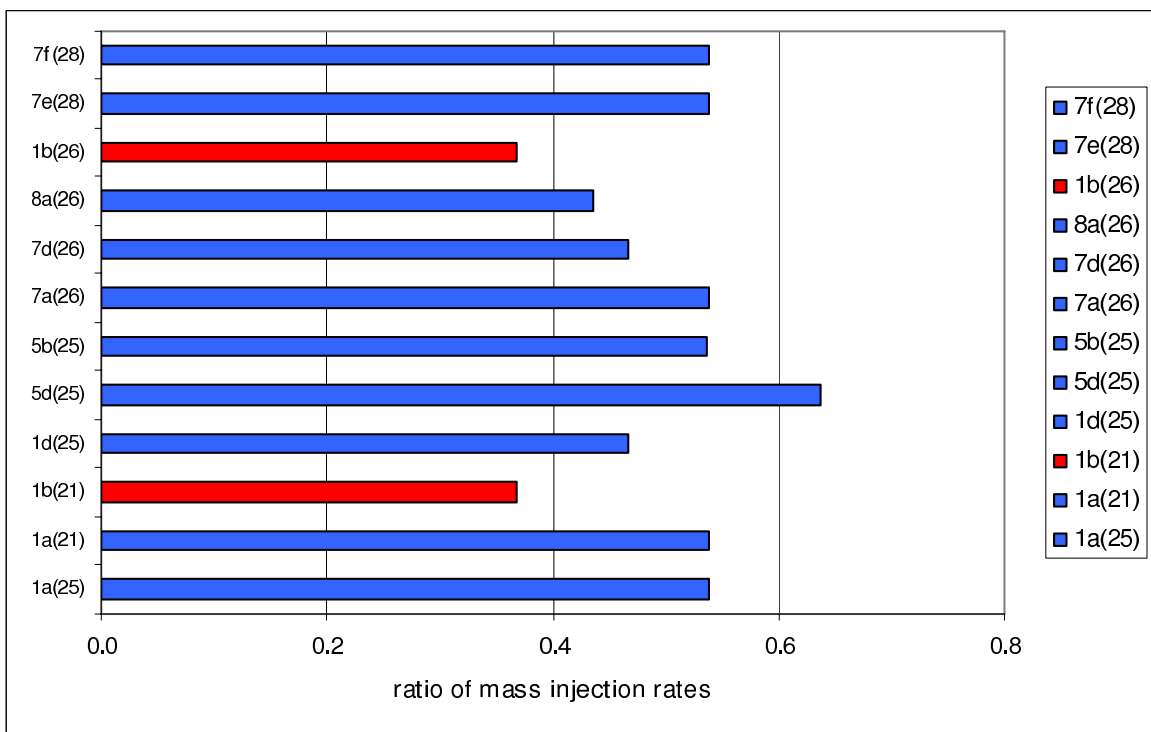
Figure 55: A summary of results for tests with all nozzles. Blue bars represent successful extinction, while red bars represent a failure to suppress the fire. In all of these cases, the Vulcan predictions were in agreement with the tests.
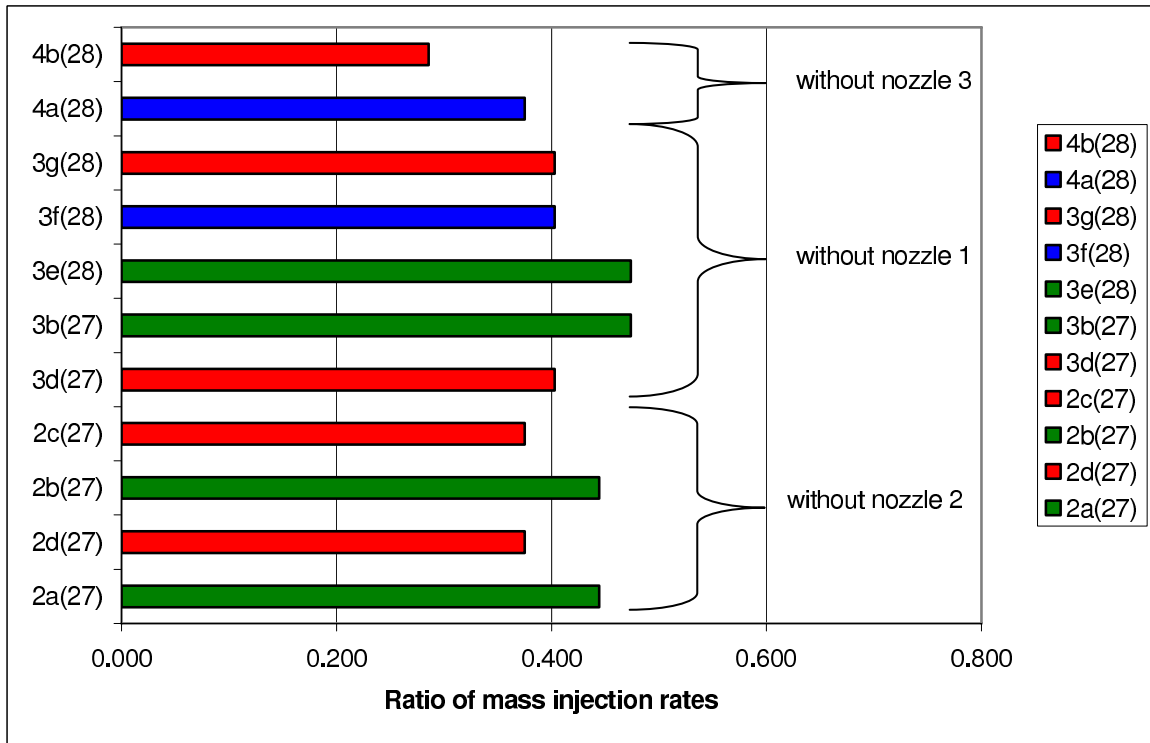
Figure 56: A summary of test results with specified nozzles capped. Those cases shown with the blue bars represent successful extinction, and those shown with red bars represent a failure to suppress the fire. In all of these cases, the Vulcan predictions were in agreement with the test results. Green bars indicate cases where suppression was successful in the tests, but Vulcan indicated failure to extinguish.

It is estimated that the bulk of the suppressant is injected in 3 s for 7 lbs, in 2 s for 4.84 lbs, and in 1 s for 2.2 to 3 lbs. These results reinforce the importance of the ratio of mass injection rates. The Vulcan simulations were conducted with 7 and 4.84 lbs (3.2 and 2.2 kg) of agent, and the results were in agreement with the tests. No Vulcan simulations were run for agent masses less than 4.84 lbs (2.2 kg).

Figure 56 summarizes results for those tests in which one of the four nozzles is capped. Capping a nozzle has two effects: First of all, the total nozzle area is reduced so that, for the same nominal bottle pressures employed, the suppressant injection rate is reduced. The reduction depends on each specific nozzle orifice diameter (Table I), but the reduction is on the order of 25%. This effect is captured by the indicated ratio of the mass injection rates. The second effect of capping a nozzle is the increased inhomogeneity inside the nacelle. More inhomogeneity would require a greater ratio of injection rates to define the boundary between successful and failed suppression. In the Vulcan simulations, it was predicted that higher inhomogeneity would be associated with capping either nozzles numbered 1 or 2 but not 3.

The results of tests when nozzle 3 is capped are indicated by the labels with the prefix '4' at the top

105

of Fig. 56. It is seen that the mass ratio where suppression fails is moving towards lower values than observed when all nozzles are employed. It is not certain whether or not the degree of inhomogeneity actually decreases and performance of the system improves by capping nozzle 3, and this conclusion should not be drawn based on the present results even though this is implied in the test results. Nozzle 3 injects suppressant into the upper nacelle, far from any of the pool fires considered here. For this reason, reduced suppressant in the upper nacelle may not impact suppressant levels in the lower nacelle where the fires are.

Tests where nozzle 1 is capped are indicated with the prefix '3' in Fig. 56. For these tests, it is necessary to refer to Table VI, because in some tests only specific pools were ignited to find the locations where fires failed to extinguish. The tests where all pools are ignited are discussed first (3b, 3d, 3e). In cases 3b and 3e the Vulcan simulations and the tests showed different outcomes; based on the results of this overall program, cases 3b and 3e are considered to be the same parameter space and 3e was run specifically to confirm the result of test 3b. Specifically, the Vulcan predictions indicated a failure to suppress the fire in test 3b (the Vulcan prediction for 3e was not actually run, but assumed to provide the same result as 3b) whereas the fire was extinguished in the tests. Reducing the injection rate so that the ratio of mass rates is 20% less leads to a successful prediction as in case 3d. This implies that Vulcan tends to predict failure to suppress before it actually occurs. This may be because the mixing rate within the Vulcan simulation errs on the low side, thereby tending to underestimate mixing in highly cluttered areas bounded by walls. This is thought to be the case because the clutter model, as implemented for the pretest simulations, did not account for enhanced mixing properly near the wall. Improvements to the clutter model may improve these predictive capabilities, but the fact that Vulcan predictions tend to be conservative, with a safety factor on the order of 20% as indicated here, is viewed as preferable and acceptable. In terms of the ratio of the mass injection rates, the tests indicate a critical value between 0.4 and 0.45, a statistically insignificant increase over the 0.4 ($\pm15\%$) estimated for tests employing all nozzles. The Vulcan predictions indicated that the critical ratio of mass injection rates was between 0.45 and 0.55. In tests 3f and 3g, only pools B1 and B3 were filled, respectively. This was done to ascertain the location of the inhomogeneity that led to failed suppression. Here it was found that low concentrations of agent occur in the vicinity of pool B1 and not pool B3. This agrees with the Vulcan simulations. We view the ability of Vulcan to identify the region where the fire could not be suppressed as favorable. Such information is particularly useful in designing tests where one might want to locate fires in particularly challenging-to-suppress areas.

The results of tests for which nozzle 2 is capped are indicated by the labels with the prefix '2' in Fig. 56. As with the previous examples, the Vulcan simulations indicated a failure to suppress at the higher injection rates for tests '2a' and '2b' due to increased inhomogeneities. The test results show that the failure to suppress occurs at the next step down in the injection rate (or the suppressant bottle pressure), the same as when nozzle 1 was capped. This again indicates a roughly 20% safety factor relative to the Vulcan simulations. It is noted that the failure to suppress when either nozzle is capped occurs at a ratio of injection

rates that is again spanning 0.4 which is the same value indicated in the tests employing all nozzles. This implies that the degree of inhomogeneity in the tests where nozzles were capped is not significantly greater than those where all nozzles were open; in the Vulcan simulations capping nozzle 2 did indicate greater inhomogeneities in the fire region. Test '2a' was a duplication of '2b' except for the fact that only the third set of pools (B3C3) is filled in test '2a.' Similarly, test '2c' is a duplicate of test '2d' except that only pool B3C3 was filled. These results show that extinction of pool B3C3 is difficult when nozzle 2 is capped. This is in agreement with the Vulcan predictions, except for the above mentioned 20% difference in the injection rate required in Vulcan.

15 Summary and Conclusions

In this report a detailed CFD analysis of fire suppression predictions within an aircraft engine nacelle is made using Vulcan. The geometry is that of a nacelle simulator used for ground-based fire tests. The distribution of the suppressant within the nacelle is described based on predictions and compared with available point-wise measurements. Simulations are conducted in which pool fires are ignited in the nacelle and then the ability of various suppressant discharges to suppress these fires is predicted. Following this series of simulations, tests were conducted in the simulator to evaluate the Vulcan predictions. In most of the cases considered the tests indicated agreement with the suppression predictions.

The Vulcan suppression model that makes these predictions possible is based on the concept of a critical Damköhler number for flame extinction. Such a model relates the available fluid time for heat release to the maximum chemical heat-release rates. This model captures the full range of dilution, cooling and chemical inhibition modes of extinction through a detailed chemical-kinetic model of the flame-extinction process.

A general understanding of the suppression-system effectiveness can be obtained by considering two factors: first, an overall average mass fraction of suppressant provided to the nacelle and, second, a level of inhomogeneity in the suppressant mass fraction throughout the nacelle. The first can be understood using zonal type models while the second can only be understood using a well-instrumented test fixture or a CFD approach like the present.

To leading order, the average mass fraction of the suppressant in the nozzle is determined by the ratio of the mass injection rate of the suppressant to the total mass injection rate (mostly suppressant plus air). In addition to the average mass fraction it is necessary to understand how uniformly the suppressant is distributed within the nacelle. Regions where the suppressant mass fraction is too low provide locations where a fire can be stabilized until the suppressant has been dissipated. The degree of inhomogeneity is determined by the location of the suppressant nozzles and the rate of turbulent mixing around these nozzles and throughout the nacelle. The cluttered nature of nacelles tends to lead to relatively rapid mixing, but the CFD results suggest, and the tests confirm, that the level of inhomogeneity is still high enough that 30-40%

excess average mass fraction is required to insure suppression throughout the nacelle.

Vulcan predictions and tests were conducted using a four nozzle system similar to that installed on a production aircraft. The predictions and test results indicate that this suppression system is also effective against pool fires as studied here. In order to cause a suppression failure, it was necessary to reduce the suppressant bottle pressure by roughly a factor of four so that the estimated suppressant discharge rate was half of the design discharge rate. In this case, both the predictions and test results indicate a failure to suppress.

In predictions, the mass of the suppressant injected was reduced by approximately 30%, and this was found to have no detrimental effect in the suppression. The test results confirmed this, and tests with as much as a 70% reduction in suppressant mass also resulted in suppression. (The potential for hot-surface relight may be sensitive to the suppressant mass and this was not tested here.)

To go beyond the installed suppression system design, certain nozzles were capped for certain tests. The pretest predictions indicated that capping the nozzles referred to as 1 or 2 (Table I) should leave regions where the suppressant was insufficient to suppress the fires. The test results indicate that for both of these cases, it was necessary to reduce the suppressant injection rate by 25% before this occurred. In other words, the Vulcan predictions indicated slightly more more inhomogeneities than the tests suggest when nozzles 1 or 2 are capped. This leads to slightly conservative results for the Vulcan predictions. When nozzle 3 is capped, the Vulcan results were in agreement with the test results.

Within the report, the CFD predictions are used to indicate the fraction of the volume over which the suppressant is predicted to be sufficient for suppression. These integral measures obtained using CFD provide information on the inhomogeneities that goes beyond information provided by zonal models.

The results also highlight the challenges of comparing measurements in complex environments with simulations. Challenges are reported in (1) the sensitivity of point-wise concentration measurements both to position uncertainties in complex geometries and to the details of the suppressant injection momentum, (2) the temporal response of thermocouples in dynamic fire environments, and (3) the relating bottle pressures to mass-discharge rates.

The simulation results also suggest several guidelines regarding the arrangement of the suppressant injection nozzles. Specifically, the predictions suggest that providing the suppressant into the vicinity of the primary air inlet is most effective in providing a uniform distribution. The test results suggest that this effect may be stronger in the simulations than in reality, but it is not possible to make the detailed assessment within the physical nacelle simulator.

References

[1] V. Babushok, T. Noto, D. R. F. Burgess, and A. Hamins W. Tsang. Influence of CF_3I, CF_3Br, and CF_3H on the high-temperature combustion. *Combust. Flame*, 107:351–367, 1996.

[2] A. R. Black, W. Gill, and J. Suo-Anttila. Numerical predictions and experimental results of a dry bay fire environment. Technical Report SAND2003-4112, Sandia National Laboratories, Albuquerque, NM, 2003.

[3] H. J. Curran, P. Gaffuri, W. J. Pitz, and C. K. Westbrook. A comprehensive modeling study of n-heptane oxidation. *Combust. Flame*, 114(1-2):149–177, 1998.

[4] P. E. DesJardin, J. M. Nelson, L. A. Gritzo, and T. A. Ghee. On the development of a subgrid scale clutter model, aiaa 2002-0984. In *40th AIAA Aerospace Sciences Meeting*, 2002.

[5] P. J. Disimile, J. R. Tucker, B. Croswell, and J. M. Davis. The transport of water sprays past generic clutter elements found within engine nacelles. *Fire Safety Journal*, 40(1):65–78, 2005.

[6] J. Dolinar, D. Hudgins, R. Myers, and D. Keyser. F-18 E/F nacelle simulator input/output boundary condition flows. Technical Report INS/F-18-1, INS, June 2002.

[7] M. S. Eldred, A. W. Giunta, B. G. Van Bloemen Waanders, S. F. Wojtkiewicz, W. E. Hart, and M. P. Alleva. DAKOTA, a multilevel parallel object-oriented framework for design optimization, parameter estimation, uncertainty quantification, and sensitivity analysis : version 3.0 users manual. Technical Report SAND2001-3796, Sandia National Laboratories, 2002.

[8] R. G. Gann. FY2003 annual report next generation fire suppression technology program (NGP). Technical Report NIST TN 1457, PP-1059, NIST, 2004.

[9] A. Hamins, T. G. Cleary, P. Borthwick, N. N. Gorchkov, K. B. McGrattan, G. P. Forney, W. L. Grosshandler, C. Presser, and L. Melton. Suppression of engine nacelle fires. In R. G. Gann, editor, *Fire Suppression System Performance of Alternative Agents in Aircraft Engine and Dry Bay Laboratory Simulations*, volume 2, pages 1–199. NIST, 1995.

[10] A. Hamins, G. W. Gmurczyk, W. L. Grosshandler, R. G. Rehwoldt, I. Vasquez, T. G. Cleary, C. Presser, and K. Seshadri. Fire suppression effectiveness. In R. G. Gann, editor, *Evaluation of Alternative In-Flight Fire Suppressants for Full-Scale Testing in Simulated Aircraft Engine Nacelles and Dry Bays, NIST SP 861*, volume 4, pages 345–465. NIST, 1994.

[11] A. Hamins, C. Presser, and L. Melton. Suppression of a baffle-stabilized spray flame by halogenated agents. In *Proc. Combust. Instit.*, volume 26, pages 1413–1420. The Combustion Institute, Pittsburgh, 1996.

[12] J. C. Hewson and A. R. Kerstein. Local extinction and reignition in nonpremixed turbulent $CO/H_2/N_2$ jet flames. *Combust. Sci. Tech.*, 174(5-6):35–66, 2002.

[13] J. C. Hewson, S. R. Tieszen, W. D. Sundberg, and P. E. Desjardin. CFD optimization of fire suppression and its role in optimizing suppressant distribution. In *Proceedings of the Halon Options Technical Working Conference*, Albuquerque, NM, 2003.

[14] R. Hirst, P. J. Farenden, and R. F. Simmons. The extinction of fires in aircraft jet engines–Part I, small-scale simulation of fires. *Fire Technol.*, 12:266, 1976.

[15] R. Hirst, P. J. Farenden, and R. F. Simmons. The extinction of fires in aircraft jet engines–Part II, full-scale tests. *Fire Technol.*, 13:59, 1977.

[16] R. Hirst and D. Sutton. Effect of reduced pressure and airflow on liquid surface diffusion flames. *Combust. Flame*, 5:319, 1961.

[17] J. M. Holen, M. Brostrom, and B. F. Magnussen. Finite difference calculation of pool fires. *Proc. Combust. Inst.*, 23:1677–1683, 1990.

[18] W. P. Jones and B. E. Launder. Prediction of laminarization with a 2-equation model of turbulence. *Int. J. Heat Mass Transfer*, 15:301, 1972.

[19] D. Keyser. Personal Communication, 2003.

[20] D. R. Keyser and J. C. Hewson. Fire suppressant distribution in an engine nacelle. In *Proceedings of the Halon Options Technical Working Conference*, Albuquerque, NM, 2004.

[21] G. T. Linteris, D. R. Burgess, V. Babushok, M Zachariah, W. Tsang, and P. Westmoreland. Inhibition of premixed methane-air flames by fluoroethanes and fluoropropanes. *Combust. Flame*, 113:164–180, 1998.

[22] F. C. Lockwood and N. G. Shah. A new radiation solution method for incorporating general combustion prediction procedures. *Proc. Combust. Inst.*, 18:1405–1414, 1980.

[23] A. Luketa-Hanlin. Personal communication. 2005.

[24] B. F. Magnussen. The eddy dissipation concept. In *Proceedings of the Eleventh Task Leaders Meeting*, Lund, Sweden, 1989. IEA Working Group on Conservation in Combustion.

[25] Northrop Grumman Test Work Description LNV12.01-013. F/A-18 E/F HFC-125 fire protection system qualification test report. Technical report, Northrop Grumman, El Segundo, California, Feb. 29 2000.

[26] E. Meeks, H. K. Moffat, J. F. Grcar, and R. J. Kee. Aurora: A fortran program for modeling well stirred plasma and thermal reactors with gas and surface reactions. Technical Report SAND96-8218, Sandia National Laboratories, 1996.

[27] S. V. Patankar. *Numerical Heat Transfer and Fluid Flow*. Taylor & Francis, 1980.

[28] F Takahashi, W. J. Schmoll, E. A. Strader, and V. M. Belovich. Suppression behavior or obstruction stabilized pool flames. *Combust. Sci. Tech.*, 163:107–130, 2001.

[29] F. Takahashi, W. J. Schmoll, E. A. Strader, and V. M. Belovich. Suppression of a nonpremixed flame stabilized by a backward-facing step. *Combust. Flame*, 122:105–116, 2001.

[30] S. R. Tieszen, D. W. Stamps, and T. J. O'Hern. A heuristic model of turbulent mixing applied to blowout of turbulent jet diffusion flames. *Combust. Flame*, 106:442–446, 1996.

[31] J. C. Yang, S. L. Manzello, M. R. Nyden, and M. D. Connaghan. Discharge of CF_3I in a cold simulated aircraft engine nacelle. In *Proceedings of the 2002 Halon Options Technical Working Conference*, Albuquerque, NM, 2002.

[32] S. S. Yoon, J. C. Hewson, P. E. DesJardin, D. J. Glaze, A. R. Black, and R. R. Skaggs. Numerical modeling and experimental measurements of a high speed solid-cone water spray for use in fire suppression applications. *Int. J. Multiphase Flow*, 30(11):1369–1388, 2004.

DISTRIBUTION:

3   Building and Fire Research Laboratory
National Institute of Standards and Technology
Attn: R. G. Gann
Building 224, Room A-261
100 Bureau Drive, Stop 8664
Gaithersburg, MD 20899-8664

2   Survivability Technology Branch
46th Aerospace Survivability and Safety Flight
Attn: Martin L. Lentz
46 OG/OGM/OL-AC
2700 D Street, Bldg. 1661
Wright-Patterson AFB, OH 45433-7605

1   Aircraft, UAVs and Support Systems
Attn: Juan A. Vitali, Division Chief
ATEC/AEC/AVED
4501 Ford Avenue, Suite 640
Alexandria, VA 22302

1   FM Global Research
Attn. L. Gritzo
1151 Boston-Providence Turnpike
Norwood, MA 02062

1   Naval Research Labortory
Attn: R. Sheinson
Code 6185
4555 Overlook Ave. SW
Washington, DC 20375-5342

1   Naval Air Systems Command
Systems Safety
Attn: D. Bein
NAWC Code 4.1.10.1, B562, Hwy 547
Lakehurst, NJ 08733-5049

1   Naval Air Systems Command
Air-4351
Attn: M. Tedeschi
Bldg. 562-3562, Hwy 547
Lakehurst, NJ 08733-5049

1   USAF 46 TW
Survivability and Safety Flight
Attn. P. Disimile
2700 D Street, Bldg. 22B
Wright-Patterson Air Force Base, OH 45433-7605

1   Air Combat Systems
Northrop Grumman Corporation
Attn. Greg Roberts
One Hornet Way M/S 8f60/W5
El Segundo, CA 90245-2804

1   Lockheed Martin Aeronautics Co.
Attn: Mark Stewart
Mail Zone 1705
P. O. Box 748
Fort Worth, TX 76101

1   Bennettech
Attn. J. M. Bennet
1020 Kellyn Lane
Hendersonville, TN 37075

1   Hughes Associates, Inc.
Attn: J. E. Floyd
3610 Commerce Dr., Suite 817
Baltimore, MD 21227

1   The Boeing Company
Attn: Jaesoo Lee
P. O. Box 3707 MC 67-ML
Seattle, WA 98124-2207

1	MS 0828	Amalia R. Black, 1544
1	MS 1135	Thomas K. Blanchat, 1532
1	MS 1135	Alex L. Brown, 1532
1	MS 1135	Victor G. Figueroa, 1532
5	MS 1135	John C. Hewson, 1532
1	MS 1135	Anay Luketa-Hanlin, 1532
1	MS 1135	Vern F. Nicolette, 1532
1	MS 1135	Jill Suo-Anttila, 1532
1	MS 821	Anothony L. Thornton, 1530
1	MS 1135	Sheldon. R. Tieszen, 1532
2	MS 9018	Central Technical Files, 8944
2	MS 0899	Technical Library, 4536